Ph. D. Thesis

INSTITUTE OF PHYSICAL CHEMISTRY

Polish Academy of Sciences

Dmytro Lisovytskiy

M.Sc., Met.Eng.

PHASE TRANSITIONS IN NANOCRYSTALLINE Li-Mn-O SYSTEMS – APPLICATION OF RIETVELD METHOD

Ph. D. Thesis

Supervisor: Professor **Jerzy Pielaszek**

Warsaw 2005

Dmytro Lisovytskiy, MS. Met. Eng.

PHASE TRANSITIONS IN NANOCRYSTALLINE Li-Mn-O SYSTEMS – APPLICATION OF RIETVELD METHOD

Abstract

Lithium Manganese spinel oxides are one of the most promising materials for producing of the electrodes for modern Li-ion rechargeable batteries because of their low cost and low toxicity in comparison with actually used compounds. Considering the wide interest in nanocrystalline systems which in many instances exhibit unusual properties as compared to the bulk materials it is generally anticipated that batteries constructed on the base of nanocrystalline spinel electrodes will have much better properties and will supply electrical energy not only for portable electronic application but also for electric vehicles. It is difficult to fabricate Li-Mn spinel electrode material with exact predetermined composition. Hence, there is the necessity of carrying out phase analysis of the synthesized spinel compounds. Another difficulty in application is that Li-Mn spinel at lowered temperature undergoes structural phase transition. This could affect the performance of the battery.

In the present work, systematic X-Ray diffraction (XRD) (including Rietveld) analysis and impedance spectroscopy studies of laboratory synthesized by sol-gel method and commercial Li-Mn spinel nanooxides have been undertaken in order to determine structural and electrical parameters and to estimate changes in phase composition caused by course of temperature phase transition and to study phenomena which accompany this phase transformation.

Special emphasis was put on the possibility, feasibility and usefulness of the use of Rietveld method for this particular case of nanomaterials.

As a special interest in materials studies are simultaneous measurements of different parameters, for the main group of samples which undergo the phase transition, in addition to standard XRD in Bragg-Brentano geometry measurements, simultaneous measurements of impedance spectra in the frequency range from 1 MHz to 0.1 Hz and X-ray pattern in non focusing geometry were performed, in the temperature range from -25^0C to $+100^0$C. For this purpose dedicated equipment was constructed and used. This way a correlation between the XRD profile parameters and conductivity calculated from impedance spectra was evidenced. $LiMn_2O_4$ and $Li_{1.005}Mn_{1.995}O_4$ samples obtained by high temperature sol gel method (800°C) exhibited phase transition from cubic to orthorhombic structure upon cooling below room temperature. Structural transition was clearly visible in the X-ray pattern as splitting of structure-sensitive reflections, e.g. 400, of cubic structure, and was accompanied by a decrease of conductivity by a factor of about 10 in the case of samples prepared from powders obtained by sol-gel method or supplied by Alfa Aesar Co. and heat treated up to 800°C. The phase transition was not complete even at –25°C in the samples prepared from powder supplied by Sigma-Aldrich Co. and heat treated also up to 800°C and no stepwise change of conductivity was observed for this sample. Additional phases, Mn_3O_4 or Li_2MnO_3, were found in commercial samples, while the spinels prepared by high temperature sol-gel method were single phase. It was evidenced that the appropriate application of the Rietveld method allowed not only precise phase identification but also quantitative analysis of the phase composition.

ACKNOWLEDGMENTS

This work was completed under the supervision of

Professor JERZY PIELASZEK

The author is deeply grateful to him for introduction
into the new and very interesting scientific field,
constant inspiration and engagement discussions,
care and parent attitude.
Without his continued encouragement and kind assistance
this thesis would not have been possible.

The Author would also like to sincere thanks

to ***Professor J. Molenda***
for kindly supplied samples

to ***Dr. J.R .Dygas*** and to ***Dr. Z. Kaszkur***
for their assistance in experimental work

to ***Professor Z. Karpiński***
and to ***all Colleagues*** from
the Department of Catalysis on Metals
of the Institute of Physical Chemistry, PAN
for their support and friendly attitude.

1. LITERATURE REVIEW

1.1. Lithium ion secondary battery

A battery is a device that converts chemical energy into electrical energy by means of an electrochemical reduction-oxidation (redox) reaction.

There are two types of batteries: primary and secondary. In primary batteries the electrode reactions are not reversible and the cells are therefore not rechargeable. In secondary batteries, the electrode reactions are reversible and the cells are rechargeable.

A battery comprises three main components: cathode, electrolyte and anode. The cathode is characterized as the electrode where a reduction-reaction occurs (i.e. electrons are accepted from an outer circuit), while an oxidation-reaction occurs at the anode (i.e. electrons are donated to an outer circuit). The electrolyte is an electronic insulator, but a good ionic conductor; its main function is to provide a transport-medium for ions to travel from one electrode to the other. It must also prevent short-circuiting by acting as a physical barrier between the electrodes, either alone in the case of a polymer or in the matrix it impregnates (the separator), if a liquid. The voltage and capacity of a cell are functions of the electrode materials used.

Among the most advanced batteries today are the Lithium-Ion batteries. This is a type of battery composed of Lithium, the lightest metal and the metal that has the highest electrochemical potential. Lithium, however, is an unstable metal, so Li-ion batteries are made from Lithium ions from chemicals. Because of its lightness and high energy density, Lithium-Ion batteries are ideal for portable devices, such as notebook computers. In addition, Lithium-Ion batteries have no memory effect and do not use poisonous metals, such as lead, mercury or cadmium. In new types of batteries, different Li-Mn-O spinel compounds could be used as a cthode material. In older type of Li-ion batteries materials were used containing Ni and Co ($LiNiO_2$ and $LiCoO_2$) with higher toxicity. The only two disadvantages the Lithium-ion batteries currently have is that they are quite expensive and are aging relatively quickly. Stability of lithium-ion is an issue that is often ignored. Lithium-based batteries have a lifetime of 2-3 years and the clock starts ticking as soon as the battery comes off the manufacturing line. The capacity loss manifests itself in increased internal resistance caused by oxidation. [2]

Battery research is focusing heavily on lithium chemistries, so much so that one could presume that all portable devices will be powered with lithium-ion batteries in the future.

CONTENTS

Mgr inż. Dmytro Lisovytskiy

PRZEMIANY FAZOWE W NANOKRYSTALICZNYCH UKŁADACH Li-Mn-O -ZASTOSOWANIE METODY RIETVELDA

Streszczenie

Tlenki litowo-manganowe są jednymi z najbardziej obiecujących materiałów do zastosowań w wytwarzaniu elektrod nowoczesnych litowych ogniw wielokrotnego ładowania. Wynika to z ich niskiego kosztu i niskiej toksyczności w porównaniu z dotychczas stosowanymi materiałami. Biorąc pod uwagę szerokie zainteresowanie układami nanokrystalicznymi, które w wielu przypadkach wykazują niezwykłe właściwości w porównaniu z materiałami litymi, uważa się powszechnie, iż ogniwa wytworzone na bazie nanokrystalicznych elektrod spinelowych będą miały lepsze właściwości i będą mogły zasilać nie tylko przenośne urządzenia elektroniczne, ale również pojazdy elektryczne. Jest bardzo trudno wytworzyć litowo-manganowe spinele o ściśle zaplanowanym składzie. Stąd konieczność przeprowadzenia dokładnej analizy fazowej w zsyntezowanych spinelach. Inną trudnością w zastosowaniach jest to, iż w niższych temperaturach w spinelach litowo-manganowych zachodzi przejście fazowe. A to może w sposób istotny wpływać na funkcjonowanie ogniwa.

W prezentowanej pracy badane były nanokrystaliczne spinele litowo-manganowe otrzymane metodą sol-żel w warunkach laboratoryjnych jak też i spinele handlowe. Aby określić parametry strukturalne i elektryczne oraz zmiany składu fazowego wywołane zmianą temperatury w trakcie przejścia fazowego a także zjawiska towarzyszące temu przejściu stosowana była rentgenowska analiza dyfrakcyjna (łącznie z analizą metodą Rietvelda) oraz spektroskopia impedancyjna.

Szczególna uwaga zwrócona była na możliwość, wiarygodność i użyteczność zastosowania metody Rietvelda dla tej klasy nanomateriałów.

W badaniach materiałów szczególnie istotnym jest możliwość jednoczesnego pomiaru różnych parametrów. W przedstawianej pracy reprezentatywna grupa preparatów, które wykazywały przejście fazowe była, oprócz standardowych pomiarów dyfrakcyjnych w geometrii Bragg-Brentano, poddana jednoczesnym pomiarom impedancyjnym w zakresie 1 MHz do 0.1 Hz i dyfrakcyjnym w geometrii nieogniskującej. W tym celu opracowany został i skonstruowany specjalny układ pomiarowy. Pozwoliło to na bezpośrednie otrzymanie zależności pomiędzy parametrami profilu dyfrakcyjnego i przewodnictwa elektrycznego, obliczonego z widm impedancyjnych. Preparaty $LiMn_2O_4$ i $Li_{1.005}Mn_{1.995}O_4$ otrzymane wysokotemperaturową (800^0C) metodą sol-żel wykazywały przy schładzaniu poniżej temperatury pokojowej przejście fazowe od struktury regularnej do rombowej. Przejście to było widoczne jako rozszczepienie czułych strukturalnie refleksów struktury regularnej (np. 400), któremu w przypadku preparatów otrzymanych metodą sol-żel i preparatów handlowych firmy Alfa Cesar Co. wygrzewanych w 800^0C towarzyszył około 10-krotny spadek wartości przewodnictwa. W przypadku preparatów otrzymanych z materiału wyprodukowanego przez Sigma-Aldrich Co. i tak samo wygrzewanych w 800^0C przejście fazowe nie było zupełne nawet w -25^0C. Dla tych preparatów nie obserwowano również skokowej zmiany przewodnictwa w trakcie przejścia fazowego. W preparatach komercyjnych stwierdzono dodatkowe fazy: Mn_3O_4 lub Li_2MnO_3, niestwierdzalne w preparatach otrzymanych metodą sol-żel, które były jednofazowe. Wykazano, iż odpowiednie zastosowanie metody Rietvelda pozwoliło nie tylko na dokładną identyfikację fazową, ale również na ilościowe określenie składu fazowego.

INTRODUCTION

One of the most important challenges for scientists in XXI century is finding solutions for more effective global environmental protection and finding more and safer sources of electrical energy for exponentially growing needs of the modern society. For these aims new energy transfer and new energy storage technologies such as battery energy storage must be developed. Not only for portable electronic applications but also for modern, emission free electric vehicles.

Among the various types of rechargeable batteries which are being developed, the Li-ion battery is one of the best-suitable candidates because of its non toxicity, high cyclability, low cost, high voltage, slim geometry and global availability of lithium.

Lithium is the lightest of all metals, has the greatest electrochemical potential. Therefore, Li-ions are optimal charge carrier for battery systems.

It is well known that lithium could be intercalated/deintercalated reversibly in several compounds, which makes it possible for use as the cathode in rechargeable lithium batteries.

Manganese oxides are the most promising compounds for the innovative Li-ion rechargeable battery cathodes because of their non toxicity, low price and availability.

Pioneering work on the lithium battery began by G. N. Lewis in 1912, but it was interrupted until the early 1970's when the first nonrechargeable lithium batteries became commercially available. Attempts to develop rechargeable lithium batteries were continued in the 1980s, but failed due to the safety problems [1].

After much research on rechargeable lithium batteries during the 1980s, in 1991, Sony commercialized the first lithium-ion battery. Other manufacturers followed suite. Today the lithium-ion is the fastest growing battery chemistry in the world. But despite the impressive growth in sales of batteries worldwide, the science underlying battery technology is often criticized for its slow advancement.

Li-ion batteries are used where high-energy density and light weight is of prime importance. This is another reason why the Lithium ion battery is considered to be the fastest growing battery system. Good working properties can be realized in attractive group of newest batteries, with a lithium transition metal oxide as cathode, for example spinel type Li-Mn oxides.

The present investigations form a part of the worldwide research aimed at finding novel mobile and rechargeable sources of electrical energy for cellular telephones, computers

(lap-tops) and many other useful portable devices. This research focuses on materials for the development of rocking-chair battery technology, which can contribute to an electrical energy based society. It is believed that new materials and technologies can solve global human problems closely interrelated, in the so-called trilemma problem: increase in energy production, economic growth, and global environmental protection.

1. LITERATURE REVIEW

1.1. Lithium ion secondary battery

A battery is a device that converts chemical energy into electrical energy by means of an electrochemical reduction-oxidation (redox) reaction.

There are two types of batteries: primary and secondary. In primary batteries the electrode reactions are not reversible and the cells are therefore not rechargeable. In secondary batteries, the electrode reactions are reversible and the cells are rechargeable.

A battery comprises three main components: cathode, electrolyte and anode. The cathode is characterized as the electrode where a reduction-reaction occurs (i.e. electrons are accepted from an outer circuit), while an oxidation-reaction occurs at the anode (i.e. electrons are donated to an outer circuit). The electrolyte is an electronic insulator, but a good ionic conductor; its main function is to provide a transport-medium for ions to travel from one electrode to the other. It must also prevent short-circuiting by acting as a physical barrier between the electrodes, either alone in the case of a polymer or in the matrix it impregnates (the separator), if a liquid. The voltage and capacity of a cell are functions of the electrode materials used.

Among the most advanced batteries today are the Lithium-Ion batteries. This is a type of battery composed of Lithium, the lightest metal and the metal that has the highest electrochemical potential. Lithium, however, is an unstable metal, so Li-ion batteries are made from Lithium ions from chemicals. Because of its lightness and high energy density, Lithium-Ion batteries are ideal for portable devices, such as notebook computers. In addition, Lithium-Ion batteries have no memory effect and do not use poisonous metals, such as lead, mercury or cadmium. In new types of batteries, different Li-Mn-O spinel compounds could be used as a cthode material. In older type of Li-ion batteries materials were used containing Ni and Co ($LiNiO_2$ and $LiCoO_2$) with higher toxicity. The only two disadvantages the Lithium-ion batteries currently have is that they are quite expensive and are aging relatively quickly. Stability of lithium-ion is an issue that is often ignored. Lithium-based batteries have a lifetime of 2-3 years and the clock starts ticking as soon as the battery comes off the manufacturing line. The capacity loss manifests itself in increased internal resistance caused by oxidation. [2]

Battery research is focusing heavily on lithium chemistries, so much so that one could presume that all portable devices will be powered with lithium-ion batteries in the future.

In many ways, lithium-ion is superior to nickel and lead-based chemistries and the applications for lithium-ion batteries are growing as a result.

Lithium-ion has not yet fully matured and is being improved continuously. It is estimated that new metal and chemical combinations are being tried every six months to increase stability and prolong service life. The improvements in longevity after each change will not be known for a few years [1].

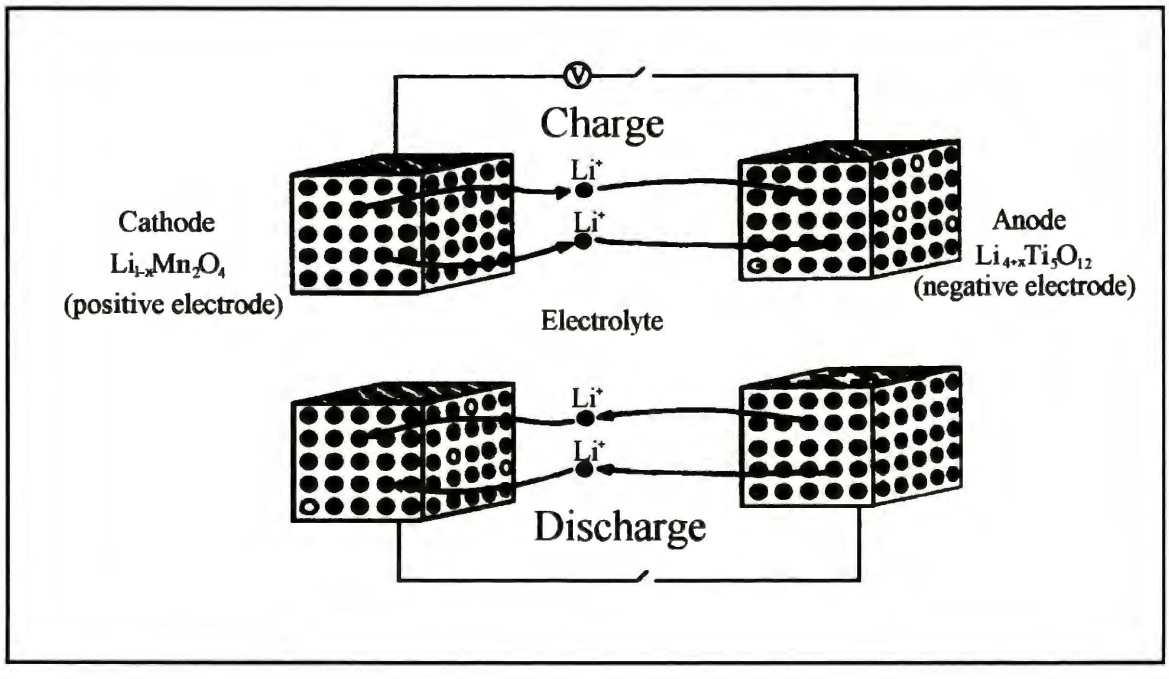

Fig. 1.1. Schematic illustration of a spinel anode/spinel cathode lithium-ion cell [3].

1.2. Li-Mn-O spinel electrodes

The early interest in spinel electrodes for Lithium battery applications was started by the discovery that the [B2]X4 framework of many stable $A[B_2]X_4$ spinels, such as $LiMn_2O_4$ (and other) provided a stable host structure for the electrochemical insertion and extraction of lithium. Schematic illustration of a spinel anode/spinel cathode lithium-ion cell presented on Fig.1.1. During discharge of a Lithium/spinel cell, the insertion reaction is accompanied by a simultaneous reduction of the A and/or B cations of the host. In general, spinel electrodes can be lithiated to the rock salt stoichiometry ($LiA[B_2]X_4$) before the $[B_2]X_4$ framework is destroyed. The lithium spinels $Li[B_{2-x}Li_x]O_4$ (B= Mn, Ti, Co, V; $0 \leq x \leq 0.33$), are of particular interest because the $[B_{2-x}Li_x]O_4$ spinel framework provides an uninterrupted and energetically accessible three-dimensional interstitial space

of face-sharing tetrahedra and octahedra for Li+-ion diffusion through the structure. Moreover, it is possible to extract lithium from $Li[B_{2-x}Li_x]O4$ structures with a concomitant oxidation of the B cations, thereby increasing the operating capacity of the spinel electrode over a wider compositional range [4].

The ideal properties for insertion electrodes in a Li-ion cell are:

-Minimal change in the host network to ensure good reversibility.

-Light host structure that is able to accommodate a significant amount of Li to provide a high capacity.

-Good electronic and ionic conductivity to provide high rate capability

-Chemically and structurally stable over the whole voltage range and insoluble in the electrolyte.

-Inexpensive and non-toxic.

1.3. Spinel structure

Spinels have the formula AB_2O_4, where A can be a Group IIA (2) metal or transition metal in the +2 oxidation state, and B is a Group IIIA (3) metal or transition metal in the +3 oxidation state. Spinels belong to cubic crystal system, of space group number 227, full Hermann-Mauguin symbol $F4_1/d-32/m$, short symbol Fd-3m, point group (crystal class) is m-3m, Patterson symmetry is Fm-3m, Pearson symbol cF56, Shoenflies symbol O^7_h.[5]

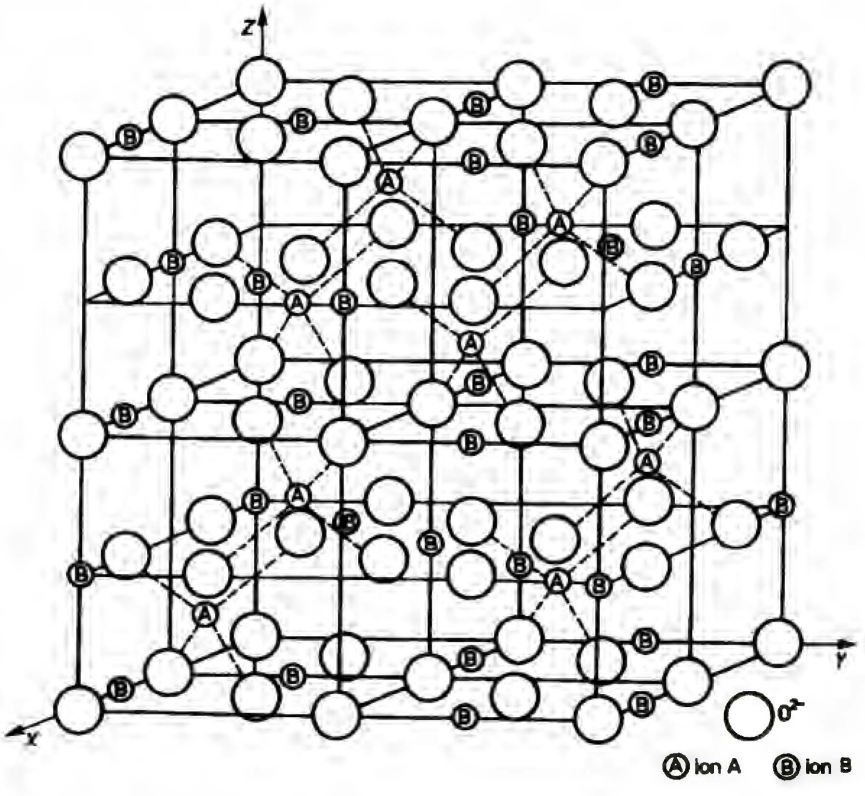

Fig. 1.2.Unit cell of the spinel [6].

The oxygen ions form a close-packed cubic lattice, which can be regarded as consisting of eight octants. All these octants are simple FCC unit cell, with eight tetrahedral holes and four octahedral holes. Part of these holes is occupied by ions A and B in a definite way.

The crystallographic unit cell of the spinel structure $A_8B_{16}O_{32}$ or $(AB_2O_4)_8$ (Fig.1.2.) contains approximately thirty two cubic close packed O atoms. For every thirty two close packed O atoms, there are thirty two octahedral and sixty four tetrahedral holes, but in the space group of spinel there are equivalent positions for eight atoms in tetrahedral and sixteen in octahedral coordination. Coordinates of atoms are listed below:

1. thirty two O-atoms

0,0,0; 1/2, 1/2, 1/2; 1/4, 1/4, 1/2↻; 3/4,3/4,0↻; 3/4,3/4,1/2↻; 3/4,0,1/4↻; 0,0,1/2↻; 1/4,1/4,0↻; 1/2,1/2,0↻; 3/4,1/4,1/2↻.

2. sixteen atoms type B

1/4,1/4,1/4; 3/4,3/4,1/4↻; 0,0,1/4↻; 1/4,1/2,1/2↻; 3/4,0,1/2↻.

3. eight atoms type A

5/8,5/8,5/8; 1/8,1/8,5/8↻; 7/8,7/8,7/8; 7/8,3/8,3/8↻.

In a regular spinel, the ions of the Group IIA (2) metal or transition metal in the +2 oxidation state occupy one-eighth of the tetrahedral holes and the ions of the Group IIIA

(3) metal or transition metal in the +3 oxidation state occupy one-half of the available octahedral holes.

Spinels also exist in inverse structures $B(AB)O_4$, in which the A ions and one half the B ions exchange places. Therefore, the A ions occupy octahedral holes along with one half of the B ions while the other one-half of the B ions are in tetrahedral holes.

Some spinels exist in an intermediate structure between normal and inverse. For this reason, it is convenient to describe the structure of spinels by the parameter Δ, which is defined as the fraction of B ions in tetrahedral holes .The values of Δ range from zero for regular spinels to 0.50 for inverse spinels. Intermediate values (such as 1/3) are found in a random spinel.

In some publications we can find mentioning about so called delta-spinels; their formula is $A_{1+\delta}B_{2-\delta}O_4$. In another way it can be represented as $\{A\}_{8a}[B_{2-\delta}A_{\delta}]16_dO_4$, where 8a and 16d refer to the tetrahedral A sites and octahedral B sites of the prototypic spinel space group Fd-3m. For example, in the case of fully delithiated lithium manganese spinel so called λ–MnO_2 ($Li_0Mn_2O_4$), the formula in spinel notation will be following: $\{\square_{1.0}\}8a[Mn_2]16dO_4$ and for lithium manganese delta-spinel with δ=0.005 the notation is $\{Li_{1.0}\}8a[Mn_{2-0.005}Li_{0.005}]16dO_4$.

1.4. Li-Mn-O system compounds

1.4.1. The Li-Mn-O phase diagram

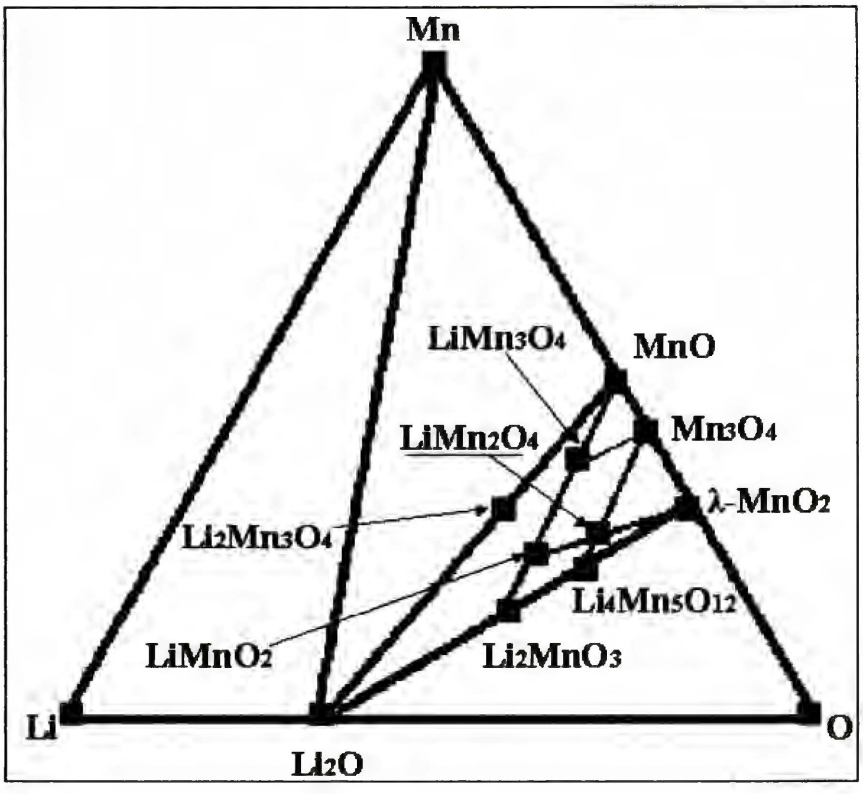

a)

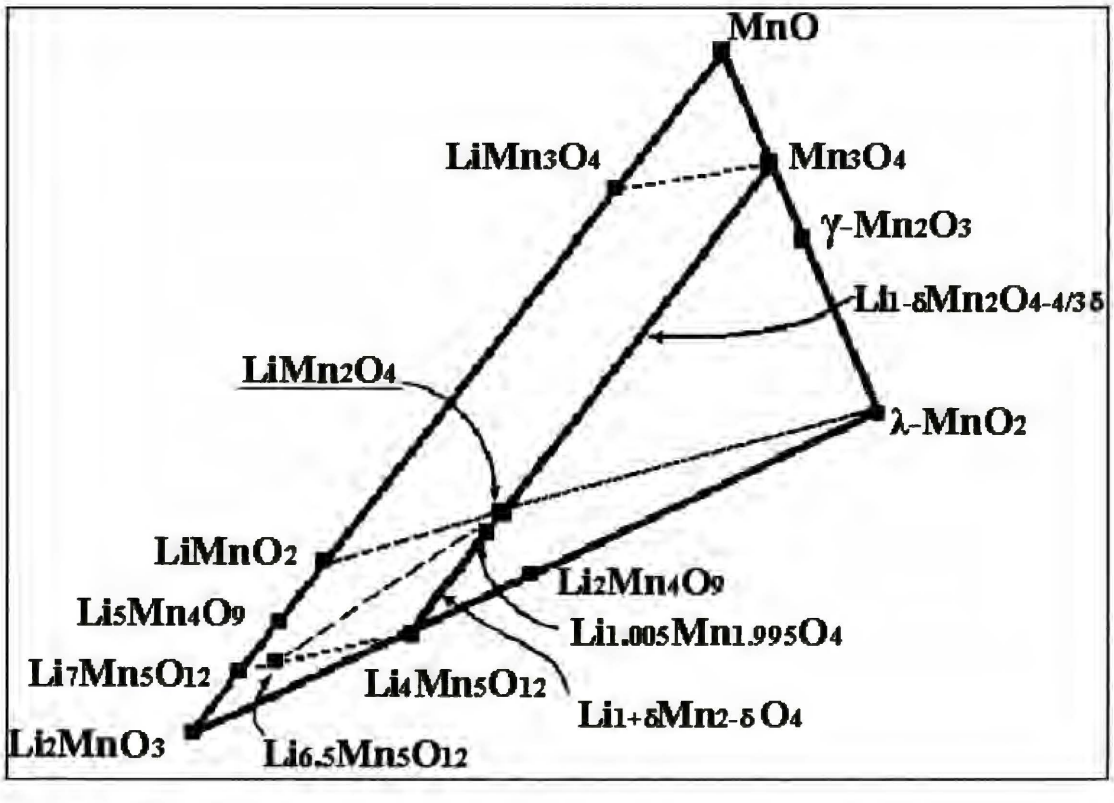

b)

Fig. 1.3. a) The Li-Mn-O phase diagram. b) Enlargement Li_2MnO_3- MnO- λ-MnO_2 region; modified and redrawn from [7].

A representation of the Li-Mn-O phase diagram highlighting the positions of spinel compositions within the λ-MnO_2, MnO and Li_2MnO_3 tie-triangle is shown in Fig. 1.3.a; an expanded view of this tie-triangle is shown in Fig. 1.3.b [7]. It shows the location of known structures and emphasizes the wide range of spinel compositions that exist in the lithium-manganese-oxygen system. Stoichiometric spinels fall on the tie line between Mn_3O_4 and $Li_4Mn_5O_{12}$ (Fig. 1.3.b). Lithium insertion/extraction reactions into/from the spinel phases are represented by λ-MnO_2 – $LiMnO_2$ lines. The stoichiometric spinels of importance for lithium battery applications form a solid solution between $LiMn_2O_4$ and $Li_4Mn_5O_{12}$; they can be represented by the general formula $Li_{1+\delta}Mn_{2-\delta}O_4$ for $0 \leq \delta \leq 0.33$. These spinels can be lithiated to their rock salt compositions which fall on the tie-line between $LiMnO_2$ and $Li_7Mn_5O_{12}$. Because lithium insertion into $Li_{1+\delta}Mn_{2-\delta}O_4$ spinels is accompanied by the immediate displacement of tetrahedrally-coordinated lithium ions into octahedral sites, the area that falls within the $LiMn_2O4$ - $Li_4Mn_5O_{12}$ - $Li_7Mn_5O_{12}$ - $LiMnO_2$ quadrilateral represents a region of defect rock salt compositions. Extraction of lithium from the tetrahedral sites of $Li_{1+\delta}Mn_{2-\delta}O_4$ electrodes drives the composition of these spinels toward the MnO_2 - $Li_4Mn_5O_{12}$ tie line in the phase diagram; the area that falls within the MnO_2 - $LiMn_2O_4$ - $Li_4Mn_5O_{12}$ tie triangle, therefore, constitutes a region of defect spinel compositions. The various spinel structures that are of interest in the Li-Mn-O system can be defined by the three tie-lines of the MnO_2 - $LiMn_2O_4$ - $Li_4Mn_5O_{12}$ triangle. They represent the following systems: (i) $Li_x[Mn_2]O_4$ ($0 \leq x \leq 1$), (ii) $Li_{1+\delta}Mn_{2-\delta}O_4$ ($0 \leq \delta \leq 0.33$), and (iii) $Li_2O \cdot yMnO_2$ ($y \geq 2.5$).

1.4.2. The $LiMn_2O_4$ spinel system

The regular lithium manganese spinel formula is $LiMn_2O_4$, more precisely $Li^{+1}Mn^{+3}Mn^{+4}O_4^{-2}$, because the average Mn valence state is +3.5, i.e. there are equal numbers of Mn^{3+} and Mn^{4+} ions. The Li-ions occupy the 8a tetrahedral sites (one eighth of the all tetrahedral sites), both type of Mn-ions occupy the 16d octahedral sites (one half of the all octahedral sites) in a cubic close-packed (ccp) lattice of O-ions (32e sites). There are three vacant sites: the 8b tetrahedral sites, the 16c octahedral sites, and 48f tetrahedral sites. The structure of $LiMn_2O_4$, showing the relative positions of atoms is illustrated in Fig. 1.4.

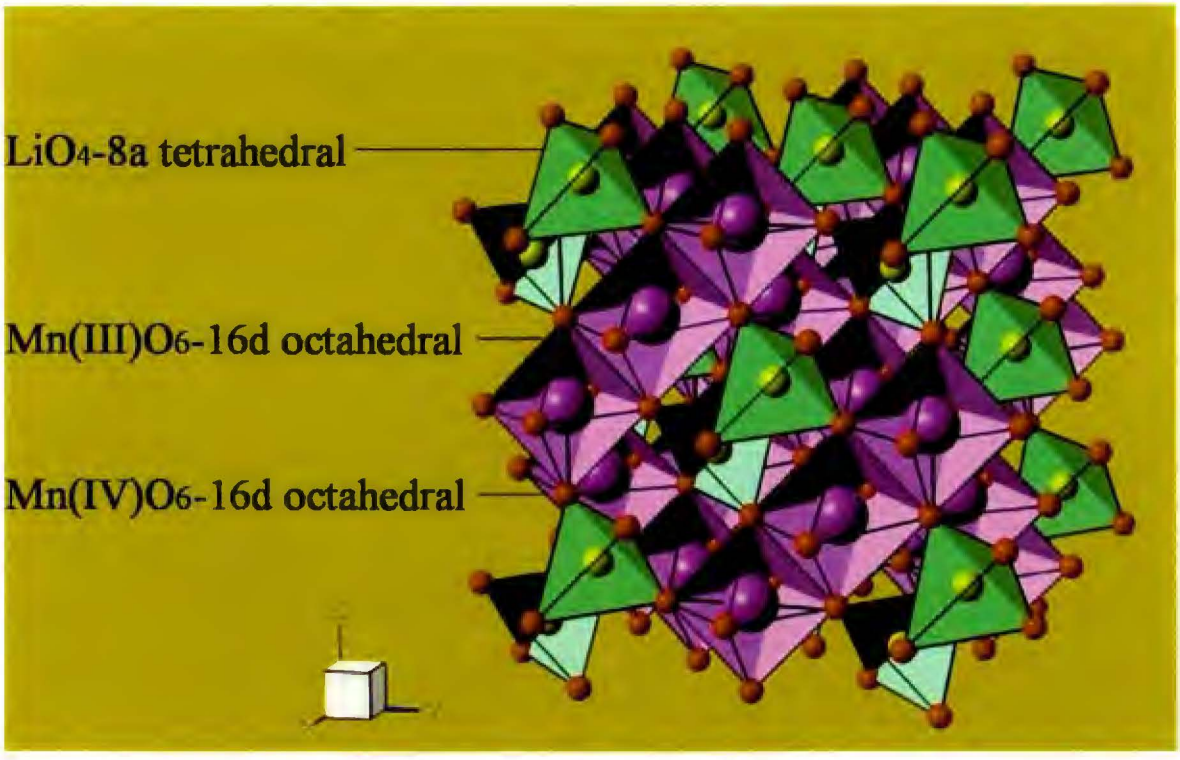

Fig. 1.4. Spinel structure of $LiMn_2O_4$.

The interstitial space in the Mn_2O_4 framework represents diamond-type network of tetrahedral 8a and surrounding octahedral 16c sites. These empty tetrahedra and octahedra are interconnected with one another by common faces and edges to form three-dimensional (3D) host for Li^+ ions. The schematic representation of Mn_2O_4 framework is shown on Figure 1.5.

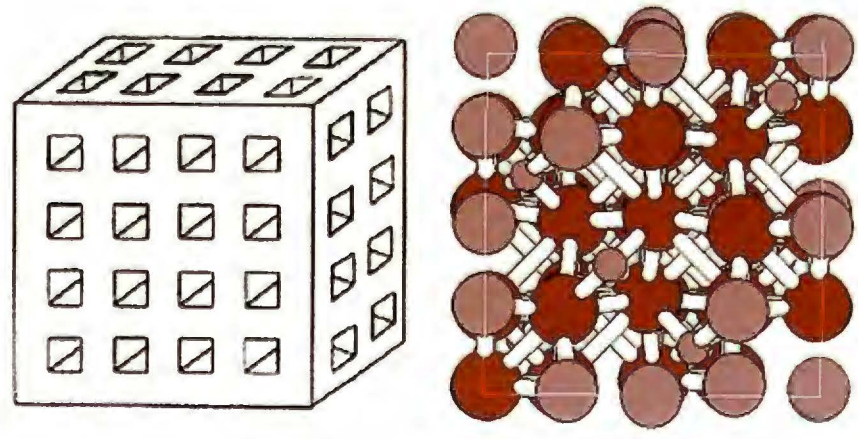

a) b)

Fig. 1.5. a) Schematic representation of void spaces in 3D host $\{\square_{1.0}\}$ $[Mn_2]$ O_4;
b) Structure of $Li_{0.03}$ Mn_2 O_4 spinel (ICSD #40484) created using Balls & Sticks program.

The structure of the $[Mn_2]O_4$ spinel framework shows the octahedral coordination of the manganese ions and the three-dimensional interstitial pathways for lithium-ion diffusion during working of cathode of battery. As mentioned above, in the spinel structure the MnO_6 octahedra are edge-shared and form a continuous three-dimensional cubic array (the manganese ions being distributed between alternate oxygen layers of the cubic close packed (ccp) array in a 3:1 ratio), thereby imparting a robustness and stability to the $[Mn_2]O_4$ spinel framework. Furthermore, of all the interstitial tetrahedra (8a. 8b and 48f) and octahedra (16c), the 8a tetrahedra are situated farthest from the 16d octahedral occupied by manganese; they share each of their four faces with adjacent, vacant 16c octahedra.

These structural features account for the unique stability of stoichiometric spinel compounds, many of which are found in nature, as exemplified by the stability of the prototype mineral, spinel, $MgAl_2O_4$.

1.5. Phase transitions

Phase transition is the transformation of a thermodynamic system from one phase to another. The distinguishing characteristic of a phase transition is an abrupt change in one or more physical properties, in particular the heat capacity, with a small change in thermodynamic variables such as e.g. the temperature.

The cause of phase transitions is a change of stability of phases caused by external factors. A phase which is stable at one set of values of temperature and pressure may change to a different phase when either one or both of these variables change. Many elements and compounds change type of crystal structure under appropriate changes of temperature and/or pressure, these changes, too, being phase changes. Phase transitions often (but not always) take place between phases with different symmetry. Generally, we may speak of one phase in a phase transition as being more symmetrical than the other. The transition from the more symmetrical phase to the less symmetrical one is a symmetry-breaking process. In the fluid-solid transition, for example, we say that continuous translation symmetry is broken. Generally, the more symmetrical phase is on the high-temperature side of a phase transition, and the less symmetrical phase on the low-temperature side.

The first attempt of classifying phase transitions was the Ehrenfest (classical) classification scheme [8], which grouped phase transitions based on the degree of non-analyticity involved. Under this scheme, phase transitions were labeled by the lowest derivative of the free energy that is discontinuous at the transition. First-order phase transitions exhibit a discontinuity in the first derivative of the free energy with a thermodynamic variable. The various solid/liquid/gas transitions are classified as first-order transitions because they involve a discontinuous change in density (which is the first derivative of the free energy with respect to pressure.) Second-order phase transitions have a discontinuity in a second derivative of the free energy. These include the ferromagnetic phase transition in materials such as iron, where the magnetization, which is the first derivative of the free energy with the applied magnetic field strength, increases continuously from zero as the temperature is lowered below the Curie temperature. The magnetic susceptibility, the second derivative of the free energy with the field, changes discontinuously. Under the Ehrenfest classification scheme, there could be, in principle third, fourth, and higher-order phase transitions. In Figure 1.6. are shown the changes in thermodynamic properties accompanying first and second-order transitions. Though useful,

Ehrenfest's classification is a simplified approach. The Ehrenfest scheme is an inaccurate method of classifying phase transitions, for it is based on the mean field theory of phases.

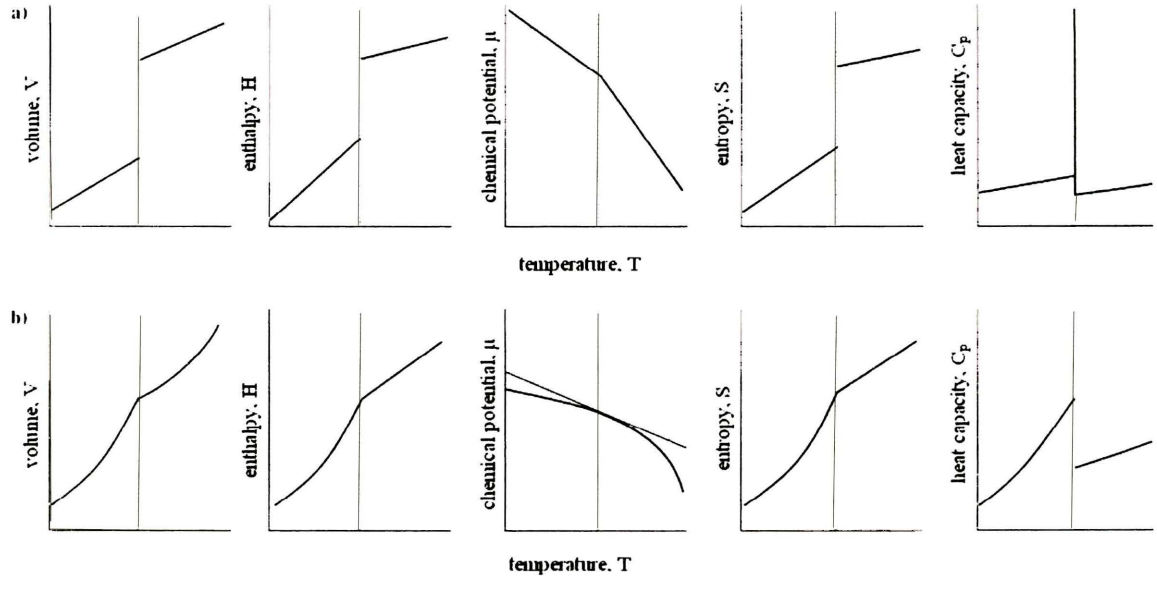

Fig.1.6. The changes in thermodynamic properties accompanying (a) first order and (b) second-order transitions, dotted lines show the temperature of phase transition. [8]

Mean field theory is inaccurate in the vicinity of phase transitions, as it neglects the role of thermodynamic fluctuations. In the modern (non classical) classification scheme [9], phase transitions are divided into two broad categories, named similarly to the Ehrenfest classes.

The first-order phase transitions are those that involve a latent heat. During such a transition a system either absorbs or releases a fixed (and typically large) amount of energy. Because energy cannot be instantaneously transferred between the system and its environment, first-order transitions are associated with "mixed-phase regimes" in which some parts of the system have completed the transition and others have not. Mixed-phase systems are difficult to study, because their dynamics are violent and hard to control. However, many important phase transitions fall in this category, including the solid/liquid/gas transitions.

The second class of phase transitions are the continuous phase transitions, also called second-order phase transitions. These have no associated latent heat. Examples of second-order phase transitions are the ferromagnetic transition, the superfluid transition, and Bose-Einstein condensation.

Several transitions are known as the infinite-order phase transitions. They are continuous but break no symmetries.

Despite numerous publications [10,11,12,13], works for complex classification of phase transitions are continued. In Fig.1.7. presented is one of the classification scheme on a three dimensional plot.

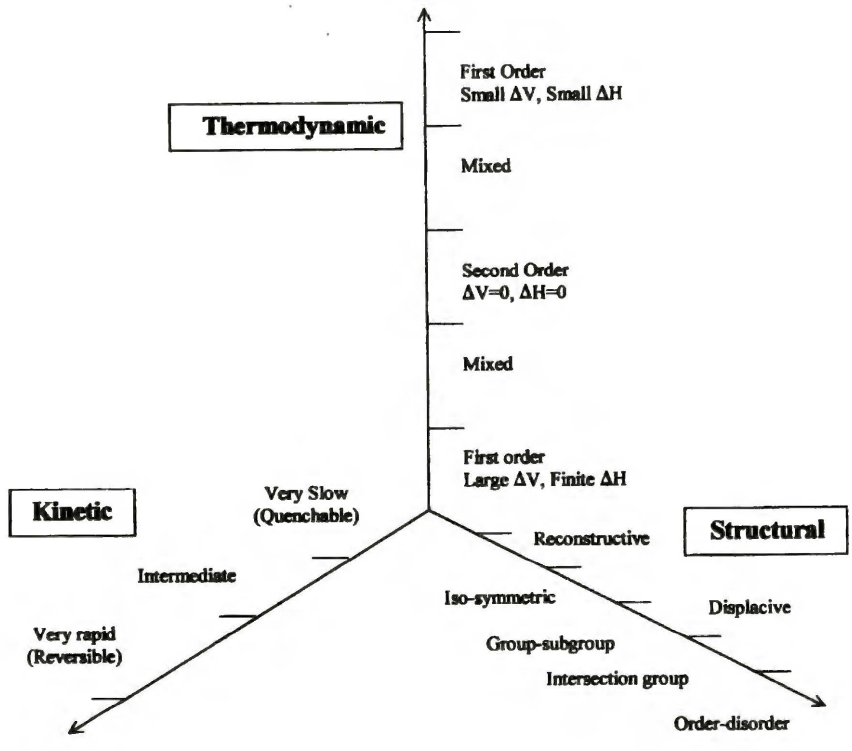

Fig. 1.7. Classification scheme on a three-dimensional plot [14].

The kinetic classification simply divides transitions into two main groups: rapid, or non-quenchable, and sluggish. However, no real classification scheme can be based on this parameter since it does not treat any basic property of either of the two phases.

The thermodynamic classification leads to a very satisfactory conceptual scheme, dividing all phase transitions according to their 'order'(discussed above).

Thermochemical classification proposes to classify all transitions by the magnitudes of ΔH (change in enthalpy) and ΔS (change in entropy). It was hoped that if a matrix of these two elements is constructed, transitions could be pigeonholed in it. The difficulty arises because of the unavailability/unreliability of the data on ΔH and ΔV (change in volume).
While the thermodynamic treatment of phase transitions is fundamental and useful, it does not provide a geometrical picture of the microscopic changes accompanying a transition. A classification into four categories was proposed [15]: iso-symmetric, group–subgroup,

intersection group and order–disorder transitions. In fact, the major strides made in the understanding of the crystal chemistry [16,17] in terms of atomic arrangements and bonding can be advantageously applied to the study of phase transitions in solids. For example, the new phase obtained after a transition may be related to the parent phase. The transition may have been accompanied by a change in the primary coordination or secondary coordination either being brought out by a reconstructive or displacive mechanism.

1.5.1. Structural considerations of phase transitions in solids

In conditions of full thermodynamic balance in a system, which practically is never realized in real conditions of experiment (at infinitely slow change of temperature), phase transition would take place at temperature T_0, corresponding to condition of equality of specific thermodynamic potentials. Structural phase transitions of such a type are *first order phase transitions*. We shall consider further basically phase transitions in the crystals, connected with rather small distortions of a crystal lattice leading nevertheless to change of symmetry of a crystal. In case when these distortions are continuous the *second order phase transitions* take place; it is essential, that in this case the state of a crystal changes continuously, smoothly. In the point of the first order phase transition position of atoms change abruptly. Close to the point of the second order phase transition, distortion of structure and each elementary cell can be very small. Second order phase transition have no temperature hysteresis, are not accompanied by abrupt change of volume and entropy, and groups of symmetry of phases possess "continuity": with reverse of the temperature distortion of crystal structure at a point of phase transition leads to losing some of elements of symmetry of more ordered (usually, high-temperature) phases.

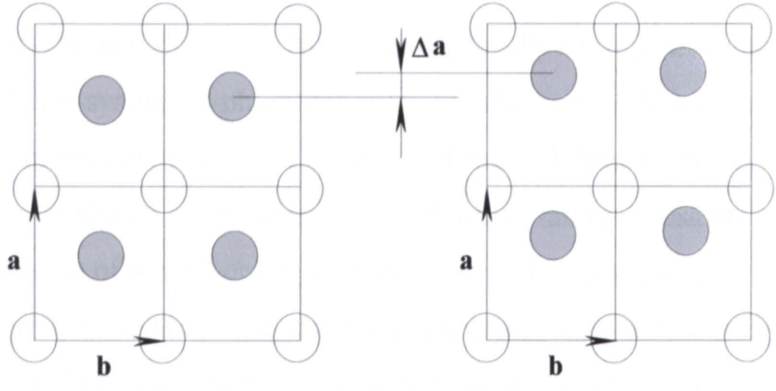

Fig. 1.8. The centered rectangular two dimensional lattice [18].

We shall discuss basic features of structural phase transitions on an example of the face centered rectangular two dimensional lattice (Fig. 1.8.). Let's assume, that at some temperature one sublattice is displaced in a particular direction with respect to the other one. We shall name the initial phase symmetrical, and the new, distorted phase - asymmetrical. For quantitative description of that kind of transformation of a crystal, the parameter η - a fraction of translation, on which atoms of sublattice are displaced is introduced:

$$\eta = \frac{\Delta a}{a} \tag{1.1}$$

value $\eta=0$ corresponds to a symmetrical, and $\eta\neq0$ - to an asymmetrical phase. We shall note, that this parameter is not a unique one and generally it is defined by specificity of the system and nature of the phase transformations. In Fig. 1.9 various variants of temperature dependence of η are shown:

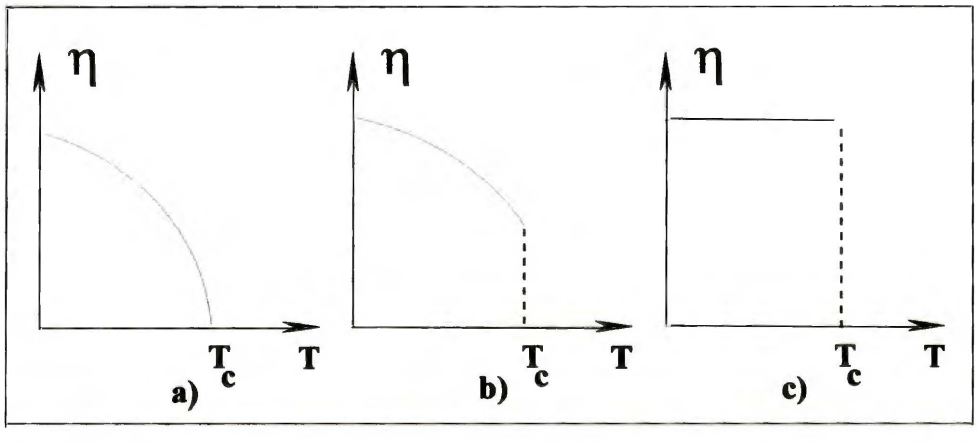

Fig. 1.9. The temperature dependence of the order parameter η in a field of different types of structural phase transitions. a) Second order phase transition; b) First order phase transition, close to second order phase transition; c) First order phase transition. [18]

Phase transitions and structure changes are generally closely associated. The higher temperature, higher symmetry phase generally transforms to a lower temperature phase with loss of symmetry elements. The change in Bravais lattice symmetry at a first order transition often produces small changes in absolute lattice constants and in atomic positions. In the case of second order phase transitions, the point group of lower symmetry must be a subgroup of the higher symmetry point group, with consequently small atomic displacements. [19,20]. A test on the utility of any classification is to see whether it enables us to understand a transition being studied.

1.6. Nanomaterials - tendency in developing and characterization

The rational design of properties of a material has begun to focus on its composition at the nanometer scale. To the engineer, chemist, and material scientist, the challenges of controlling morphology at these dimensions are compounded by their intermediate scale, where neither molecular nor bulk models are satisfactory. With domain sizes generally ranging from 1 to 100 nm, an appreciable portion of a nanophase material is subjected to forces related to grain boundaries and interfaces. As the domain size increases, these forces become negligible and the characteristic properties associated with a macroscopic sample gradually appear. During this evolution a number of physical and electron constants for a material are, in fact, variable. As the ability to alter the behavior of a material through changes in dimensions is harnessed, new avenues are expected to open in material design.

In the last decade, materials science has witnessed substantial progress in the synthesis, characterization, and understanding of materials with atomic dimensions. Using a variety of techniques such as ball milling, sputtering, sol gel formation, it is possible to generate materials with dimensions and sizes ranging from a few angstroms to several nanometers. The electronic, magnetic, optical, and chemical properties of these materials have been found to be very different from those of the bulk form and to depend sensitively on size, shape, and composition.

For receiving samples with nanometric size grains, described in the present work the sol-gel technology was used. Considered as one of the most promising method for obtaining oxides of nanometric size it is described in preparation section and in literature [21,22,23]. The sol gel process refers broadly to room temperature solution routes for preparing oxide materials. In most cases, the process involves the hydrolysis and polymerization of metal alkoxide precursors of silica, alumina, titania, and manganese as well as other oxides. The solutions of precursors are reacted to form irreversible gels that dry and shrink to rigid oxide forms.

In the 1980s when the sol gel process enjoyed resurgence in interest, the emphasis was on the duplication of conventionally prepared ceramics and glasses. Trying the sol gel process was motivated by claims of the purity of the starting materials and the generally lower temperatures required for processing.

In today's terminology, sol gel processing is a form of nanostructure processing. Not only does the sol gel process begin with a nanometer-sized unit, a molecule, it also undergoes reactions on the nanometer scale resulting in a material with nanometer features.

The scale of this sol gel process requires probing by different scattering techniques (for example x-ray diffraction studies).

The concept behind the sol gel process is that a combination of chemical reactions turns a homogeneous solution of reactants into an infinite molecular weight oxide polymer. This polymer is a three dimensional skeleton surrounding interconnected pores. Ideally the polymer is isotropic, homogeneous, and uniform in nanostructure, and it replicates its mold exactly and miniaturizes all features without distortion. The nanostructure of gels is, in fact, of interest, from both scientific and technology points of view.

The proper characterization of nanodimensional materials is a connecting bridge between the material synthesis and processing, and the understanding of the unusual properties that result from spatial confinement. X-ray diffraction is a standard structural characterization technique for bulk materials that can be proposed for successful application to study nanostructures [24]. There are however some distinctive aspects of diffraction from nanoparticles which should be taken to account.

Nanocrystalline materials exhibit an atomic structure which differs from that of the two known solid states: the crystalline (long-range order) and amorphous (short-range order). They are polycrystals; the crystallite size of which is a few nanometers (1-100nm). The very small grain size of clusters in nanophase materials gives their diffraction pattern the appearance of an amorphous material. The problem is in accuracy of describing nanoparticle structure. Decreasing of size of crystalline structural domains affects the shape of the X-ray diffraction lines, which no longer consist of narrow, symmetrical, delta-function like peaks, such as the diffraction lines given by an ideal powder diffraction pattern. That leads to difficulties in detecting and determining structure of nanomaterials by X-ray diffraction, especially during graphical analysis of diffraction pattern.

Size-dependent and structure-specific features in diffraction patterns can be quite striking in nanometer sized particles. Small particles have fairly distinct diffraction patterns, both as a function of size and as a function of structure type. In general, regardless of the structure, there is a steady evolution in the aspect of diffraction profiles: as particles become larger, abrupt changes do not occur, features grow continuously from the diffraction profile and more details are resolved. These observations form the basis for a direct technique of diffraction pattern analysis that can be used to obtain structural information from experimental diffraction data [25].

The properties of nanocrystals and nanocrystalline materials are determined by their microstructure, i.e., crystallite size and shape, microstrains and defects, and grain and

nterphase boundaries. One of the most frequent applications of XRD analysis in polycrystalline materials phase determination is crystallite size calculation. This is also the case in the present work and the method used is described later.

X-ray diffractometry is a relatively simple technique that provides structural information statistically averaged over an extended spatial region. When combined with other techniques it constitutes a powerful tool for characterization of the microstructure. A straightforward application of the XRD technique is the determination of the crystalline structure of a material. This can be done by comparing the diffraction spectrum peak positions and intensities with those in the reference literature, e.g., the ICSD (Inorganic Crystal Structure Database) or JCPDS (Joint Committee on Powder Diffraction Standards) databases. This is especially true for nanocrystalline materials that may contain several crystallographic phases, including highly disordered or amorphous phases, and for nanocrystals whose crystal structure may be different from that of the corresponding bulk form [24]. Though such approach is very useful, there are nevertheless some difficulties. For example, identifying and properly ascribing additional lines originating on diffraction pattern from impurity phases (when quantity of minor phases is less than 5 percent). Quite often the peaks are overlapped, for example, when in a sample coexist few phases. Particular cases are $LiMn_2O_4$ and $Li_4Mn_5O_{12}$ phases, of interest in this work; when all the peaks are largely overlapped, because these compounds have the same Fd-3m space group and differ only slightly in lattice parameters. The Rietveld method is probably the only one that can be useful for separating so closely related phases in compounds.

Despite some complication, nano approach is especially advantageous in the case of materials for manufacturing of new types of batteries with high exploitation parameters such as high energy density. Today manufacturers produce polycrystalline electrode materials with particle size about 10-30 μm. In common opinion this is insufficient for designing todays battery systems. More and more publications are devoted to describing modern methods and technologies for synthesizing materials with particle size lower than 100 nm for following (e.g. electrodes) application in new renewable energy sources.

AIM OF THE WORK

Lithium Manganese oxides were widely studied over last years as alternative candidates to replace more expensive and toxic $LiCoO_2$ and $LiNiO_2$ for cathodes in the commercial lithium-ion batteries. Despite growing interest in Li-Mn spinel type oxides there are still not enough structural data on these spinels, including the course of the phase transition. It should be also noted that the main crystallographic data bases practically do not contain any information about phases appearing in Li-Mn spinels after phase transition around 280K.

Apparently, the existence of phase transition in lithium manganese spinels near room temperature, i.e. close to the working temperature of the battery, may cause changes in its important operational parameters. In the literature, there is a common opinion that the phase transition occurring at around room temperature worsens the properties of the cathode material. However, there is no experimental evidence for this.

The principal aim of the present work was to investigate phase transition in lithium manganese spinels near 280K. Elucidation of this phenomena can contribute in improving working properties of Li-ion batteries, for example increasing temperature stability.

Development of computer technologies and increase in computation power of PCs gives us the possibility to use efficiently well known Rietveld method to this quite specific group of objects.

The second aim was to check how far the Rietveld method can be extended for these compounds and especially for the nanocrystalline systems.

Investigations of the cubic and orthorhombic structures are the basis in understanding the nature of the phase transition in Li-Mn spinels. Knowledge of initial and final structures helps in verification of the sequence of phase changes using in situ XRD measurements. For these purposes design and construction of special environment cameras were needed.

Over the last years, investigations of the Li-Mn spinels were one of the main topics studied in our laboratory (Laboratory of X-ray Powder Diffractometry and Spectroscopy, Department of Catalysis on Metals, Institute of Physical Chemistry, Polish Academy of Sciences). This work was partially supported by research and PhD grants from KBN.

After acquiring an impedance spectrometer a possibility appeared to measure electrical characteristics simultaneously with measurements of structural parameters. However, this type of measurements needed redesigning and rebuilding of a dedicated environment

camera. The camera had to give the possibility to control temperature in certain range and atmosphere (not only air) giving at the same time possibility of simultaneous electrical and XRD measurements. This was a real challenge. Therefore, the third aim was constructing and testing new equipment and methods of recording of phase changes and verification of its course in the particular case of the Li-Mn spinels.

It should be noted that these new techniques tested in our laboratory on spinels of our interest can be of larger interest in studies of similar kind of phenomena (with accompanying changes in structural and electrical properties of the material under investigation) for other systems.

2. MATERIAL FOR INVESTIGATIONS

In the present thesis, three groups of lithium manganese spinels were investigated:

1) Spinels synthesized by sol-gel (low- and high-temperature) method

These lithium manganese spinels were prepared by sol-gel method according to the procedure described in details elsewhere, for example in [26]. Below is a summary of the procedure.

The appropriate amounts for the required final stoichiometry of $LiNO_3$ and $Mn(CH_3COO_2)\cdot 4H_2O$ were dissolved in a small amount of deionized water. At room temperature, droplets of concentrated ammonia were added until pH=9. The obtained colloid was dried at 90°C for 48 hours, calcined at 300°C for 24 hours (the SL and DL series were obtained in this way) and some was annealed at 800°C for 24 h and quenched to room temperature (the SH and DH series). As a result, low-temperature stoichiometric spinels (later on referred to as SL) with the assumed ratio Li/Mn=1:2, as well as "delta-spinel" with the ratio Li/Mn=1.005/1.995, were obtained (DL). The high-temperature series, the SH and DH, consist of a stoichiometric sample $LiMn_2O_4$ and the "delta-spinel" ($Li_{1.005}Mn_{1.995}O_4$) respectively.

The similar method of the synthesis (high and low temperature) was used for obtaining $Li_{1.20}Mn_{1.80}O_4$ samples, labeled $D_{20}L$ and $D_{20}H$ respectively and in detail described in [27].

All powder samples synthesized by sol-gel method and pellets SH and DH were kindly supplied by Prof. J. Molenda from Stanislaw Staszic University of Mining and Metallurgy in Cracow. The specifications and compositions of all the types of the samples are listed in Table 2.1.

2) Commercial spinel samples

Four commercial powders of lithium manganese oxide spinel were obtained from industrial suppliers:

2.1) $LiMn_2O_4$ - Sigma-Aldrich Co.

2.2) $LiMn_2O_4$ - Alfa Aesar Co. (purity 99.5%)

2.3) $Li_{1.0237}Mn_{1.9763}O_4$ - Honeywell Specialty Chemicals Co.

$Li_{1.0392}Mn_{1.9608}O_4$ - Honeywell Specialty Chemicals Co.

3) Derivative samples (treated samples)

The third group was obtained by heat treatment of some samples of the first and the second groups.

3.1) $LiMn_2O_4$ Sigma-Aldrich Co., heated up to 800°C

3.2) $LiMn_2O_4$ Alfa Aesar Co., heated up to 800°C

3.3) $LiMn_2O_4$ (low-temperature sol-gel method) heated up to 580°C

3.4) $Li_{1.005}Mn_{1.995}O_4$ (low-temperature sol-gel method) heated up to 580°C

3.5) $LiMn_2O_4$ (low-temperature sol-gel method) heated up to 800°C

3.6) $Li_{1.005}Mn_{1.995}O_4$ (low-temperature sol-gel method) heated up to 800°C

3.7) $Li_{1.20}Mn_{1.80}O_4$ (low-temperature sol-gel method) heated up to 600°C

3.8) $Li_{1.20}Mn_{1.80}O_4$ (low-temperature sol-gel method) heated up to 800°C

Samples	Composition	Additional notes
SL	$LiMn_2O_4$	low-temperature (300°C) sol-gel synthesis
DL	$Li_{1.005}Mn_{1.995}O_4$	low-temperature (300°C) sol-gel synthesis
SH	$LiMn_2O_4$	high-temperature (800°C) sol-gel synthesis
DH	$Li_{1.005}Mn_{1.995}O_4$	high-temperature (800°C) sol-gel synthesis
$D_{20}L$	$Li_{1.20}Mn_{1.80}O_4$	low-temperature (300°C) sol-gel synthesis
$D_{20}H$	$Li_{1.20}Mn_{1.80}O_4$	high-temperature (800°C) sol-gel synthesis
AA	$LiMn_2O_4$*	Alfa Aesar Co., *99.5% purity
AD	$LiMn_2O_4$	Sigma-Aldrich Co.
HDS10 HDS30	$Li_{1.0237}Mn_{1.9763}O_4$ $Li_{1.0392}Mn_{1.9608}O_4$	Honeywell Specialty Chemicals Co.

Table 2.1. Specification and composition of all the studied types of the samples.

2.1. Sample preparation for special experimental conditions

For in-situ X-ray diffraction experiments powder sample was spread onto a porous glass (Fig. 6.1. pos.1)

The samples for in-situ X-ray diffraction combined with impedance spectroscopy measurements were pressed into pellets of 10 mm in diameter and about 1mm thick (Fig. 6.2. pos.1). Pellets were sintered in air at 800°C and rapidly cooled (quick removal from the furnace). After polishing of surfaces using SiC emery paper up to 4000 grit, metal films

were deposited on both sides of the pellets by the dc sputtering (POLARON-SC502). In order to obtain from the sample x-ray a signal of appropriate intensity in the Debay non focusing geometry, the deposited metal film had to be thin. On the other hand, the film, serving as electrode, should have low electrical resistance measured along the surface. Therefore the proper balance between the thickness of the films and the intensity of the beam diffracted from the sample X-Ray had to be achieved. As electrodes, thin layers of gold, platinum and copper have been tested. Because of too much overlapping of the reflections from spinel on the XRD pattern, Au was not selected, although for electrical measurements only it can the best candidate. In the case of platinum electrodes it is extremely difficult to obtain the resistance measured along a surface less than 20Ω (sputtered in the same conditions it is almost 20 times that for Au). This can lead to an overestimated value of resistance during measurements in elevated temperatures.

Thus copper was found to be the most convenient electrode, because it offers low absorption of Cu Kα radiation, has relatively low resistance, is mechanically stable and reflections are not too much overlapping with those of the spinel.

3. USED METHODS AND TECHNIQUES

3.1. **The Rietveld method** (whole-pattern-fitting structure refinement)

Materials are especially important to our technology-based society: semiconductors in the electronic industry, oxides (spinels) as electrodes in the battery and energy storage industry, different other ceramics in medicine and engineering and, possibly in the future many other groups of materials.

In order to understand the properties of these materials and to improve them, their structure has to be known. An effective way to do this is by means of diffraction techniques. Most of our detailed understanding of the structures of crystalline materials has resulted from single-crystal X-ray and neutron diffraction experiments. This technique, using relatively large crystals of the material, gives a set of separate data from which the structure can be obtained. Unfortunately, for many substances of technical interest it has not been possible to grow or, in the case of minerals, find crystals that are suitable for single-crystal diffraction studies, so one has to resort to the powder diffraction technique using material in the form of very small crystallites. It is well known that many important materials for which structures have not been refined typically are finely crystalline and/or poorly ordered, for example manganese oxides, zeolites, clay minerals etc. In many of these cases where good single-crystals cannot be found, powder X-ray (or neutron) diffraction experiments provide an alternative, to single-crystal, method for structural studies.

Powder X-ray diffraction (XRD) has been an important standard tool for many decades for identification and characterization of many types of crystalline materials. The drawback of this conventional powder method is that the intensities from different reflections grossly overlap, thereby preventing proper determination of the structure, and accurate measuring of positions of Bragg intensities is strongly needed.

Two developments have kindled an interest in structural analysis using powder XRD data. Firstly, the introduction of computer-automated diffractometers has made it possible to collect routinely digitized data using a step-scan procedure. Secondly, the application of the Rietveld refinement method [28] to powder XRD data, which at least in part circumvents the peak overlap problem, has yielded successful refinements for an increasing number of crystal structures. The Rietveld method creates an effective separation of these overlapping data, thereby allowing an accurate determination of the structure. The Rietveld technique employs the entire powder diffraction pattern, thereby overcoming the problem of peak overlap and

allowing the maximum amount of information to be extracted from the pattern [29]. In the Rietveld method, each data point (2θ step) is an observation, and during the refinement procedure structural parameters, background coefficients, and profile parameters are varied in a least-squares procedure until the calculated powder profile, based on the starting structure model, best matches the observed pattern. This method was first applied to powder neutron diffraction data but was later adapted for use with X-ray data by Young et al. [30]. Powder XRD data have been used only relatively recently in Rietveld refinements because whereas peak shapes arising from constant-wavelength powder neutron diffraction experiments are close to Gaussian, those from powder XRD are considerably more complex and therefore more difficult to model. This disadvantage is, however, countered by the easy accessibility and smaller sample requirements for XRD as opposed to neutron diffraction experiments. These factors along with improvements in functions to describe powder XRD peak shapes have initiated a rapidly growing number of publications reporting Rietveld structure refinements using powder XRD data. A limitation of the Rietveld method is that one must start with a model that is a reasonable approximation of the actual structure, and it is therefore primarily a structure refinement, as opposed to structure solution technique. However, in some cases partial structure solutions are possible and thus the starting structure model available.

In addition to providing crystal structure information for materials that cannot be studied by single-crystal techniques powder XRD, the Rietveld method offers several other attractive features. Powder XRD data collection is usually rapid.. Thus Rietveld refinements are well suited for phase transformation studies, heating or cooling experiments, pressure studies, etc. Twinning is not a problem for powder diffraction studies, and in fact, might serve to help randomize the crystallite orientations in the powder sample. Rietveld refinements can yield very precise and, when performed with care, accurate unit-cell parameters, as well as quantitative analyses of mixtures. On the negative side, in addition to being mainly a refinement technique, atomic structural parameters (especially temperature factors) are, in general, less accurately determined than by comparable single-crystal studies. Also, sample-related problems such as structure disorder and preferred orientation of crystallites can affect the accuracies of the Bragg peak intensities, resulting in a poor or incorrect refined structure. Regardless the negative side, the technique has been so successful that the Rietveld method is now widely recognized to be uniquely valuable for structural analysis of nearly all classes of crystalline materials not available as single crystals. The success of the method can be judged

by the publication of more than a thousand scientific papers yearly presenting results with its using.

3.1.1. Mathematical aspects of Rietveld analysis

In the Rietveld method the least-squares refinements are carried out until the best fit is obtained between the entire observed powder diffraction pattern taken as a whole and the entire calculated pattern based on the simultaneously refined model for the crystal structure(s), diffraction optics effects, instrumental factors, and other specimen characteristics (e.g. lattice parameters) as may be desired and can be modelled. A key feature is the feedback, during refinement, between improving knowledge of the structure and improving allocation of the observed intensity to partially overlapping individual Bragg reflections.

The quantity minimized in the least-squares refinement is the residual, S_y:

$$S_y = \sum_i w_i (y_i - y_{ci})^2 \qquad (3.1)$$

where $w_i=1/y_i$ is the weighting factor

y_i-observed intensity at the i-th step,

y_{ci}-calculated intensity at the i-th step,

A powder diffraction pattern can be recorded in numerical form for a discrete set of scattering angles. This scattering variable is referred as T. Then, the experimental powder diffraction pattern is usually given as two arrays $\{T_i,y_i\}_{i=1,\ldots,n}$. In the case of data that have been manipulated or normalized in some way the three arrays $\{T_i,y_i,\sigma_i\}_{i=1,\ldots,n}$, where σ_i is the standard deviation of the profile intensity y_i, are needed in order to properly weight the residuals in the least squares procedure. The profile can be modelled using the calculated counts y_{ci} at the i-th step by summing the contribution from neighbouring Bragg reflections plus the background:

$$y_{c,i} = \sum_{\varphi} S_{\varphi} \sum_h I_{\varphi,h} \Omega (T_i - T_{\varphi,h}) + b_i \qquad (3.2)$$

The vector h(=H,or=H+k) labels the Bragg reflections, the subscript φ labels the *phase* and vary from 1 up to the number of *phases* existing in the model. In FullProf (reasons of choosing this Rietveld program are described in chapter 4.3.) the term *phase* is synonymous of a *same procedure for calculating the integrated intensities* $I_{\varphi,h}$. This includes the usual meaning of a phase and also the case of the magnetic contribution to scattering (treated

usually as a different *phase*) coming from a single crystallographic phase in the sample. The general expression of the integrated intensity is:

• $I_{\phi,h} = \{ LAPCF^{2} \}_{\phi,h}$ (3.2.1.)

• S_φ is the scale factor of the phase φ

• L_h contains the Lorentz, polarization and multiplicity factors

• F_h is the structure factor (The ratio of the intensities for the two wavelengths handled by the Rietveld program is absorbed in the calculation of F_h^2, so that only a single scale factor is required. For magnetic scattering F_h^2 is the square of the magnetic interaction vector)

• A_h is the absorption correction

• P_h is the preferred orientation function

• Ω is the reflection profile function that models both instrumental and sample effects

• C_h includes special corrections (non linearity, efficiencies, special absorption corrections, extinction, etc)

• b_i is the background intensity

The Rietveld Method consists of refining a crystal (and/or magnetic) structure by minimizing the weighted squared difference between the observed $\{y_i\}_{i=1,\ldots,n}$ and the calculated (2.2) pattern $\{y_{ci}(\alpha)\}_{i=1,\ldots,n}$ against the parameter vector $\alpha=(\alpha_1\alpha_2\alpha_3,\ldots\alpha_p)$. For FullProf, the function minimized in the Rietveld Method is:

$$\chi^2 = \sum_{i=1}^{n} \frac{1}{\sigma_i^2} \{ y_i - y_{c,i}(\alpha) \}^2 \qquad (3.3)$$

where, σ_i^2 is the variance of the "observation" y_i.

3.1.2. Criteria of fit

The quality of the agreement between observed and calculated profiles is measured by a set of (nowadays) conventional factors. In FullProf two sets of indices are calculated, according to the meaning of the integer *n*. In the first set *n* is the total number of points used in the refinement (*n* is equal to total number of points in the pattern minus total number of excluded points). In the second set only those points where there are Bragg contributions are taken into account. The definition of some of the often-used numerical criteria of fit is as follows:

- Profile Factor

$$R_P = 100 \frac{\sum_{i=1,n} | y_i - y_{c,i} |}{\sum_{i=1,n} | y_i |} \quad (3.4)$$

- Weighted Profile Factor

$$R_{wp} = 100 \sqrt{\frac{\sum w_i | y_i - y_{c,i} |^2}{\sum_{i=1,n} w_i y_i^2}} \quad (3.5)$$

- Expected Weighted Profile Factor

$$R_{expected} = 100 \sqrt{\frac{n-p}{\sum_i w_i y_i^2}} \quad (3.6)$$

where $(n-p)$ is the number of degrees of freedom, the meaning of n has been given above and p is the number of refined parameters.

- Reduced chi-square:

$$\chi_v^2 = \left[\frac{R_{wp}}{R_{expected}} \right]^2 = S^2 \quad (3.7)$$

- Goodness of fit indicator

$$S = \frac{R_{wp}}{R_{expected}} \quad (3.8)$$

- Bragg Factor:

$$R_B = 100 \frac{\sum_h | I_{obs,h} - I_{calc,h} |}{\sum_h | I_{obs,h} |} \quad (3.9)$$

- Crystallographic R_F- Factor:

$$R_F = 100 \frac{\sum_h | F_{obs,h} - F_{calc,h} |}{\sum_h | F_{obs,h} |} \quad (3.10)$$

The Rietveld refinement process will adjust the refinable parameters until the residual (in the least-squares method) is minimized in same sense. That is, a "best fit" of the entire

:alculated pattern to the entire observed pattern will be obtained. But the particular "best fit" obtained will depend on the adequacy of the model (i.e. does it contain the parameters needed to model the actual structure and diffraction conditions "well enough "?) and on whether a global minimum, rather than a local ("false") minimum, has been reached. One needs various criteria of fit in order to make these judgments. It is also important to have the same kinds of indicators reported at each cycle so that one can judge whether the refinement is proceeding satisfactorily and when the refinement has become sufficiently near to completion that it can be stopped.

Because "R-Bragg" and "R-structure factor" are based not on actually observed Bragg intensities but on those deduced with the help of the model, they are, therefore, biased in favour of the model being used. Nonetheless, they are the *R's* that are most nearly comparable to the conventional R-values quoted in the literature on single-crystal structure refinements. They also serve as a useful function because they are insensitive to misfits in the pattern that do not involve the Bragg intensities of the phase(s) being modelled.

From a purely mathematical point of view R_{wp} is the most meaningful of all these *R's* because the numerator is the residual being minimized. For the same reason it is also the one that best reflects the progress of the refinement.

Another useful numerical criterion is the "goodness of fit", S. An S value of 1.3 or less is usually considered to be quite satisfactory. The higher S value is probably a warning that you should look further into the reasons and question the adequacy of your model. On the other band, a small S may simply mean that the counting statistical errors far outweigh the model errors either because of poor counting statistics or because of high background which, being slowly varying in angle, is easily modelled. In the first case, a data set with better counting statistics would permit improved refinement of model details to better approximate the physical facts. As many guidelines has often said, "if your S value turns out to be significantly less than 1.00, you have surely done something wrong".

The experimental points within the *excluded regions* of diffraction pattern are always excluded from the calculation of all agreement factors. Conventional Rietveld R-Factors cR_p and cR_{wp} are calculated as above but using background-corrected counts. In the denominators the quantity y_i is changed to $(y_i\text{-}b_i.)$. The *observed* integrated intensity $I_{obs,h}$ is in fact calculated from the Rietveld formula:

$$I_{obs,h} = I_{calc,h} \sum_i \{ \frac{\Omega(T_i - T_h)(y_i - b_i)}{y_{c,i} - b_i} \} \qquad (3.11)$$

This formula is equivalent to a *proportional sharing* of the integrated intensity of a cluster between its components according to the actual model. Then, if the model contains a strictly zero integrated intensity for the reflection h (I_{calc}=0), the observed integrated intensity is also zeroed: $I_{obs,h}$ = 0, even if it is obvious that $I_{obs,h}$ is non zero from the experimental pattern. This has as a consequence that the reflections with $I_{calc,h}$=0 do not contribute to the Bragg R-factor.

The observed structure factor appearing in (3.10) is obtained from (3.11) corrected for multiplicity and the Lorentz-polarisation factor using the formula:

$$F_{obs,h} = \sqrt{\frac{I_{obs,h}}{L_h}} \tag{3.12}$$

Commonly used, the R_p, R_{wp} agreement factors are not satisfactory from a statistical point of view, therefore, a number of statistically more significant parameters are calculated by FullProf:

• The deviance [31] is defined as:

$$D = 2\sum_i \{y_i \ln(y_i / y_{c,i}) - (y_i - y_{c,i})\} \tag{3.13}$$

• From the deviance, one can derive two other measures of discrepancy which are useful as model selection criteria. These criteria take account of both the goodness of fit of a model and of the number of parameters used to achieve that fit. They take the form:

$$Q = D + a \cdot p \tag{3.14}$$

where p is the number of refined parameters and a=2 or a=ln(p) for different approaches.

• The Durbin-Watson statistic parameters: d and Q_D. The use of these two quantities to assess the quality of the refinement was advocated by Hill and Flack [32]. This statistic which measures the correlation between adjacent residuals (serial correlation) is defined as:

$$d = \sum_{i=2}^{n} \{[w_i(y_i - y_{c,i}) - w_{i-1}(y_i - y_{c,i-1})]^2\} / \sum_i \{[w_i(y_i - y_{c,i})]^2\} \tag{3.15}$$

Serial correlation is tested (at the 99.9% confidence level) by comparing the value of d to that of Q_D that is given by the relation:

$$Q_D = 2\{(n-1)/(n-p) - 3.091/(n+2)^{1/2}\} \tag{3.16}$$

Three cases may occur:

1) If $d < Q_D$, there is positive serial correlation: successive values of the residuals tend to have the same sign. This is the most common situation in profile refinement.

2) If $Q_D < d < 4- Q_D$, there is no correlation

3) If $d > 4-Q_D$, there is negative serial correlation: successive values of the residuals tend to have opposite sign.

A statistic strongly recommended by Hill and Flack [32] is the Durbin-Watson statistic, *d*. It is intended to reveal serial correlation between the successive y_i values. The ideal value for it is 2.00. It is now being routinely calculated in several of the more widely distributed programs for Rietveld refinement. Since the statistical errors in the intensity measurements at successive steps across reflection profile do not depend on each other, there is no serial correlation in a statistical sense. If, however, the calculated and observed profile functions just do not match well, whether for reasons of shape or area, there will be strong serial correlation of the residuals and the Durbin-Watson *d* will be far from its ideal value of 2.00. Thus, this *d* statistic can be a useful indicator of the quality of the fit of the calculated Bragg reflection profile functions to the actual observed profiles. Of course, it will be small (or large) if the areas, and therefore the integrated intensities which are of primary importance for crystal structure refinement, do not match. For that reason, *d* is usually small at the beginning of a refinement series and gets progressively larger (closer to 2.00) as the refinement progresses. But if the observed and calculated profiles have different shapes, the Durbin-Watson *d* will not become 2.00 even though the areas may be perfectly matched. As a useful hypothetical example, a Gaussian observed profile and a Lorentzian calculated profile with the same area, and recall that the Lorentzian has much longer "tails" than does the Gaussian profile. The intensity at each step in the central regions of the profiles will be higher on the Gaussian profile than on the Lorentzian profile while the converse will be true for the outer regions. The result will be that *d* will be significantly less than 2.00 for a non-statistical reason.

Numerical criteria are very important, but numbers are blind. It is imperative to use graphical criteria of fit, also, e.g. difference plots as well as plots of the observed and calculated patterns. That is particularly true when one is starting work on a new structure or a new sample or a new set of data for the "same" structure. Such plots often give immediate clues to the source of the problems one is having in getting the refinement started well. Large errors (e.g. in scale factor, lattice parameters, zero offset, wrong structure, strong phase contamination, etc.) are usually immediately obvious in the plots but not in the tables of numbers that are output from the refinements.

R_{wp} values can be seriously inflated by things which one can see at once in a difference plot and which do not arise from a poor structural model. An example we can see the lines in the difference plot which are not from the main phase and this it is strong enough to inflate

the R_{wp} value significantly. These lines can arise e.g. from the impurities. The difference plot made it very easy to note the presence of a second phase.

Conversely, R_{wp} values can be misleadingly small if the refined background is high: it is easier to get a good fit to a slowly varying background than to sets of Bragg reflection profiles.

It is then clear that both criteria, numerical and graphical, are needed for adequate evaluation of profile fitting. To perform correctly the Rietveld refinement procedure proper strategy of measurements and selection of starting parameters has to be done. These include: data collection, sample preparation, taking into account of background contribution, starting structural model as well as a choice of proper peak-shape function. There are in the literature numerous recommendations how to do it and what factors are influencing most the results. Summary of these recommendations is given in Annex I.

3.2 Scherrer method (technique for determination of the average crystallite size)

One of the most common applications of XRD analysis is to determine the crystallite size in poly- and nanocrystalline materials [33]. The finite size of the crystallite results in a broadening of the peaks in the XRD spectra. This can be understood by a simple analogy with optical diffraction if one considers that in a finite crystal the number of rays reflected from successive lattice planes that add up to produce constructive or destructive interference is finite and therefore they do not reinforce or cancel out completely. Inhomogeneous lattice strains, that is, variations in the lattice constants from one crystallite (coherent domain) to another, and structural faults will also result in a broadening of the diffraction peaks. All three effects are often simultaneously present, although structural faults may broaden some of the lines but not others.

The literature on the determination of the crystallite size from the broadening of the XRD lines is very extensive e.g. [34,35]. A simple treatment of finite-size broadening is given by Scherrer's equation: $D=k\lambda/(\beta\cos\theta)$ that was applied in the present work. To calculate the average crystallite sizes, broadening of the spinel 400 reflection was employed.

Practical use of Scherrer formula is described below.

$$D = \frac{k\lambda}{\Delta^{2\theta}_{RAD}\cos\theta}, \qquad \text{Scherrer equation} \qquad (3.17)$$

where:

D- the average crystallite dimension perpendicular to the reflecting phases

θ- the Bragg angle

$\Delta^{2\theta}_{RAD}$ - integral half width in radians (in some works denoted as β -the finite-size broadening)

k- Scherrer's constant close to unity that is related both to the crystallite shape and to the way β is defined, i.e., either as the full width at half-maximum (FWHM) or as the integral breadth (ratio of peak area to peak maximum).

λ- weighted average x-ray wavelength of Cu Kα radiation, (used in this work)

$$\lambda = \frac{2\lambda_{K\alpha_1} + \lambda_{K\alpha_2}}{3} = 1{,}5418\ \text{Å} \tag{3.18}$$

In the case of non-negligible contribution to the peak width of instrumental broadening the following equations were applied:

$$\begin{aligned} \partial^{2\theta}_{RAD} &= \sqrt{\Delta^2 - \partial^2_A} : \pi/180 \\ D &= \frac{\lambda}{\partial^{2\theta}_{RAD}\cos\theta} \end{aligned} \tag{3.19}$$

where:

Δ- integral half with of measured reflection

∂_A - instrumental broadening for standard (for example diffractometer quartz standard),here used 0.16° for peak of SiO_2 close 44°2θ

$\partial^{2\theta}_{RAD}$ - integral half width, with correction (in radians).

Some remarks on the applicability of Scherrer's equation are discussed in [34].That formula can be used to obtain an estimate of the crystallite size when there are no inhomogeneous strains and when the particle size distribution is narrow.

The finite-size broadening β can be determined from the experimentally observed line width, which needs to be corrected for instrumental errors such as finite slit width and the $K\alpha_1\alpha_2$ doublet of X-ray wavelength. If the line shape can be described by a Gaussian function, the square of the line breadth is the sum of the squares of the breadths originating from finite size, lattice distortion, and instrumental resolution. If the line shape follows a Cauchy (Lorentzian) function, the line breadth is a sum of the contributing breadths. Often, the experimental line shape shows better fit to a convolution of Gaussian and Cauchy functions, with size- and strain-broadened profiles approximated by Cauchy and Gaussian components, respectively.

In the present work to obtain accurate position (2θ) for each of a slow scanned diffraction peaks as well as a full width at half-maximum (FWHM) values or the integral breadth (β)

(ratio of peak area to peak maximum) a commercial Peakfit-3.11 program was used (Fig. 3.1.a). The peaks were fitted using Pearson VII function. This software was used also for separation of overlapped peaks (Fig. 3.1.b). After correcting the instrumental broadening, the remaining line broadening is assumed to be due to the crystallite size.

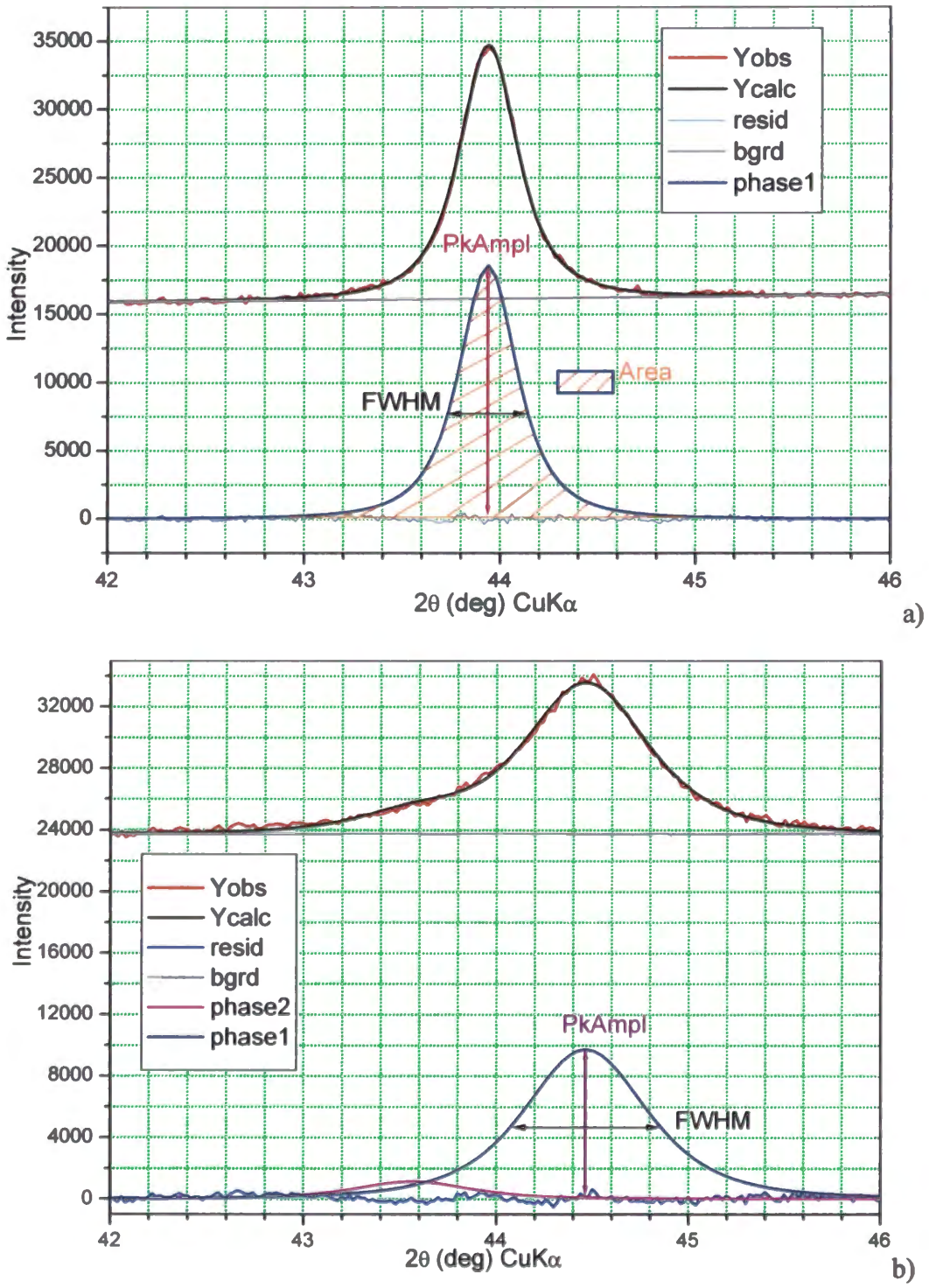

Fig. 3.1. Illustration of the fit and obtained peak parameters. a) for single phase sample, b) for multi phase sample.

3.3. Impedance spectroscopy

One of the most frequently used method for determination of electrical parameters is impedance spectroscopy [ex. 36, 37]. In this thesis two electrodes version of this technique is used. The method consists in measuring of modulus of the impedance (3.20) and phase angle between voltage signal and current signal. For such a type of measurements sinusoidal variable signal with low amplitude (10-30mV) is usually used. Frequency of that signal ω can be changed in wide range. The impedance:

$$Z=U(\omega)/I(\omega)=|Z|\cdot e^{-j\varphi}=Z'-jZ'' \tag{3.20}$$

where:

$Z'= |Z|\cdot\cos\varphi$ - real part of impedance - resistance

$Z''= |Z|\cdot\sin\varphi$ - imaginary part of impedance - reactance

φ - phase angle ($tg\varphi= Z''/Z'$)

$j=\sqrt{-1}$ - imaginary unit

Results of measurements can be presented in impedance or admittance representation. Between impedance Z and admittance Y there is following relationship:

$$Y= I(\omega)/U(\omega)=|Y|\cdot\cos\varphi+j|Y|\cdot\sin\varphi=Y'+jY''=G+jB \tag{3.21}$$

$$Y=1/Z \text{ and } Y'/Z'=Y''/Z'' \tag{3.22}$$

where: G-conductance, B-susceptance.

Impedance and admittance curves for some simple circuits of resistors R, capacitors C and (CPE) constant phase element P are shown in Fig.3.2. Admittance of a constant phase element is given by

$$Y(\omega)=A(j\omega)^n \tag{3.23}$$

where A and n are constant parameters ($0\leq n\leq 1$). When n=1, CPE is identical to ideal capacitor with capacity A, when n=0 CPE is equal to resistor with resistivity 1/A. Besides listed elements, more advanced elements can be constructed for description of some sophisticated phenomena of diffusion, dielectrical relaxation and others.

Intersections of semicircles or straight lines with real axis are determining values of resistance (conduction) of appropriate elements of the electrical circuit. Overlapping of impedance (admittance) semicircles can lead to difficulty with using simple graphical representation methods. It forces us to use computer fitting by least square method described in [38]. The equivalent electrical circuit consists of the elements which represent

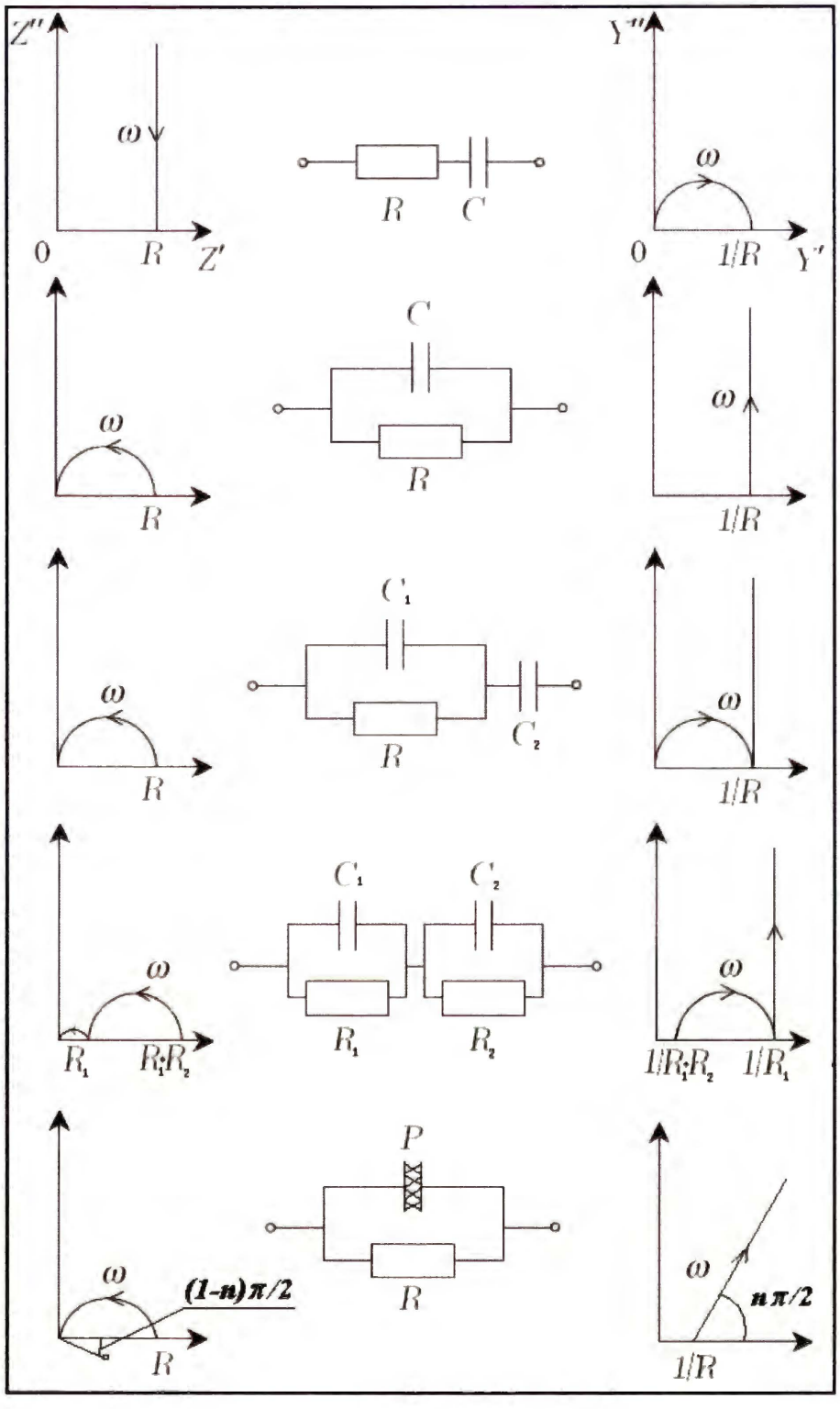

Fig. 3.2. Examples of impedance and admittance figures for simple circuits, built-up from resistors R, capacitors C and constant phase element P. [39].

different processes active in the investigated system: free charges transport, dielectrical relaxation, diffusion and adsorption-desorption phenomena and transport of charges

through electrode-sample interface. Proper selection of electrical equivalent circuit gives us possibility for correct interpretation of results.

Essential characteristic feature of the impedance spectroscopy method is a possibility of extrapolation of a part of the obtained semicircle, or the straight line, down to the intersections with the real axis. The intersection point lies often beyond the measurement range of the available equipment and can only be theoretically predicted.

From impedance spectroscopy measurements it is thus possible to obtain Z and φ. These data are needed for creation of impedance (admittance) curves. Then for a given shape of the curve we try to fit an equivalent electrical circuit for the investigated sample. It means, a circuit that can be characterized by the same impedance (admittance) curve, describing the response of the sample to electric excitation. Example of complex plane plot of impedance for the spinel sample is shown in Fig. 3.3.

In the present work, the electrical conductivity (σ) was obtained by reading coordinates of the crossing of an impedance semicircle with the real axis – value of resistance R. Taking into account geometrical factor a ($a=d/S$ where S is an area of each electrode, d is a distance between electrodes) we are receiving $\sigma = a/R$.

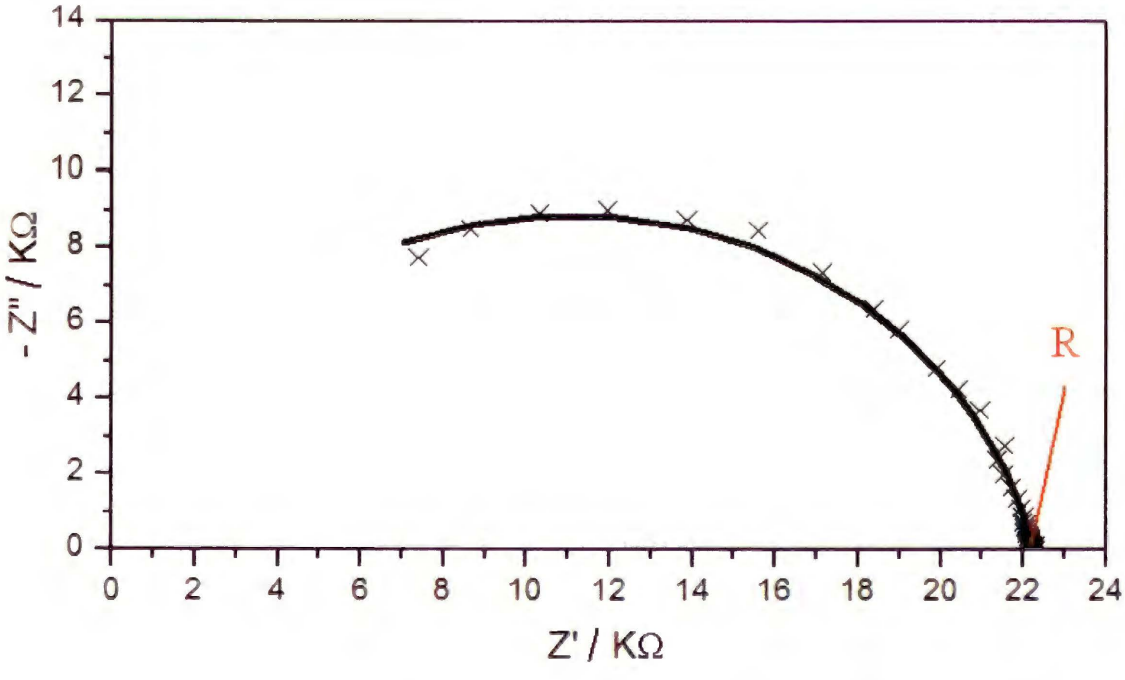

Fig. 3.3. Example of complex plane plot of impedance measured at 7°C for the spinel sample ($LiMn_2O_4$ Alfa Aesar heated up to 800°C) with sputtered copper electrodes. The solid line represents response of fitted equivalent circle of Fig. 7.1.

4. X-RAY POWDER DIFFRACTION STRUCTURAL MEASUREMENTS

Constructive interference of X-ray radiation occurs in a material when Bragg's law is satisfied:

$$2d\sin\theta = n\lambda \tag{4.1}$$

Where d is the distance between equivalent atomic planes, θ is the angle between the incident beam and these planes, *n* is an integer and λ is the wavelength. The scattered intensity can be measured as a function of scattering angle 2θ. In literature [40] is available a more sophisticated description of the theory of X-ray Diffraction written by M. von Laue, P. P. Ewald and others. Analysis of the resulting X-ray diffraction (XRD) pattern is an efficient method for determining the different phases present in the sample. Since the wavelength of X-rays used is of the same order of magnitude as the interatomic distances and bond lengths in crystalline solids (~1 Å), the XRD method serves well to determine the structure of crystalline materials.

The cubic structure of the $LiMn_2O_4$ material studied in this work facilitates the determination of the lattice parameter (a_c) from the diffraction data according to (4.2) and the same for orthorhombic structure (4.3).

$$\frac{1}{d_{hkl}^2} = \frac{h^2 + k^2 + l^2}{a_c^2} \tag{4.2}$$

$$\frac{1}{d_{hkl}^2} = \frac{h^2}{a_o^2} + \frac{k^2}{b_o^2} + \frac{l^2}{c_o^2} \tag{4.3}$$

Where *d* is the spacing of the crystal planes and h, k, l are the Miller indices of the measured reflection.

The X-Ray diffraction (XRD) method for polycrystalline (powder) materials studies was developed by Peter Debye and Paul Scherrer and independently Albert Hull, who used monochromatic X-ray radiation and powdered sample. When the sample is a powder, some of the crystallites will always be oriented so as to satisfy the Bragg condition (4.1).

The phase transition in electrode materials has been shown to be particularly amenable to study by in situ X-ray diffraction (XRD) methodology. Its advantage lies in its ability to monitor structural changes in the electrode material with changing temperature. This, combined with simultaneous electrical measurements, provides valuable information, inaccessible to ex situ experiments, on the relationship between structure and electrical properties.

In this work the X-ray structural measurements were performed in two arrangements: in classical diffractometer geometry with Bragg-Brentano focusing and step by step counting with preset values of step 2θ and counting time in a definite range of 2θ values; and in non focusing geometry with immobile sample.

Each of the type of the measuring geometries has its advantages and disadvantages and can be supplementary to each other when interpreting measured x-ray diffraction patterns of a given sample.

For the measurements under non ambient conditions for both the geometries, the diffractometer was fitted with one of the two types of laboratory made environmental cameras. (described in chapter 6) For the first type of camera, the powdered sample is spread on porous glass mounted on heating-cooling Peltier element (PE) serving as a sample holder. For the second type of camera, powder samples are pressed in pellets and mounted directly on a heater-cooler element (PE).The latter configuration was chosen for the combined XRD and electrical measurements. To avoid ice-covering at temperatures below $0^{o}C$, helium or dry air atmosphere were used in both arrangements.

4.1. The Bragg-Brentano geometry

This type of arrangement was provided using Siemens D5000 diffractometer (equipped with a horizontal goniometer) with θ-2θ geometry and Ni filtered Cu Kα radiation, powered at 40kV and 40mA. Data were collected in range of $2\theta=15^{o}$-95^{o}, (some data up to 140^{o}) with step interval of 0.02^{o} and counting time up to 12 second per step. Schematic representation of Bragg-Brentano focusing is presented in Fig 4.1.

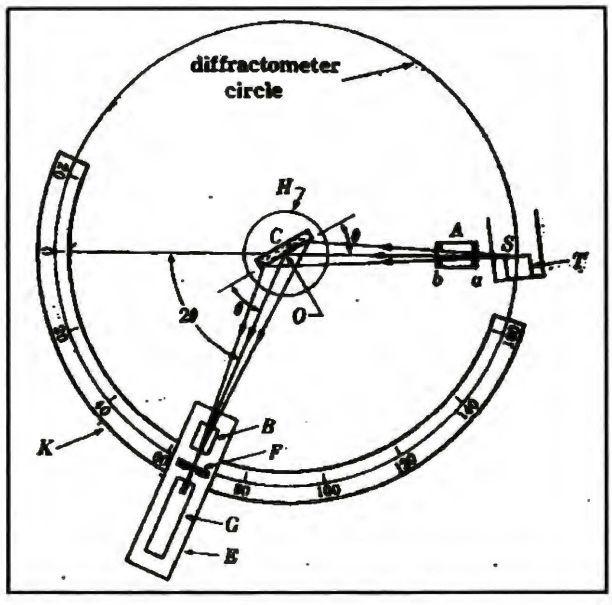

Fig. 4.1. Schematic representation of Bragg-Brentano focusing: T- x-ray tube, S- focus, A- set of slits a and b, O- goniometer axis, C- sample, H- table, B- receiving slit, F-incoming slit of counter, G- counter, E- arm of counter, K- angular scale.

XRD patterns collected in Bragg-Brentano arrangement can be used for Rietveld method of structure refinement. For obtaining suitable statistics in these measurements quite large counting time in every step is needed. Therefore this geometry can be used for investigation of structural parameters which do not change with time or change slowly. For many samples, in order to obtain reliable statistics, the whole measuring time of a pattern, under standard voltage and mA settings, is more than 12 hours. It means that the sample at the beginning of measurements can differ (from the point of view of its structure) from the one at the end of measurements. Thus, in such a case, the measurements are a compromise between measuring 2θ ranges and counting time. For example in our case some data were collected only around one peak that will be most representative for the interpretation of the phase transition.

4.2. Non focusing geometry

When non focusing geometry was applied, the XRD patterns were collected also with Siemens D5000 generator and Cu sealed-off tube. A diffractometer was used with flat graphite monochromator in the incident beam and an INEL CPS 120 position sensitive detector (PSD) was applied for data collection.

The non focusing case can be regarded as a classical Debye-Sherrer configuration. Capillary samples on such a setting correspond to the very classical Debye-Sherrer, while flat-plate specimens can be investigated in either reflection or transmission mode. Another difference from the conventional Debye-Sherrer method (Fig. 4.2.) is in the method of recording XRD pattern. Recording on the photo sensitive film is changed to electronic registration using CPS detector.

In our case the counter has the shape of a part of the ring (120^{o}) and the sample is placed at the central axis of this ring. Application of this type of detector allows recording of a wide part of the XRD pattern with good counting statistics and with a very short measuring time. Therefore CPS detectors can be used for *in situ* dynamic experiments. It means that there is the possibility to follow structural changes with time, studying, e.g., a process caused by temperature change. In the present work flat specimen and reflection geometry were used.

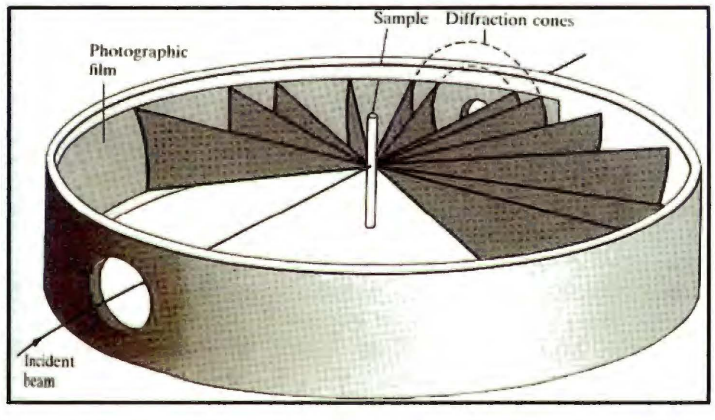

Fig. 4.2. The classical Debye-Sherrer setting.

This is a quite specific situation and is discussed in [41]. Examples of application to nanocrystal studies are given in [42]. In practice the incident x-ray beam (even after monochromatization) has some divergence and the reflected beam is focused on a certain reflecting angle, that angle being equal to the incidence angle (like in Bragg-Brentano geometry). Radiation reflected at other angles is not focused on the detector body. It results in some geometrical aberrations that cause deformation of the shape of recorded reflections.

It means that using this setting needs then a compromise between the whole time of measurement (must be conditioned by speed of structural changes), counting time

(intensity of peaks), and divergence of x-ray beam (acceptable geometrical aberrations). In measurements presented in this work the counting time between 180 and 300 seconds was found to be adequate to obtain good statistics for the interpretation of the XRD profiles. It is important to point out that investigations of structural parameter are of great interest in relation to other parameters, for example in correlation of x-ray and electric measurements, which was one of the aims of this work.

4.3. FullProf Suite - software instrument for Rietveld refinement

Almost as rapidly as the applications of the Rietveld method have proliferated, so have 'ıe versions of computer programs for carrying out the refinements. Although vastly odified and extended during several generations of evolution, many and perhaps most of ıem are recognizable descendants of Rietveld's original program [28,29] for which he ıreely distributed the source code. While most of those versions have been prepared only for local use, a few have been deliberately prepared and documented for general use.

Among a few very good freely distributed programs, (such us GSAS, DBWS, FullProf and others), which are currently well known; in the present work the FullProf was chosen for many reasons. This universal software is ultimately user friendly, so called FullProf-Suite consists of about sixteen useful programs. It is a powerful multipurpose set of programs. There are three main programs in this package.

First, the FullProf program [43] which has been mainly developed for Rietveld analysis (whole-pattern-fitting structure refinement) of neutron or X-ray powder diffraction data collected at constant or variable step in scattering angle 2θ. The program can be also used as a Profile Matching (or pattern decomposition) tool, without the knowledge of the structure. Single crystal refinement can also be performed alone or in combination with powder data. Time of flight (TOF) neutron data analysis is also available.

Second, WinPLOTR [44] - is a graphic software for plotting and for the analysis of powder diffraction patterns. It can be used to plot raw or normalized data files coming from neutron and X-ray diffractometers (conventional or synchrotron radiation) as well as Rietveld files created by the FullProf refinement program. WinPLOTR can also be used as a Graphical User Interface (GUI) for several programs used frequently in powder diffraction data analysis e.g.: FullProf-software partner refinement program, Dicvol,

SuperCELL or TREOR- automatic indexing programs, Mendel- periodic table, FullProf-Studio –visualization program and user defined programs.

Third, EdPCR - the new graphical editor for creating and modifying the PCR control input files.Additionally, in our case for more accurate control of PCR input files, an external PFE32 program was used .

The software is written in standard Fortran (77 or 90) language, WinPLOTR has been developed to run on PC's with a 32-bit Microsoft Windows operating system (supports Windows 9x/NT/2k and upper versions). The actual version of FullProf can be run on VAX, Alpha and Unix computers, Macintoshes and on PCs (supports Windows 9x/NT/2k and upper versions).

4.4. Using of quartz standard for selection of experimental conditions

For selection of proper experimental conditions several tests using quartz standard have been performed. After analysis of XRD pattern with different scanning steps (0.05, 0.01 and 0.01), step 0.02 was chosen because of reasonable good resolution and relatively short measurement time. Part of XRD pattern (near 212, 203, 301 reflections) of quartz standard is shown in Fig. 4.3. The recording of all five peaks (so called "fingers") confirm suitable resolution of used diffractometer arrangement.

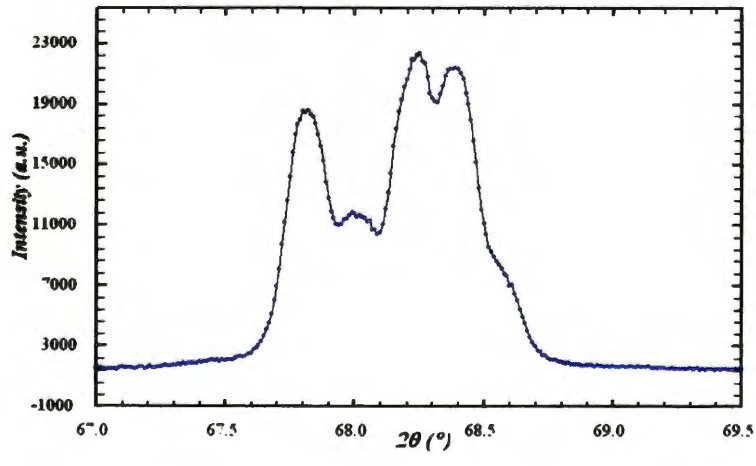

Fig. 4.3. Fragment of the SiO_2 XRD pattern collected with step width 0.02° 2θ.

For obtaining Instrumental Resolution Function that characterizes used diffractometer IRF-file containing Gauss U,V,W and Lorentz X,Y,Z FWHM (full width at half

maximum) parameters, the Rietveld analysis of powder quartz standard (SiO_2) was performed. These parameters were used in the subsequent refinement routines as standard values. Results of Rietveld refinement are presented in Tables 4.1., 4.2. and in Fig. 4.4.

$FWHM_G=(U\ tg\theta+V)\ tg\theta+W$ (4.4) $FWHM_L=X\ tg\theta+Y/cos\theta+Z$ (4.5)

For equations (4.1) and (4.2) the profile is assumed to be a Voigt type function.

wavelength	U	V	W	X	Y	Z
λ_1= 1.540560Å	0.008943	-0.009609	0.017175	0.029183	0.032250	0.013874
λ_2= 1.544330Å	0.010032	-0.008525	0.016336	0.029183	0.032250	0.013874

Table. 4.1. Gauss and Lorentz FWHM parameters obtained from Rietveld refinement of quartz standard.

Sample	t_M [°C]	Cell parameters [Å]	Volume [Å^3]	Bragg R-factor	RF factor
SiO_2 DRON powder standard	25	a=b=4.9146(7) c=5.4061(9) α=β=90° γ=120°	113.08	1.95	1.01

Table 4.2. Results of Rietveld refinement for SiO_2 (close JCPDS 33-1161; ICSD#89276)

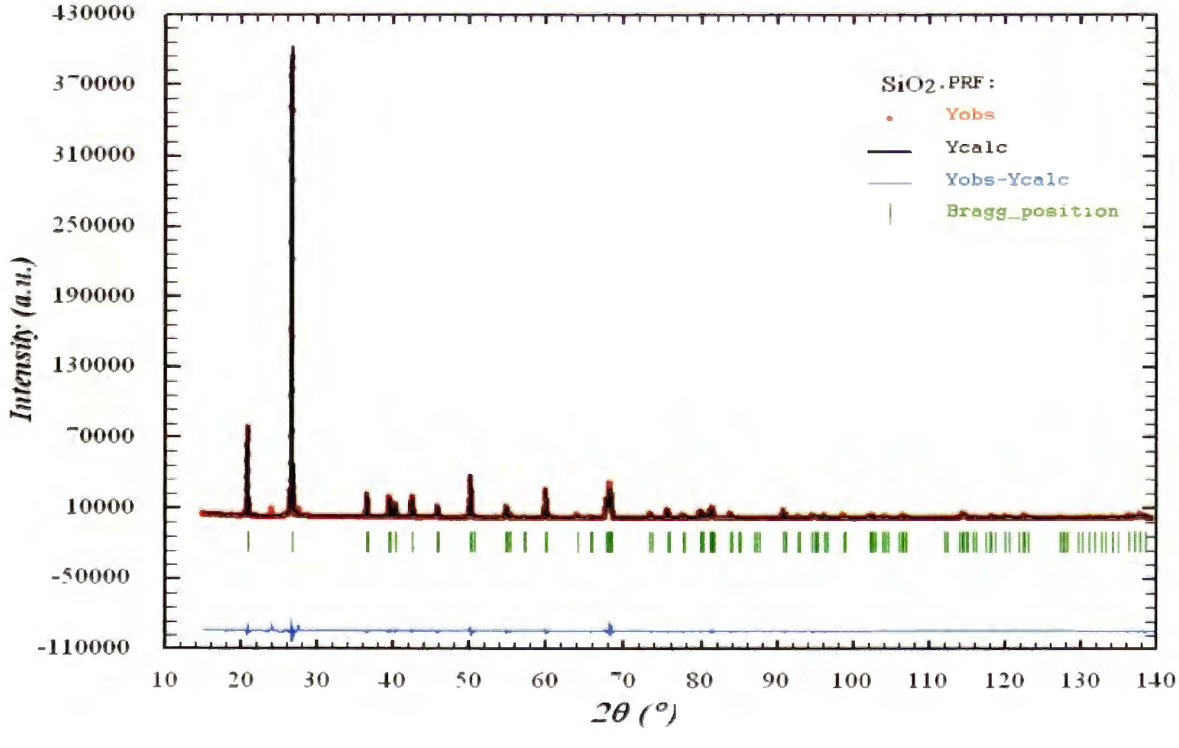

Fig. 4.4. Rietveld refinement for standard powder quartz (SiO_2) measured at 25°C.

Differences in resolution θ-2θ and non focusing geometries are shown on Fig. 4.5.

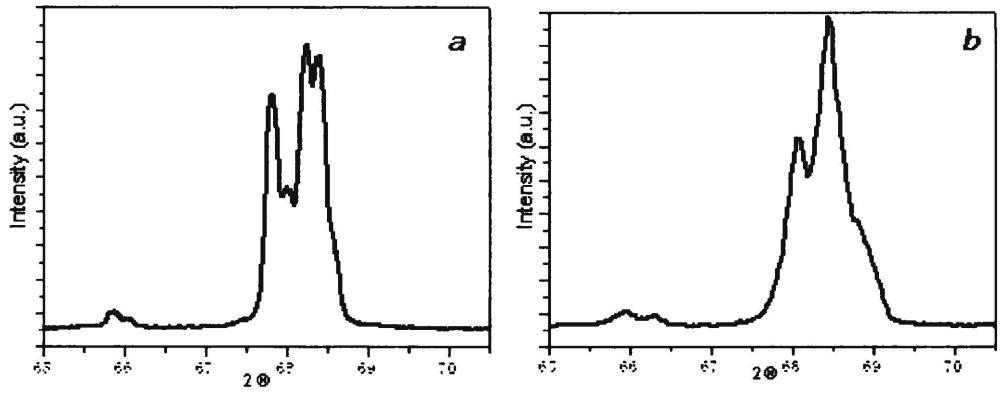

Fig. 4.5. Fragment of the SiO_2 XRD pattern collected a) using θ-2θ geometry, b) using non focusing arrangement.

5. IMPEDANCE SPECTROSCOPY MEASUREMENTS

For measurement of impedance in the frequency range between 1 MHz and 0.1 Hz an Autolab potentiostat PGSTAT30 with frequency response analyzer FRA2 was used. Sample impedance of absolute value in the range between 1Ω and 10GΩ can be measured using an a.c. signal as low as 20 mV. An additional advantage of the chosen equipment is the fact that the FRA software from Autolab allows incorporation of external routines into the measurement cycle, which makes the system adaptable to the needs of impedance measurements combined with X-ray diffractometry.

5.1 Simultaneous in-situ X-ray diffraction and impedance spectroscopy measurements

The experimental set-up had to fulfill the following requirements:

a) Allow fast XRD data collection in reflection geometry.
b) Perform impedance measurements on the sample simultaneously with XRD data collection . (or at predetermined sequence)
c) Allow measurements under controlled atmosphere at a programmed sequence of stabilized temperatures both below and above room temperature.

The scheme of the environment camera with beryllium window is presented in Fig.5.1. The base of the camera accommodates a number of feedthroughs. At its center, a Peltier cooling/heating element is mounted on a water cooler. The sample, in the mechanically stable form (a pellet) with thin metal films sputtered on opposite faces, is placed on a copper plate in thermal contact with the Peltier element. Two brass strips press the front face of the sample, leaving the central area exposed to the X-ray beam. The impedance analyzer is connected to the electrode films on the sample via the copper plate and the brass strips. A K-type shielded thermocouple is used as temperature sensor with an Eurotherm 2416 controller. The temperature can be varied between -25°C and 150°C. The cell can be flushed with dry air or helium in order to avoid water vapor condensation and deposition of ice on the sample surface at low temperature.

For X-ray diffraction measurements (like described in chapter devoted to X-ray measurements), Siemens D5000 diffractometer equipped with an INEL CPS-120 curved

position sensitive detector was used. A graphite monochromator was placed in the incident beam of Cu Kα radiation.

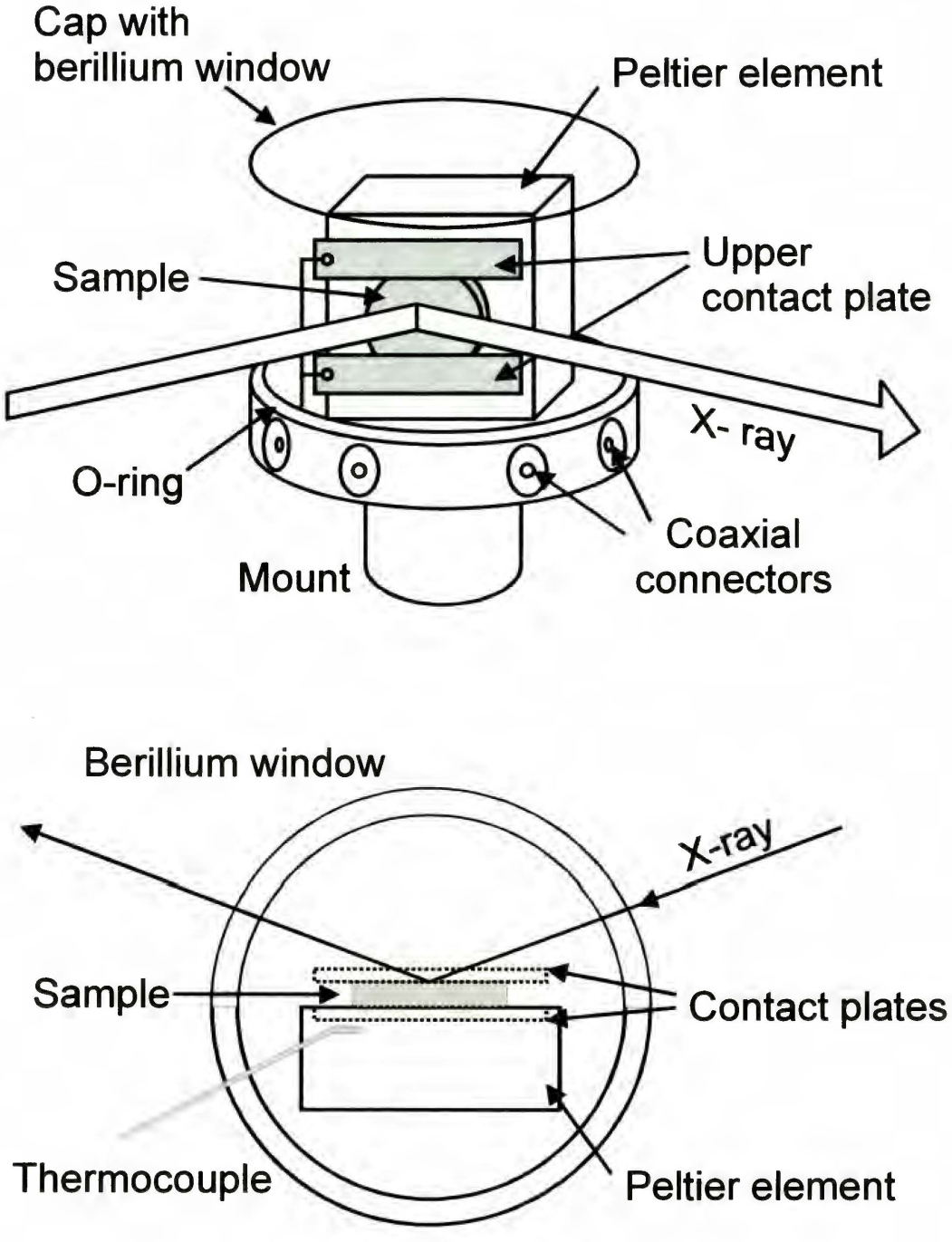

Fig. 5.1. The scheme of the environment camera for in-situ impedance spectroscopy and X-ray diffraction measurements: an overview (top), a cross-section view from above (bottom).

The mount of the camera was adapted to allow necessary geometrical corrections, especially the sample positioning at the axis of the goniometer. The position sensitive detector collects simultaneously a large part of a diffraction pattern, (for 2θ between 10 and 70 deg in the present study). Thus observations of structural changes with time, i.e., dynamic studies of structure evolution are possible. The main disadvantage is that, due to the immobility of the sample, the focusing geometry of the reflected beam can be met only within a limited, narrow range of diffraction angles. Therefore a rather narrow X-Ray beam has to be used. Additionally, due to the fact that the reflected radiation is recorded over a wide range of acceptance angles of the detector, there is a big chance that any spurious reflection (e.g. diffracted from the X-ray window of the camera) can be recorded. For the measurements presented in this work, the samples were positioned at an angle of about 20 deg with respect to the graphite-monochromatized incident Cu Kα radiation beam.

5.2 Experimental algorithm developed for combined XRD and impedance spectroscopy investigations

The flow chart and the scheme of the experimental set-up are presented in Fig. 5.2. and Fig. 5.3., respectively; The algorithm was implemented in developed using LabView-5.1 (National Instruments). The program runs on the computer controlling the impedance analyzer. The Autolab FRA program passes control to the LabView program using batch file execution. Synchronization of the X-ray pattern acquisition with measurement of impedance requires communication between computers controlling the two instruments. When the temperature of the sample is stable, the program triggers the measurement of an impedance spectrum and acquisition of an X-ray pattern. The time of accumulation of the diffraction pattern was adjusted to be approximately equal to the time of the impedance measurement (typically 15 minutes). The program proceeds to the next step when both computers signal completion of measurement. Timeout detection is provided to preserve continuity of the measurement cycle if one of the components fails. Advanced temperature control is implemented: stabilization within set criteria, multiple heating and cooling temperature ramps, detection of time dependence

of measured impedance (drift), recording of impedance spectra with values of temperature and drift.

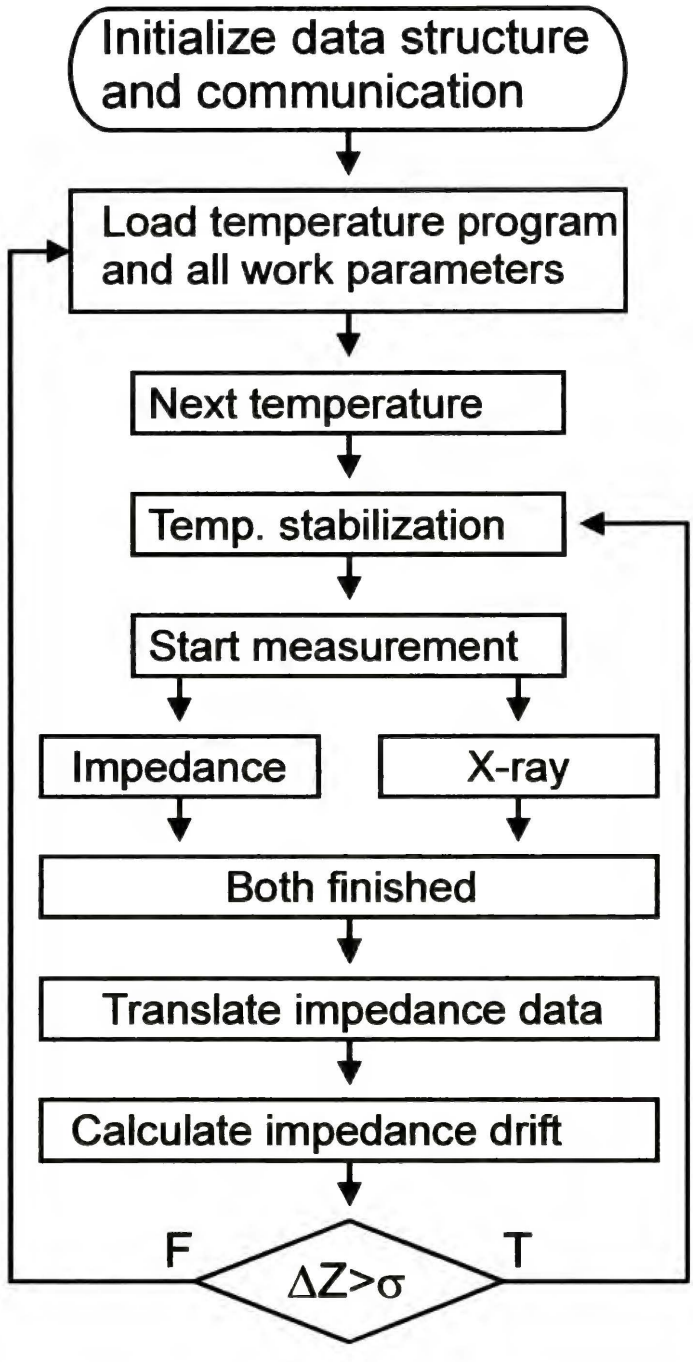

Fig 5.2. Flow chart of the combined X-ray diffraction and impedance spectroscopy measurements at programmed sequence of stabilized temperatures.

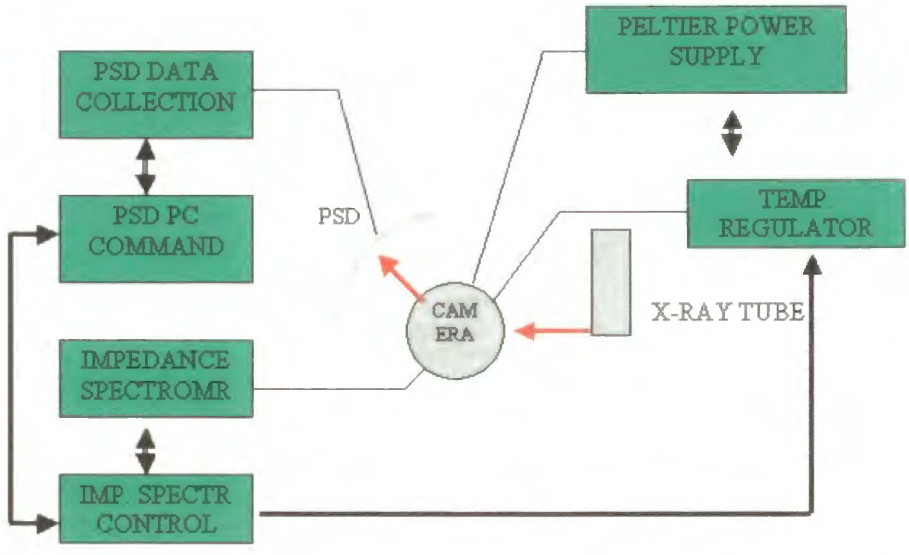

Fig. 5.3. The scheme of experimental set-up for simultaneous in-situ X-ray diffraction and impedance measurements, with marked main components.

Detection of impedance drift allows investigation of phase transition phenomena at semi-isothermal conditions. At the beginning of each impedance measurement, a test scan with a small number of points (e.g. two frequencies per decade from 100kHz to 1Hz) is executed. The test scan is repeated after measurement of the entire impedance spectrum, which lasts several minutes. The impedance drift ΔZ is calculated as the relative root-mean-square difference between the two sets of values: Z_1 and Z_2, measured at N test frequencies ω_i:

$$\Delta Z = \left[\frac{1}{N} \sum_{i=1}^{N} \left| Z_1(\omega_i) - Z_2(\omega_i) \right|^2 \times \left| Z_1(\omega_i) \right|^{-2} \right]^{1/2} \tag{5.1}$$

Measurements of impedance spectra and X-ray patterns are repeated at the same temperature until drift of the impedance is below the set limit.

6. EQUIPMENT DEVELOPED FOR IN-SITU EXPERIMENTS

For performing experiments in non ambient condition and particularly for in situ measurements it was indispensable to design and construct special environmental cameras. For investigation described in this thesis two generation of XRD cameras were designed and produced.

6.1. XRD camera for in-situ studies

To meet the desired goals using available X-Ray equipment, it was necessary to provide vertical mounting of a flat sample with the simultaneous possibility of its heating and cooling in a definite temperature range. For this purpose, as a sample holder and heater/cooler, a water-cooled Peltier element was used. Electric feedthrough assured connection of the thermocouple and power supply. To avoid ice covering of the samples the camera was flushed either with dry air or dry helium.The X-Ray window was from a thin Beryllium foil. The temperature control was ensured by using a thermocouple connected to a Eurotherm 2416 temperature controller. In Fig. 6.1. are shown photos of the camera.

6.2. Environmental camera for simultaneous XRD and impedance spectroscopy measurements

This camera was a development of the above described one. It is presented in Fig. 6.2. Principal parameters are the same. However, due to the fact that simultaneously with recording XRD spectra the electric parameters are to be measured, the camera had to possess some additional elements. The base of the camera had to accommodate larger number of feed-throughs. Additionally, a more efficient Peltier cooling/heating element had to be mounted on a water cooler element. There were also special requirements with respect to the sample under study. It was in the form of a pellet with thin metal films sputtered on opposite faces and was placed on a copper plate which is in thermal contact with the Peltier element. Two brass strips, serving as electric contacts, press the front face of the sample, leaving the central area exposed to the X-ray beam. The impedance analyzer is connected to the electrode films on the sample via the copper plate and the brass strips. A K-type shielded thermocouple is used as a temperature sensor with an Eurotherm 2416 controller. In the constructed camera the temperature can be varied between -25°C and 100°C. As before, the cell can also be flushed

with dry air or helium in order to avoid water vapor condensation and deposition of ice on the sample surface at low temperature.

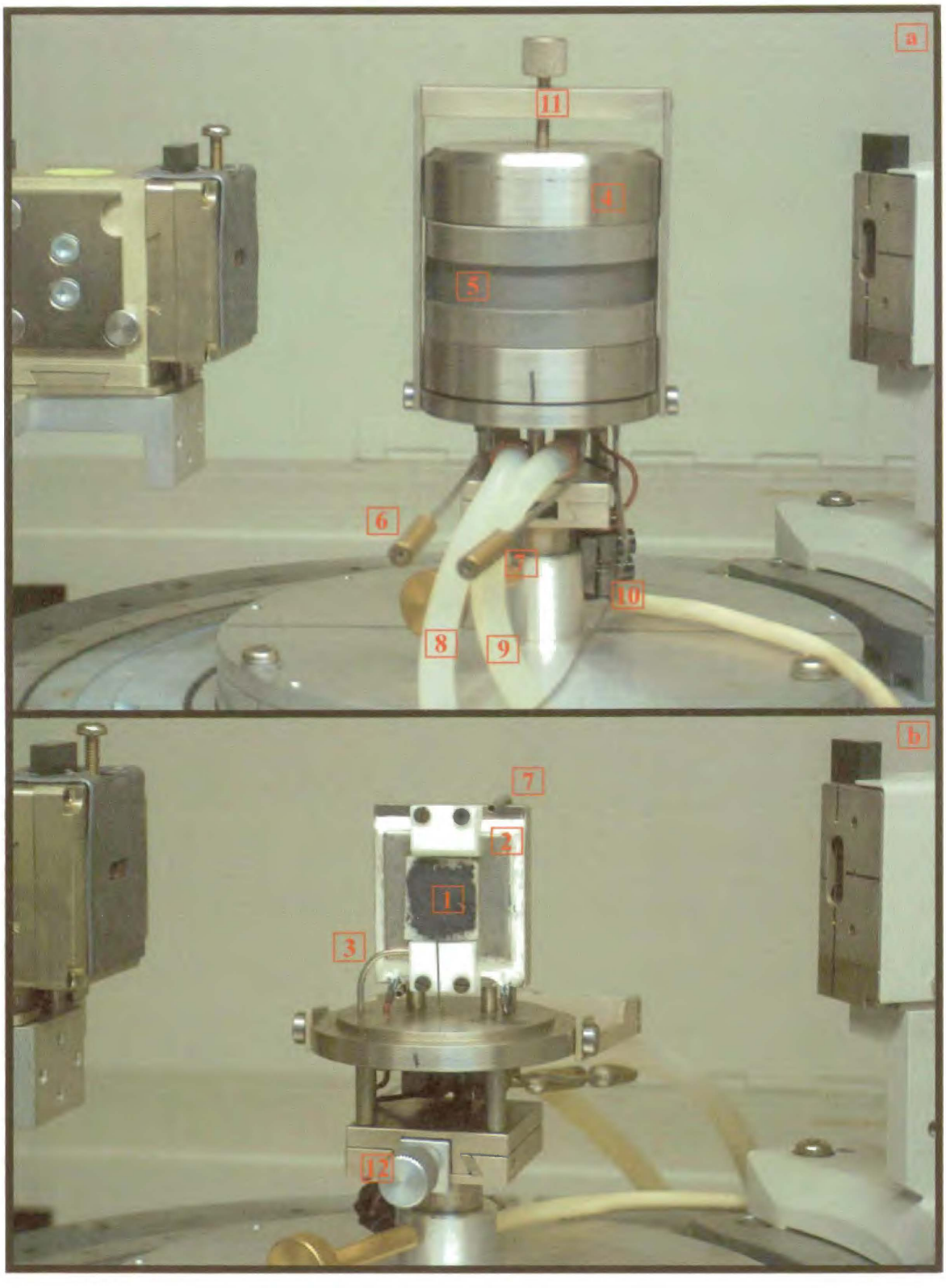

Fig. 6.1. Environmental camera for in situ XRD measurements.

a) with cap, b) without cap. 1-sample spread on porous glass; 2-Peltiere element (PE) heater-cooler; 3-lead for thermocouple connected to Omega temperature controller; 4-cap; 5-measurement window covered with Be foil; 6,7-gas inlet/outlet; 8,9-cooling water in/out; 10-electrical feed for PE; 11-cramp with fixing screw; 12-adjustment screw.

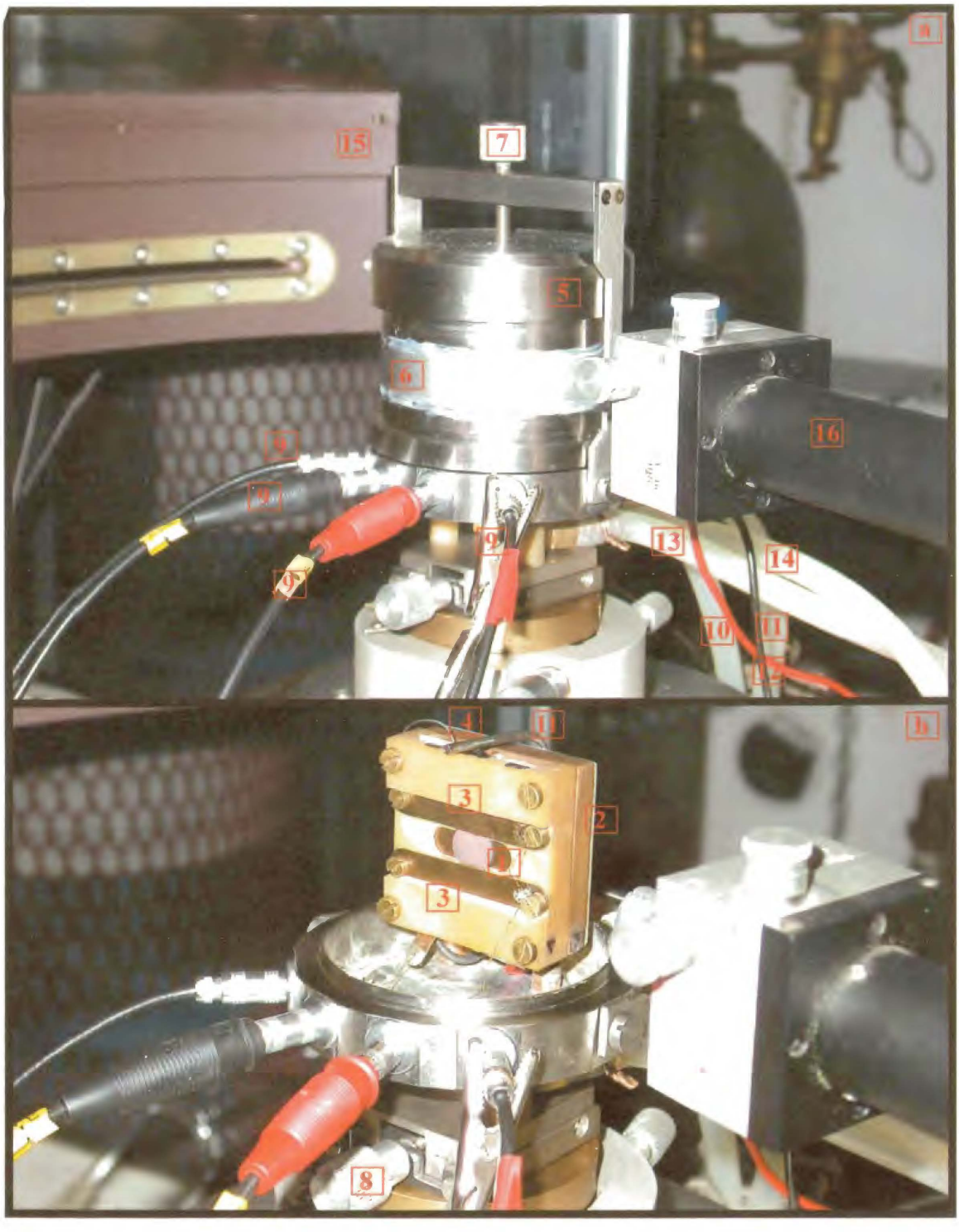

Fig. 6.2. Environmental camera for in situ XRD and electrical measurements.

a) with cap, b) without cap. 1-powder sample pressed in pellet with deposited Cu electrodes; 2-Peltiere element (PE) heater-cooler; 3-springing electrical contacts; 4-thermocouple connected to Eurotherm temperature controller; 5-cap; 6-measurement window made of Be foil; 7-cramp with fixing screw; 8-adjustment screw; 9-electrical contacts 10,11-gas inlet/outlet; 12-electrical feed for PE; 13,14-cooling water in/out; 15-INEL CPS120 position sensitive detector; 16-X-ray lead.

7. RESULTS OF MEASUREMENTS AND CALCULATIONS

Below are summarized: first shortly the procedures and methods used for data elaboration and next the results obtained for each kind of the investigated sample. For all investigated samples (listed in Table 7.1.), the Rietveld refinement procedure was applied for structure identification and phase composition analysis.

In commercial (Alfa Aesar Co. and Sigma - Aldrich Co.) spinels impurity phases, which were not specified by producers, were found and identified.

In the case of laboratory obtained spinels, synthesized by low temperature sol-gel method, three phases were found and described in materials supposed to contain only one phase.

For samples which undergo phase transitions, parameters of low temperature phases were found and described.

In parallel to the full profile analysis (by the Rietveld refinement method) single peak analysis was also employed. From broadening of a given peak the average crystallite size was calculated for all investigated samples. Results are shown in Table 7.2.

The Rietveld analysis was performed following the general recommendations given in Annex I.

The data were collected in the widest possible range of the 2θ diffraction angles of the used experimental set up, which was limited by the inherent feature of the XRD environmental camera with beryllium window.

The counting time was chosen 10-12 second per step (0.02^{o}) in order to provide the intensity of the highest reflection no less than several ten thousands counts.

Before starting measurements the calibration of diffractometer was performed using quartz standard and sets of preliminary measurements were performed on different samples to determine the optimal condition for further series of measurements.

The powder samples were additionally milled to "flour condition" to avoid so- called "rock in the dust" situation.

The background for XRD patterns was traced by point by point procedure with subsequent refinement of position of the selected points (using one of the internal algorithms of FullProf program).

The starting model for Rietveld refinement procedure was adopted using data from International Tables for Crystallography and completed using files from Inorganic Crystal Structure Database (ICSD).

Thompson-Cox-Hastings pseudo Voight function was employed to approximate peak shape function to achieve best fitting of calculated peaks to the experimentally observed ones.

Sequence of refining parameters of the starting model was taken from [45]. According to this procedure the first step was a refinement of global parameters (zero-shift, displacement and transparency), the second was refining of the profile parameters (cell constants, asymmetry, overall displacement, temperature, preferred orientation parameters, strains, size and propagation vectors) and the third step was refining of atomic parameters (coordinates, site occupancies and isotropic displacement temperature factors). The next stage was refining of the background point positions. The final stage was a simultaneous refinement of the all introduced parameters.

For samples for which it was possible to produce pellets with sufficient mechanical strengths simultaneous XRD and impedance spectroscopy measurements were performed.

The impedance spectra were analysed by fitting parameters of an equivalent circuit shown in Fig. 7.1.

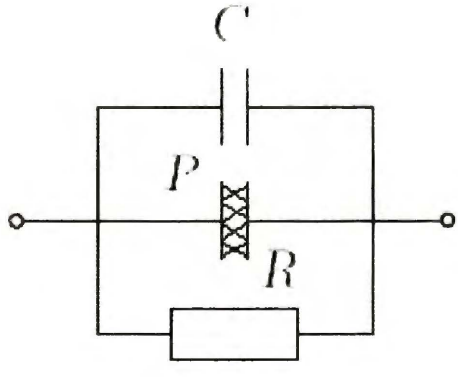

Fig. 7.1. Equivalent circuit used to model the ac response of lithium manganese spinel samples measured using Autolab FRA2 impedance analyzer.

Due to the fact that the research of electrical properties of these systems are not the main subject of this work, the necessary details concerning these measurements were published elsewhere [46,47].

In the spinels the 400 reflection of cubic phase undergoes splitting in the orthorhombic phase into 400, 040 and 004. This splitting is a function of the extent of the phase transition and change in due course of the temperature treatment. After complete phase transformation the peak can be decomposed into three reflections of the orthorhombic phase (Fig. 7.2.a). But this peak can be also approximated by a fitting of a single reflection

(Fig. 7.2.b). This approach was applied in this work to follow the temperature structural change. The value of FWHM was obtained using PeakFit software with Pearson VII type analytical functions.

Temperature dependence curves for FWHM calculated this way have been correlated with temperature dependence of resistance and are given in chapters 7.2.,7.3.,7.4.and 7.5.

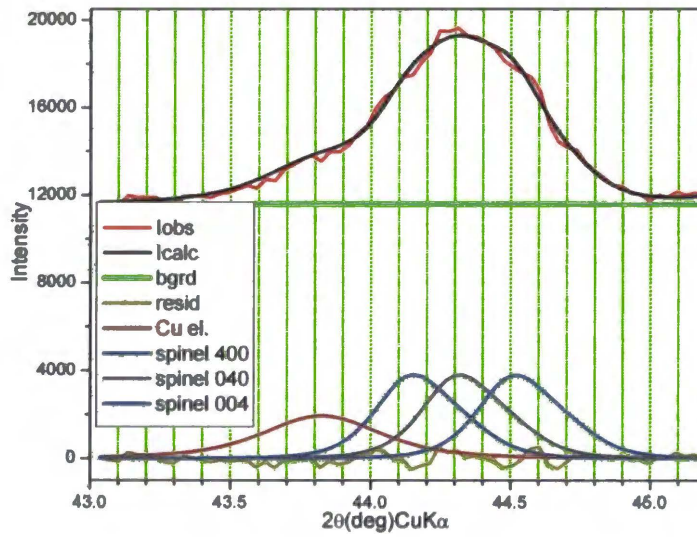

a)

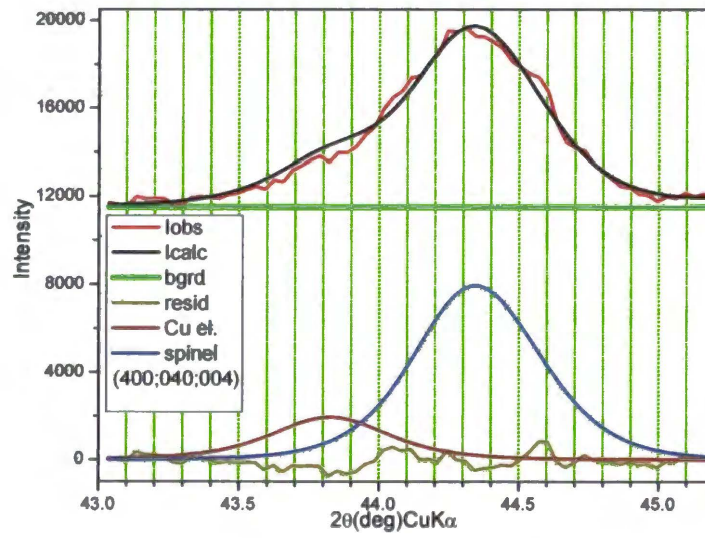

b)

Fig.7.2. XRD pattern measured in non focusing geometry for $LiMn_2O_4$ sample (high temperature sol-gel synthesis), measured at 14°C (shown only small part around 44° (2θ)). a) complex peak fitted as three separate reflections and b) complex peak fitted as one reflection. The Cu 111 reflection from electrode is taken into account during fitting.

N	Name	Formula	measurement T[°C]	Heat treatment / How to get
1	SL	$LiMn_2O_4$	25	During synthesis heated up to 300°C
2	DL	$Li_{1.005}Mn_{1.995}O_4$	25	During synthesis heated up to 300°C
3	SH	$LiMn_2O_4$	25	During synthesis heated up to 800°C
4	DH	$Li_{1.005}Mn_{1.995}O_4$	25	During synthesis heated up to 800°C
5	DL_{20}	$Li_{1.20}Mn_{1.80}O_4$	25	During synthesis heated up to 300°C
6	DH_{20}	$Li_{1.20}Mn_{1.80}O_4$	25	During synthesis heated up to 800°C
7	HDS10	$Li_{1.0237}Mn_{1.9763}O_4$	25	Industrial suppliers
8	HDS30	$Li_{1.0392}Mn_{1.9608}O_4$	25	Industrial suppliers
9	Aldrich	$LiMn_2O_4$	25	Industrial suppliers
10	Alfa Aesar	$LiMn_2O_4$	25	Industrial suppliers
*	*	*	*	*
11	SLh580	$LiMn_2O_4$	25	SL sample heated up to 580°C
12	DLh580	$Li_{1.005}Mn_{1.995}O_4$	25	DL sample heated up to 580°C
13	SLh800	$LiMn_2O_4$	25	SL sample heated up to 800°C
14	DLh800	$Li_{1.005}Mn_{1.995}O_4$	25	DL sample heated up to 800°C
15	SHm4	$LiMn_2O_4$	-4	Low temperature measurement
16	DHm4	$Li_{1.005}Mn_{1.995}O_4$	-4	Low temperature measurement
17	$DL_{20}600$	$Li_{1.20}Mn_{1.80}O_4$	25	DL_{20} sample heated up to 600°C
18	$DL_{20}800$	$Li_{1.20}Mn_{1.80}O_4$	25	DL_{20} sample heated up to 800°C
19	Aldrich	$LiMn_2O_4$	50	Elevated temperature measurement
20	Alfa Aesar	$LiMn_2O_4$	50	Elevated temperature measurement
21	Aldrich	$LiMn_2O_4$	-25	Low temperature measurement
22	Alfa Aesar	$LiMn_2O_4$	-25	Low temperature measurement
23	Aldrich 800	$LiMn_2O_4$	50	Elevated temperature measurement
24	Alfa Aesar800	$LiMn_2O_4$	50	Elevated temperature measurement
25	Aldrich 800	$LiMn_2O_4$	-25	Low temperature measurement
26	Alfa Aesar800	$LiMn_2O_4$	-25	Low temperature measurement

Table. 7.1. List of the samples for which Rietveld refinement procedure was applied. *Samples 11-26 are derivatives from samples 1-10.

Since principal interests in this work are nano-compounds, therefore for all the investigated samples the average crystallite size calculations were performed first. For this, Scherrer equation was used and the broadening of the spinel 400 and 222 reflections was considered. Diffraction patterns were collected in the standard Bragg-Brentano geometry; the same patterns were used for Rietveld refinement.

In the case of multiphase samples the average crystallite size calculation was performed for the dominant phase.

Sample	Temperature of measurement [°C]	Av. cryst. size [nm] (calc. from 400 peak)	Av. cryst. size [nm] (calc. from 222 peak)
Alfa Aesar	50	30	34
Alfa Aesar800	50	32	41
Aldrich	50	35	37
Aldrich800	50	40	44
HDS10	25	36	39
HDS30	25	38	40
SL	25	11	17
DL	25	10	16
SH	25	36	42
DH	25	35	44
DL_{20}	25	10	16
DH_{20}	25	26	34
SLh580	25	27	31
DLh580	25	30	36
SLh800	25	35	42
DLh800	25	33	38
$DL_{20}600$	25	23	29
$DL_{20}800$	25	33	39

Table 7.2. Average crystallite size of different lithium manganese spinels.

The average crystallite size was also calculated for samples measured in temperatures below 0°C (i.e. after phase transition into orthorhombic phase) and no change was observed in respect to the measurements performed before phase transformations (i.e. for cubic phase). The observed differences in average crystallites sizes calculated from 400 and 111 reflections need, however, some comments. The values calculated from the 400 reflection are systematically lower. The cause can be either the broadening by microstrains present in the samples or the fact that in the calculations of average particle sizes the coefficient K in the Scherrer's formula was put equal to one. This coefficient depends however on both particle shape and the hkl of a given reflection. Nevertheless the observed difference is small and the results confirm that all the investigated samples are in the nano range.

Below are the typical examples of results obtained for each type of the studied samples.

7.1. $LiMn_2O_4$ and $Li_{1.005}Mn_{1.995}O_4$ synthesized by low temperature sol-gel method

Results of Rietveld analysis are shown in Fig. 7.3., Fig. 7.4. and Table 7.3.

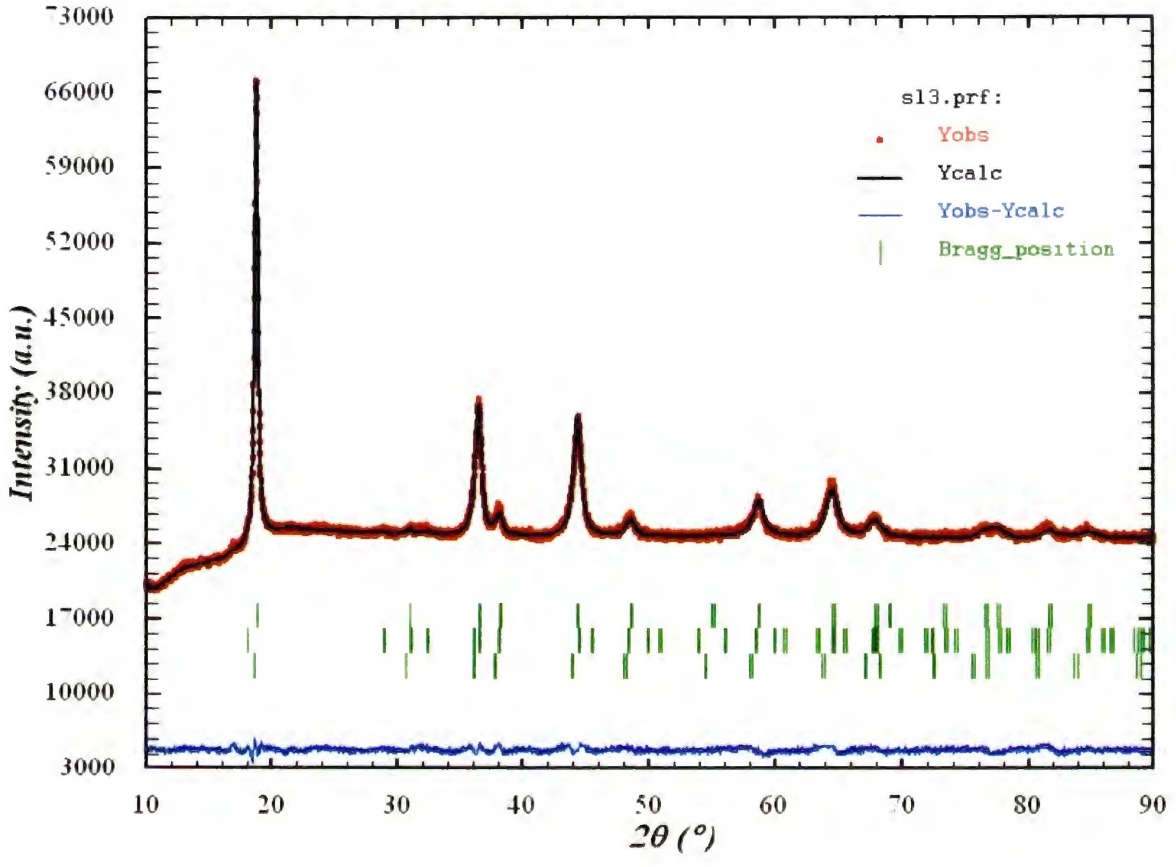

Fig. 7.3. Graphical results of Rietveld refinement for $LiMn_2O_4$ sample (low temperature sol-gel synthesis), sample measured at 25°C.

At 25°C the samples consist of following three phases:

Phase 1: Lithium Manganese Oxide, spinel $Li_4Mn_5O_{12}$ (4/5/12), similar to JCPDS card no. 46-0810, number of Space group: 227, Hermann-Mauguin Symbol: Fd-3m, Crystal System: Cubic, Laue Class: m-3m, Point Group: m-3m, Bravais Lattice: F, Lattice Symbol: cF.

Phase 2: Lithium Manganese Oxide, cubic spinel $LiMn_2O_4$(1/2/4), close to ICSD card no. 40485 and JCPDS card no. 35-0782, number of Space group: 227, Hermann-Mauguin Symbol: Fd-3m, Crystal System: Cubic, Laue Class: m-3m, Point Group: m-3m, Bravais Lattice: F, Lattice Symbol: cF.

Phase 3: Dimanganese (III) Manganese Oxide, Mn_3O_4, Hausmannite, close to ICSD card no. 68174 and JCPDS card no. 80-0382, number of Space group: 141, Hermann-Mauguin

Symbol: I 41/A M D, Crystal System: Tetragonal, Laue Class: 4/mmm, Point Group: 4/mmm Bravais Lattice: I, Lattice Symbol: tI.

Sample	t_{meas} [°C]	Cell parameters [Å] of phases	Fract. (%)	Volume [Å^3]	Bragg R-factor	RF factor
$LiMn_2O_4$	25	1) $Li_4Mn_5O_{12}$:	1)	543.79	2.52	1.88
		$\alpha=\beta=\gamma=90^o$	95.45			
Sol-gel		a=b=c=8.1623(4).	±1.89			
heated up		2) $LiMn_2O_4$:	2)	561.12	6.61	4.55
to 300°C		$\alpha=\beta=\gamma=90^o$	3.47			
during		a=b=c=8.2481(3).	±0.55			
synthesis		3) Mn_3O_4 :	3)	313.82	16.1	7.25
		$\alpha=\beta=\gamma=90^o$, a=5.7651(9),	1.08			
		b=5.7651(9), c=9.4422 (9)	±0.16			
$Li_{1.005}Mn_{1.995}O_4$	25	1) $Li_4Mn_5O_{12}$:	1)	543.61	2.86	2.64
		$\alpha=\beta=\gamma=90^o$	93.86			
Sol-gel		a=b=c=8.1614(3).	±1.26			
heated up		2) $LiMn_2O_4$:	2)	561.16	5.15	4.32
to 300°C		$\alpha=\beta=\gamma=90^o$	4.36			
during		a=b=c=8.2483(4).	±0.26			
synthesis		3) Mn_3O_4 :	3)	313.82	12.4	7.19
		$\alpha=\beta=\gamma=90^o$, a=5.7651(9),	1.78			
		b=5.7651(9), c=9.4422 (9)	±0.17			

Table 7.3. Numerical results of Rietveld refinement for $LiMn_2O_4$ and $Li_{1.005}Mn_{1.995}O_4$ (low temperature sol-gel synthesis).

Sample	t_{treat} [°C]	Cell parameters [Å] of the individual phases	Fract. (%)	Volume [Å^3]	Bragg R-factor	RF factor
$LiMn_2O_4$ Sol-gel heated up to 300°C during synthesis	580	1) $LiMn_2O_4$: $\alpha=\beta=\gamma=90^o$ a=b=c=8.2295(3).	≈99	557.34	3.75	2.11
		2) $Mn_{3\pm x}O_{4\pm y}$	≈1	-	-	-
$Li_{1.005}Mn_{1.995}O_4$ Sol-gel heated up to 300°C during synthesis	580	1) $LiMn_2O_4$: $\alpha=\beta=\gamma=90^o$ a=b=c=8.2369(5).	≈99	558.84	5.74	3.08
		2) $Mn_{2\pm x}O_{3\pm y}$	≤1	-	-	-

Table 7.4. Numerical results of Rietveld refinement for $LiMn_2O_4$ and $Li_{1.005}Mn_{1.995}O_4$ (low temperature sol-gel synthesis), additionally heated up to 580°C; the measurements performed at 25°C.

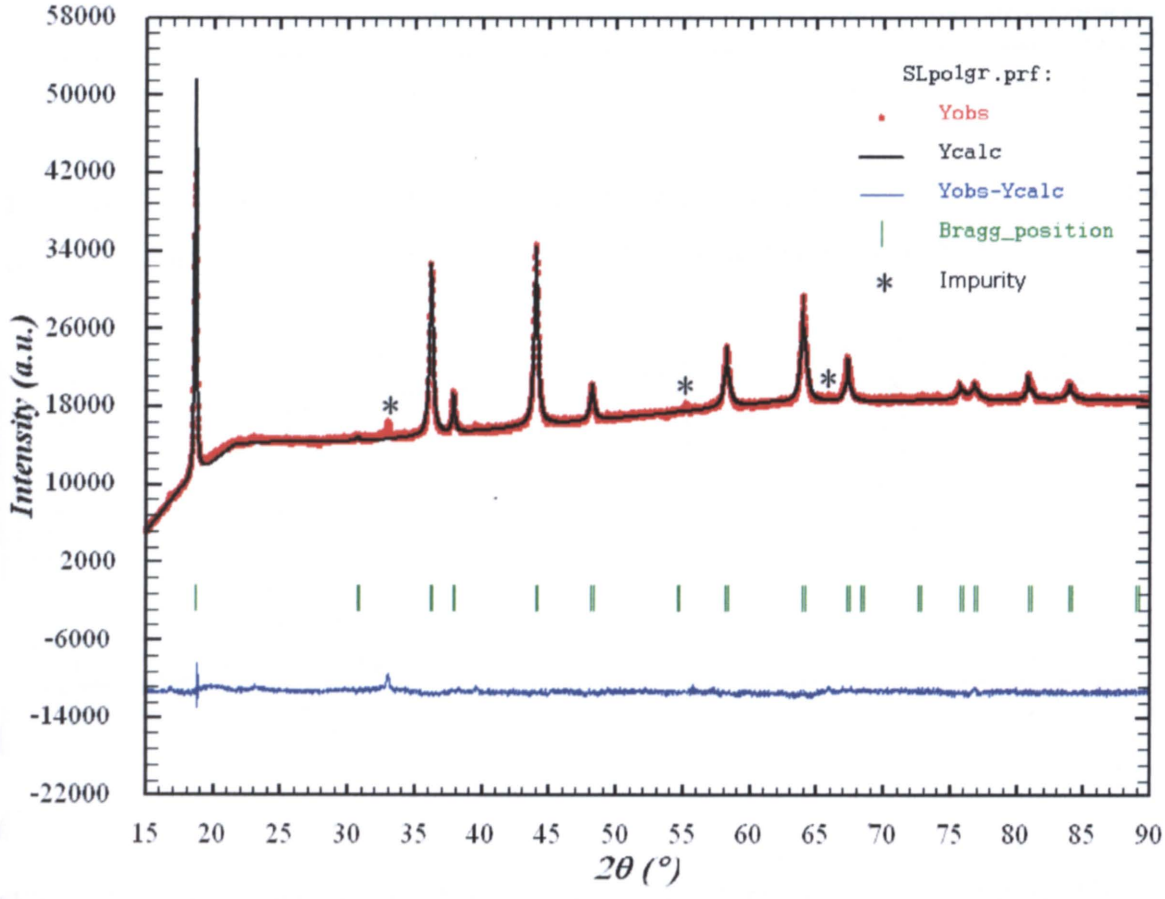

Fig. 7.5. Graphical results of Rietveld refinement for $LiMn_2O_4$ (low temperature sol-gel synthesis) additionally heated up to 580°C, sample measured at 25°C.

Sample	t_{treat} [°C]	Cell parameters [Å] of the individual phases	Fract. (%)	Volume [Å^3]	Bragg R-factor	RF factor
$LiMn_2O_4$ Sol-gel heated up to 300°C during synthesis	580	1) $LiMn_2O_4$: $\alpha=\beta=\gamma=90^o$ a=b=c=8.2295(3).	≈99	557.34	3.75	2.11
		2) $Mn_{3\pm x}O_{4\pm y}$	≈1	-	-	-
$Li_{1.005}Mn_{1.995}O_4$ Sol-gel heated up to 300°C during synthesis	580	1) $LiMn_2O_4$: $\alpha=\beta=\gamma=90^o$ a=b=c=8.2369(5).	≈99	558.84	5.74	3.08
		2) $Mn_{2\pm x}O_{3\pm y}$	≤1	-	-	-

Table 7.4. Numerical results of Rietveld refinement for $LiMn_2O_4$ and $Li_{1.005}Mn_{1.995}O_4$ (low temperature sol-gel synthesis), additionally heated up to 580°C; the measurements performed at 25°C.

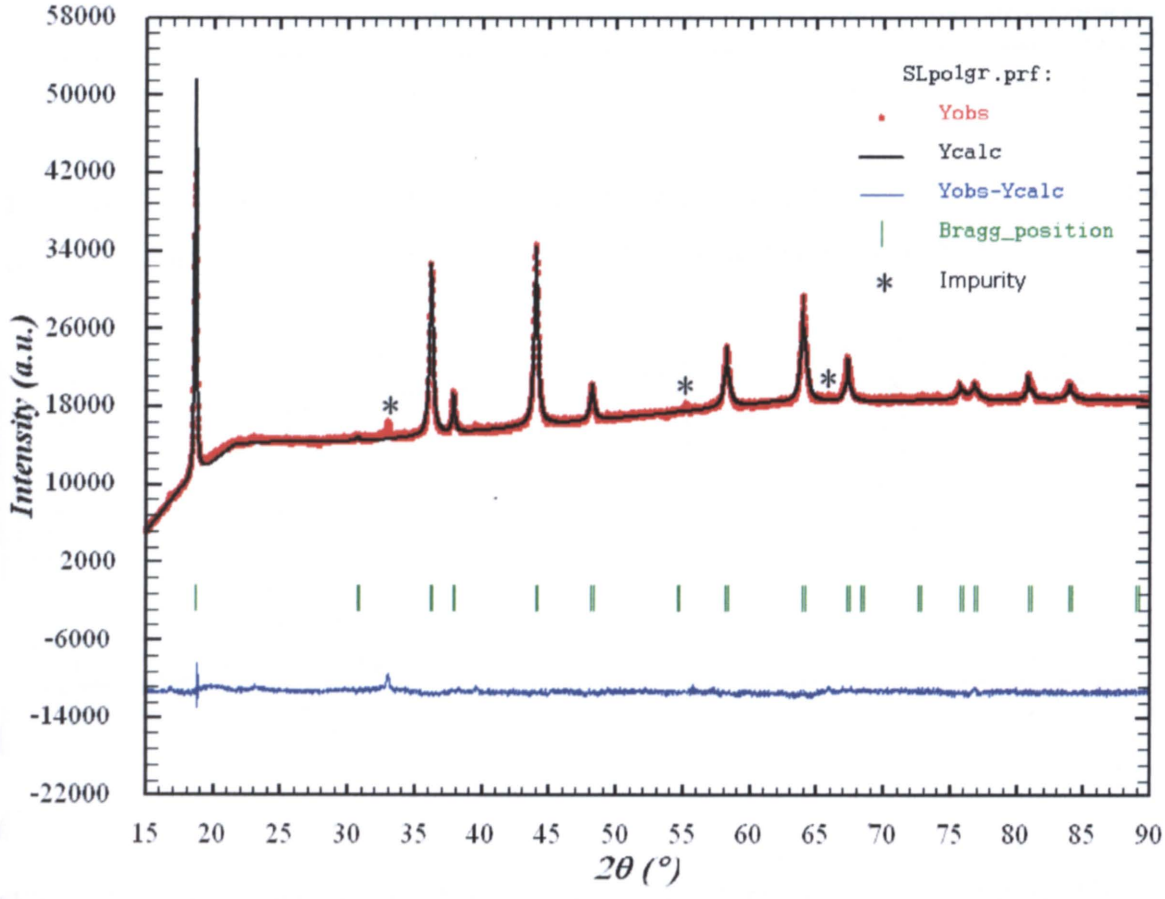

Fig. 7.5. Graphical results of Rietveld refinement for $LiMn_2O_4$ (low temperature sol-gel synthesis) additionally heated up to 580°C, sample measured at 25°C.

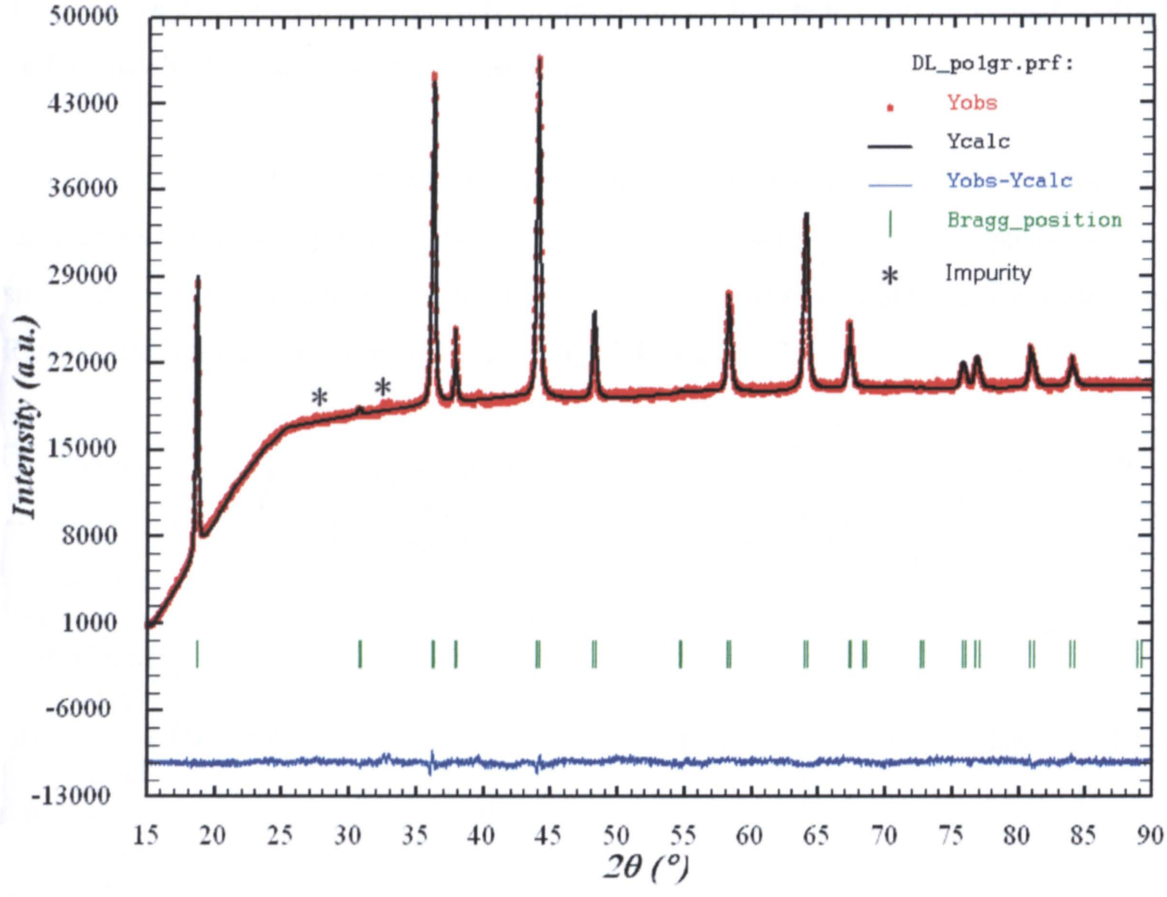

Fig. 7.6. Graphical results of Rietveld refinement for $Li_{1.005}Mn_{1.995}O_4$, (low temperature sol-gel synthesis) additionally heated up to 580°C, sample measured at 25°C.

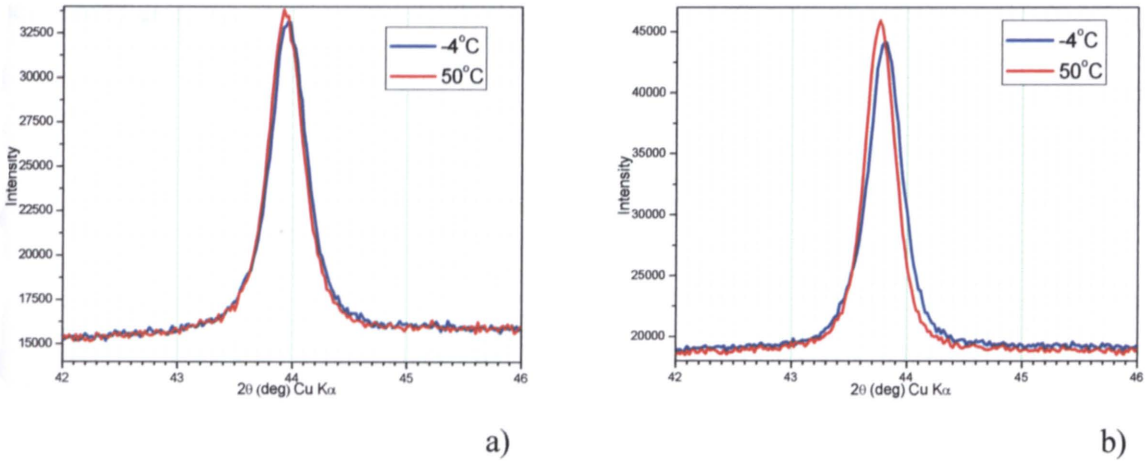

Fig. 7.7. Enlarged parts of XRD patterns (around 400 reflection) measured at 50°C and -4°C for a) $LiMn_2O_4$ and b) $Li_{1.005}Mn_{1.995}O_4$ samples (low temperature sol-gel synthesis) additionally heated up to 580°C.

There is no change of symmetry observed during cooling down to -4°C (Fig.7.7.).

7.1.2. $LiMn_2O_4$ and $Li_{1.005}Mn_{1.995}O_4$ synthesized by low temperature sol-gel method and additionally heat treated up to 800°C

Like previously described samples measured at 25°C without any heat treatment, the samples heated up to 800°C (and measured at 25°C) consist of the same two phases, main - spinel and minor - manganese oxide, but content of the oxide is slightly lower. Results of Rietveld analysis are shown in Table 7.5., Fig. 7.8. and Fig. 7.9.

Sample	t_{treat} [°C]	Cell parameters [Å] of phases	Fract. (%)	Volume [Å^3]	Bragg R-factor	RF factor
$LiMn_2O_4$ Sol-gel heated up to 300°C during synthesis	800	1) $LiMn_2O_4$: $\alpha=\beta=\gamma=90^o$ $a=b=c=8.2500(3)$.	≈99	561.51	4.09	3.61
		2) $Mn_{3\pm x}O_{4\pm y}$	<<1	-	-	-
$Li_{1.005}Mn_{1.995}O_4$ Sol-gel heated up to 300°C during synthesis	800	1) $LiMn_2O_4$: $\alpha=\beta=\gamma=90^o$ $a=b=c=8.2503(2)$.	≈99	561.57	2.61	2.56
		2) $Mn_{2\pm x}O_{3\pm y}$	<<1	-	-	-

Table 7.5. Results of Rietveld refinement for $LiMn_2O_4$ and $Li_{1.005}Mn_{1.995}O_4$ (low temperature sol-gel synthesis) additionally heated up to 800°C; the measurements performed at 25°C.

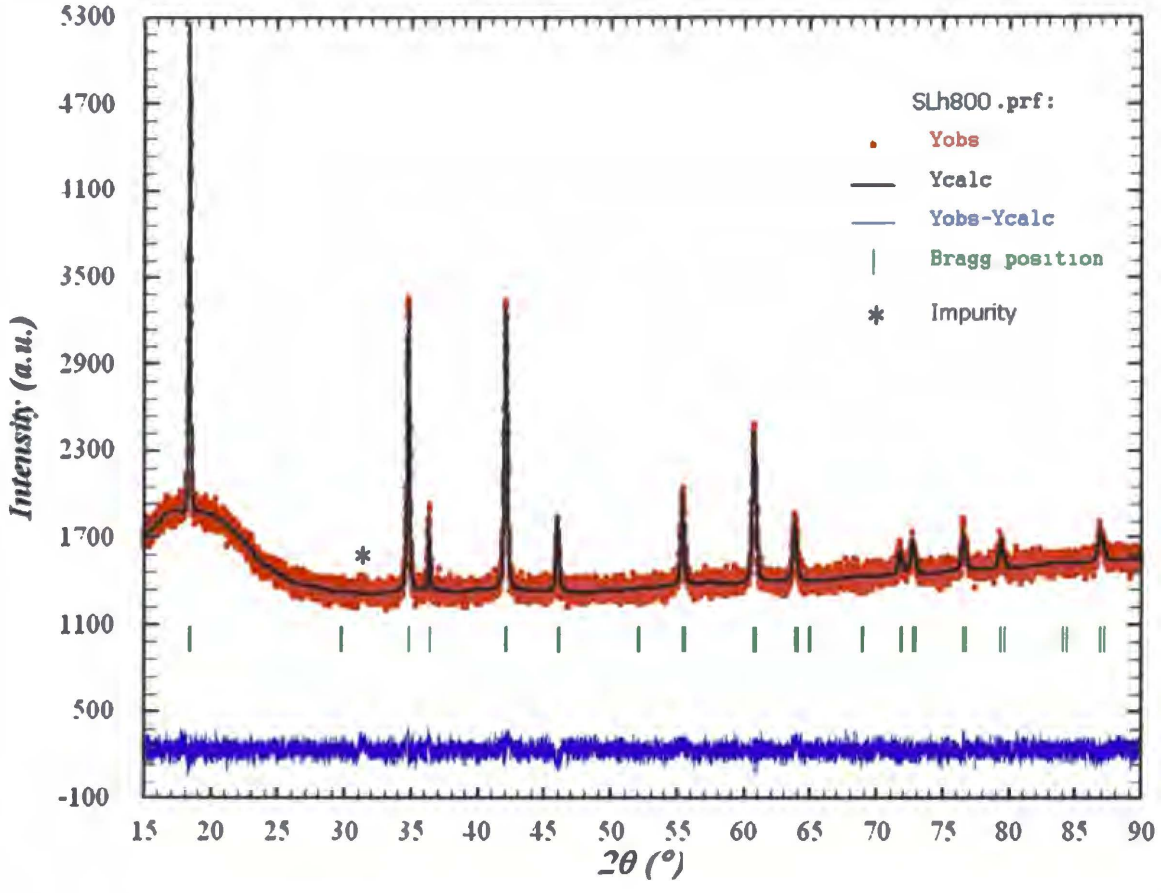

Fig. 7.8. Graphical results of Rietveld refinement for $LiMn_2O_4$ (low temperature sol-gel synthesis) additionally heated up to 800°C, sample measured at 25°C.

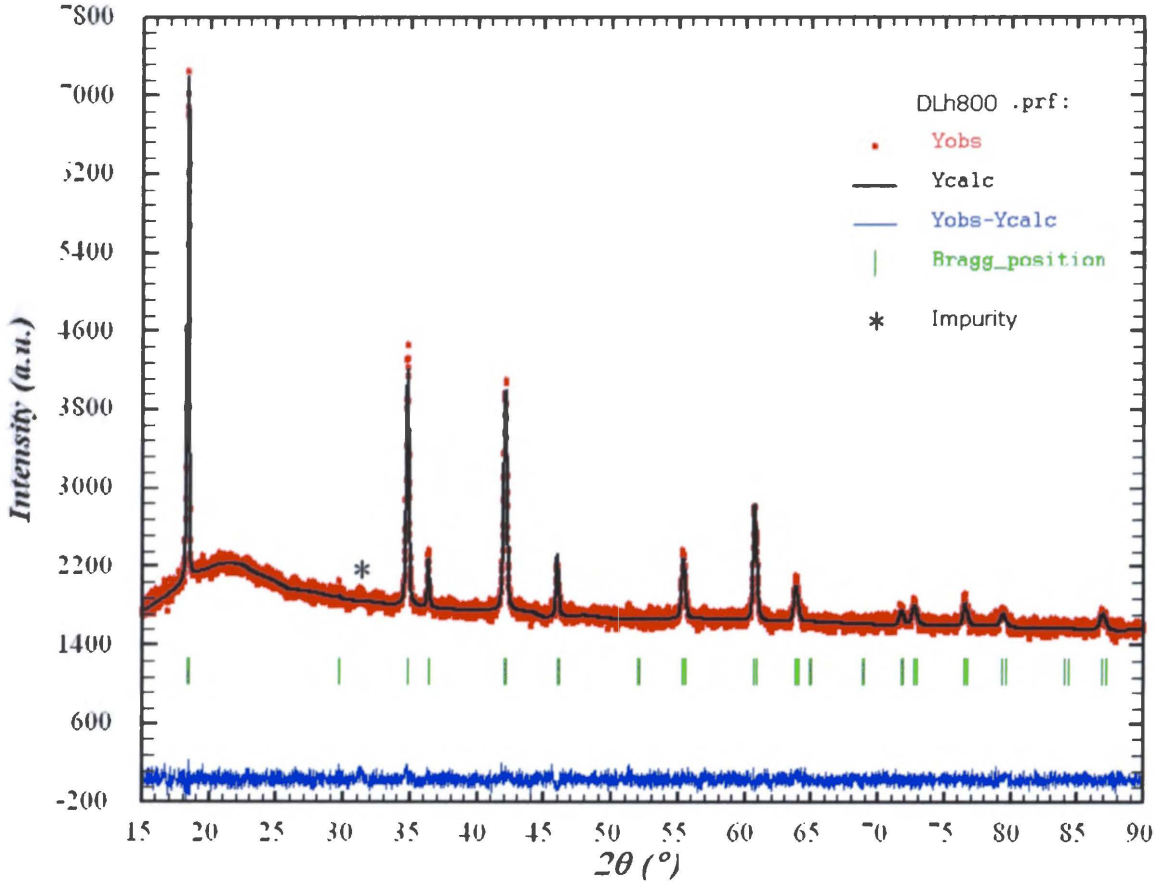

Fig. 7.9. Graphical results of Rietveld refinement for $Li_{1.005}Mn_{1.995}O_4$ (low temperature sol-gel synthesis) additionally heated up to 800°C, sample measured at 25°C.

7.2. $LiMn_2O_4$ synthesized by high temperature sol-gel method

a) XRD measurements

Results of Rietveld analysis are shown in Fig. 7.10., Fig. 7.11. and Table 7.6. At 25°C sample consists of only one phase.

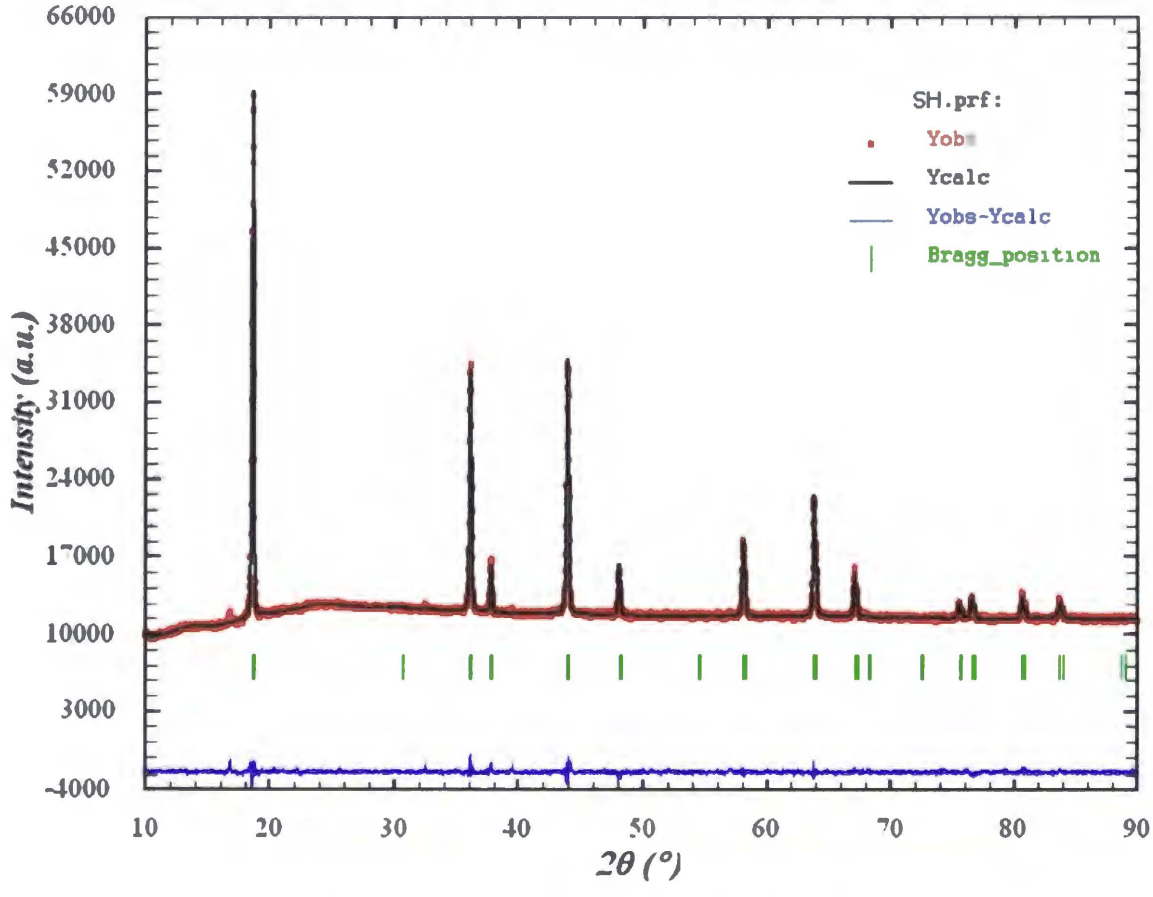

Fig. 7.10. Graphical results of Rietveld refinement for $LiMn_2O_4$ sample (high temperature sol-gel synthesis), sample measured at 25°C.

This is: Lithium Manganese Oxide, (1/2/4), cubic spinel $LiMn_2O_4$, close to ICSD card 40485 and JCPDS card 35-0782, Number of Space group: 227, Hermann-Mauguin Symbol: Fd-3m, Crystal System: Cubic, Laue Class: m-3m, Point Group: m-3m, Bravais Lattice: F, Lattice Symbol: cF.

As can see from offset in Fig. 7.11. and Fig. 7.12. the phase transition is complete already at -4°C.

Sample	t_{meas} [°C]	Cell parameters [Å] of the individual phases	Fract. (%)	Volume [Å^3]	Bragg R-factor	RF factor
$LiMn_2O_4$ Sol-gel heated up to 800°C during synthesis	25	$LiMn_2O_4$: α=β=γ=90° a=b=c=8.2475(2).	100	561.00	2.89	2.31
$LiMn_2O_4$ Sol-gel heated up to 800°C during synthesis	-4	$LiMn_2O_4$: α=β=γ=90° a=8.2075(2) b=8.2537(2) c=8.2860(2).	100	561.31	5.08	3.84

Table 7.6. Numerical results of Rietveld refinement for $LiMn_2O_4$ samples (high temperature sol-gel synthesis).

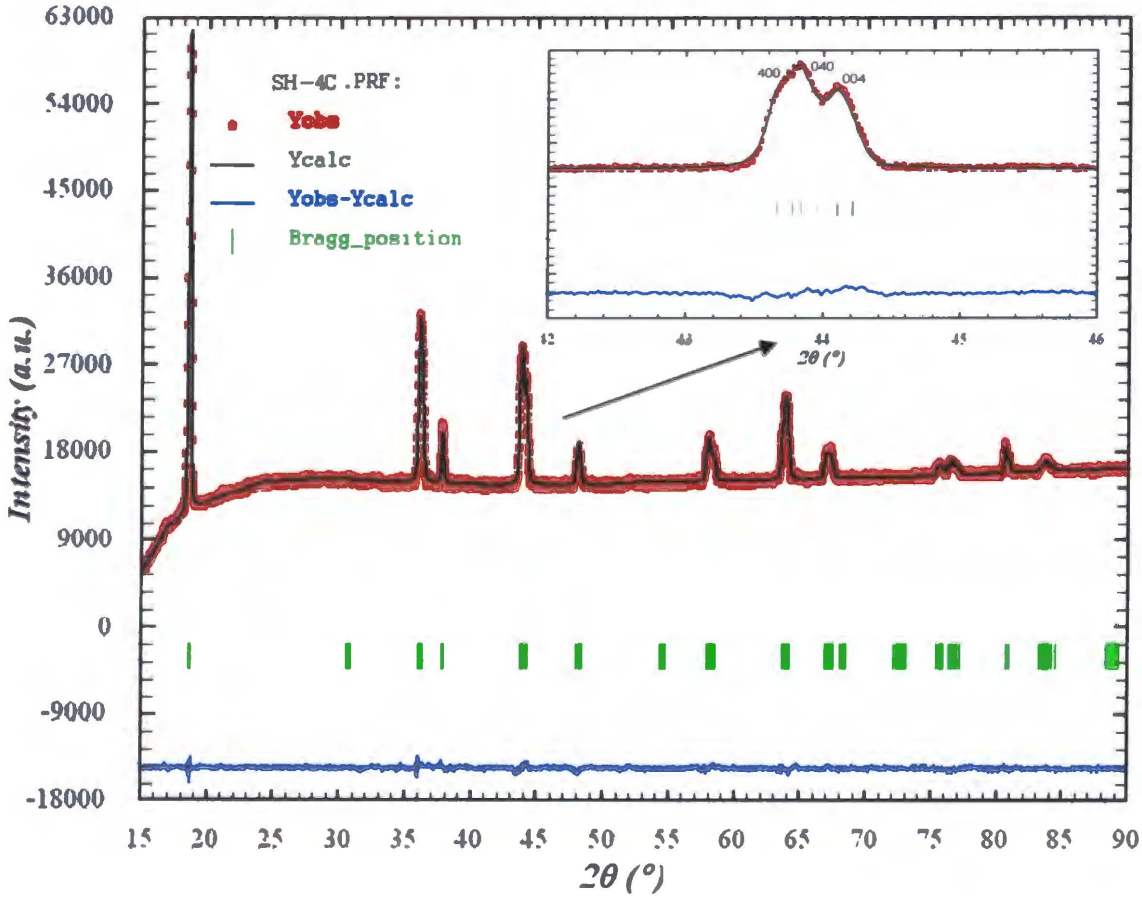

Fig. 7.11. Graphical results of Rietveld refinement for $LiMn_2O_4$ sample (high temperature sol-gel synthesis), sample measured at -4°C.

At -4°C (after phase transition) the sample consist of following spinel phase: Lithium Manganese Oxide (1/2/4), orthorhombic spinel, $LiMn_2O_4$, close to card ICSD #84842, Number of Space group: 70, Hermann-Mauguin Symbol: Fddd, Crystal System: Orthorhombic, Laue Class: mmm, Point Group: mmm, Bravais Lattice: F Lattice Symbol: oF.

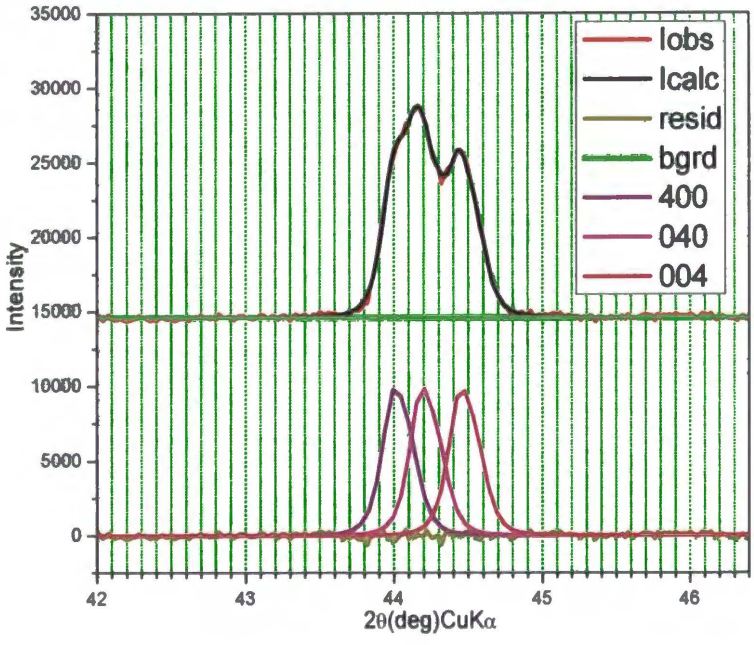

Fig. 7.12. Single peak refinement for $LiMn_2O_4$ sample (high temperature sol-gel synthesis), sample measured at -4°C.

b) Simultaneous XRD and impedance spectroscopy measurements

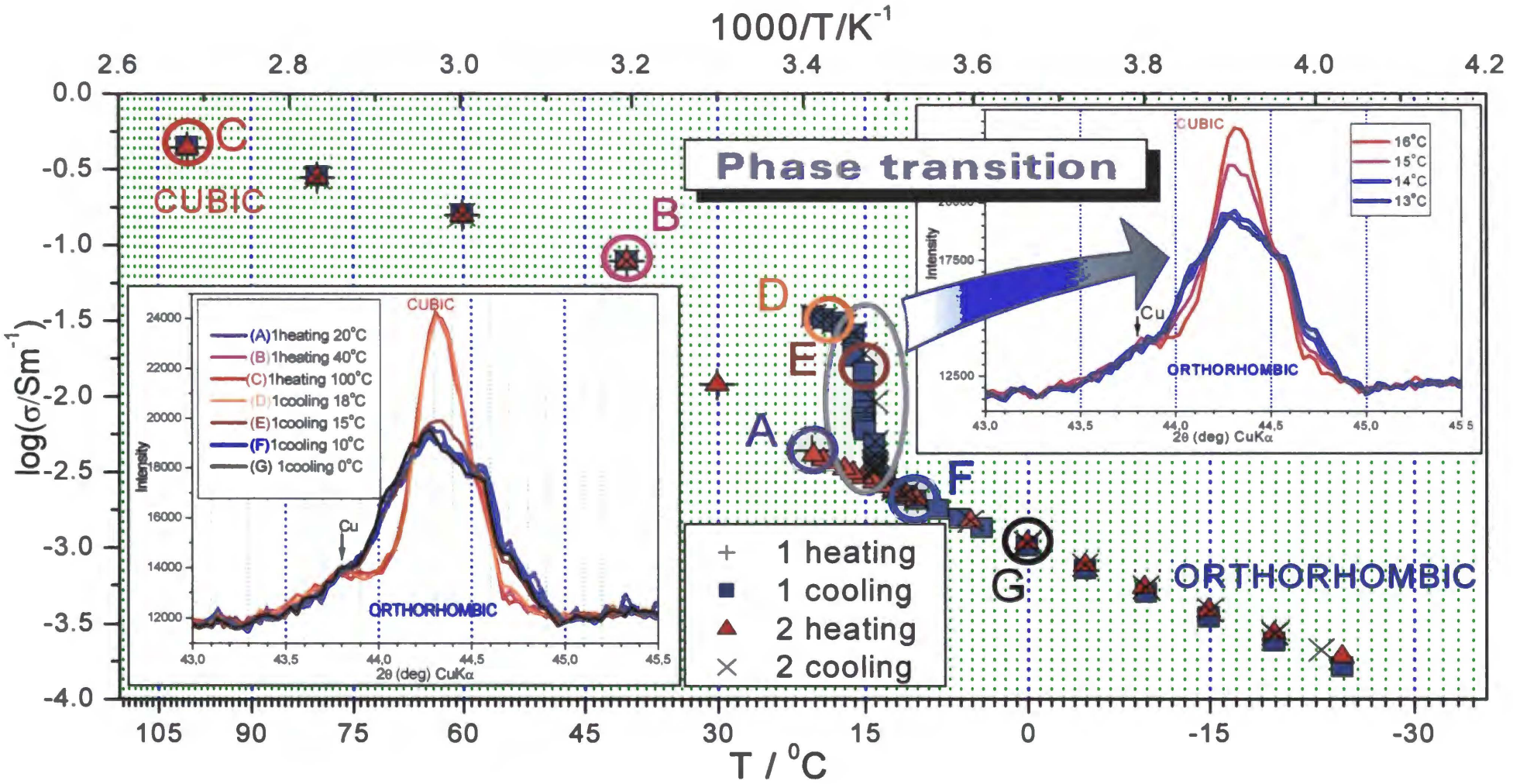

Fig. 7.13. Temperature dependency of conductivity correlated with 400 peak shape for $LiMn_2O_4$ sample (high temperature sol-gel synthesis).

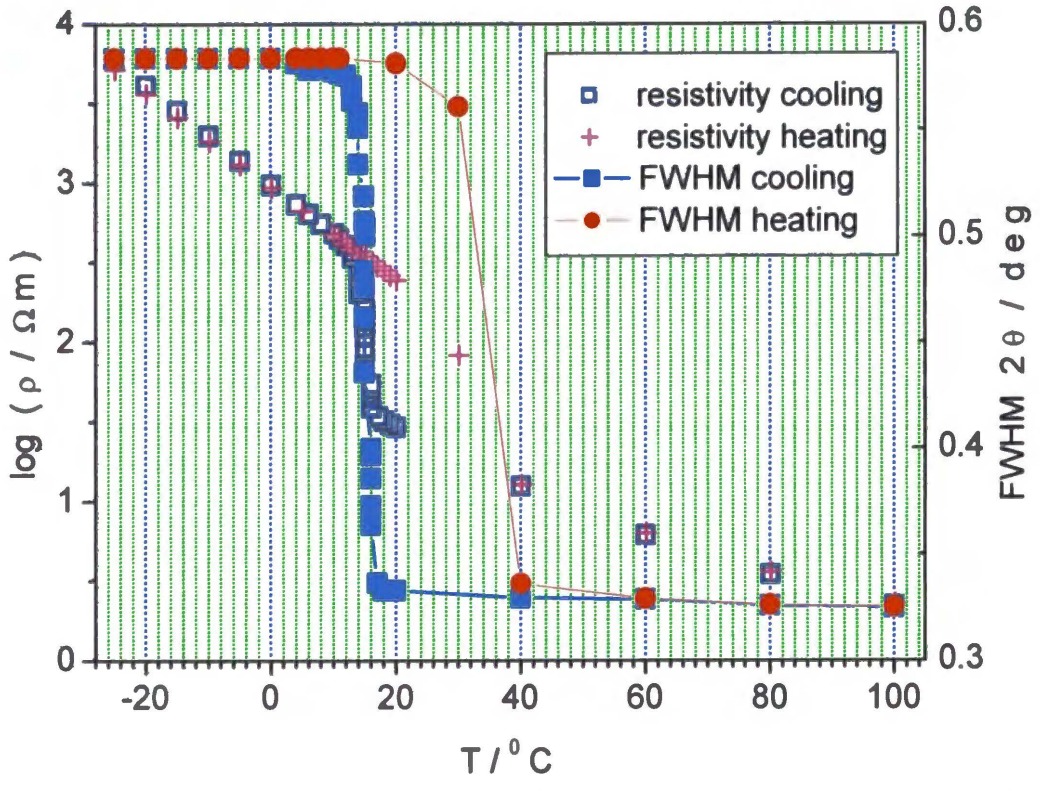

Fig. 7.14. Temperature dependence of FWHM of triplet 400,040,004 fitted like one peak correlated with resistivity for $LiMn_2O_4$ sample (high temperature sol-gel synthesis).

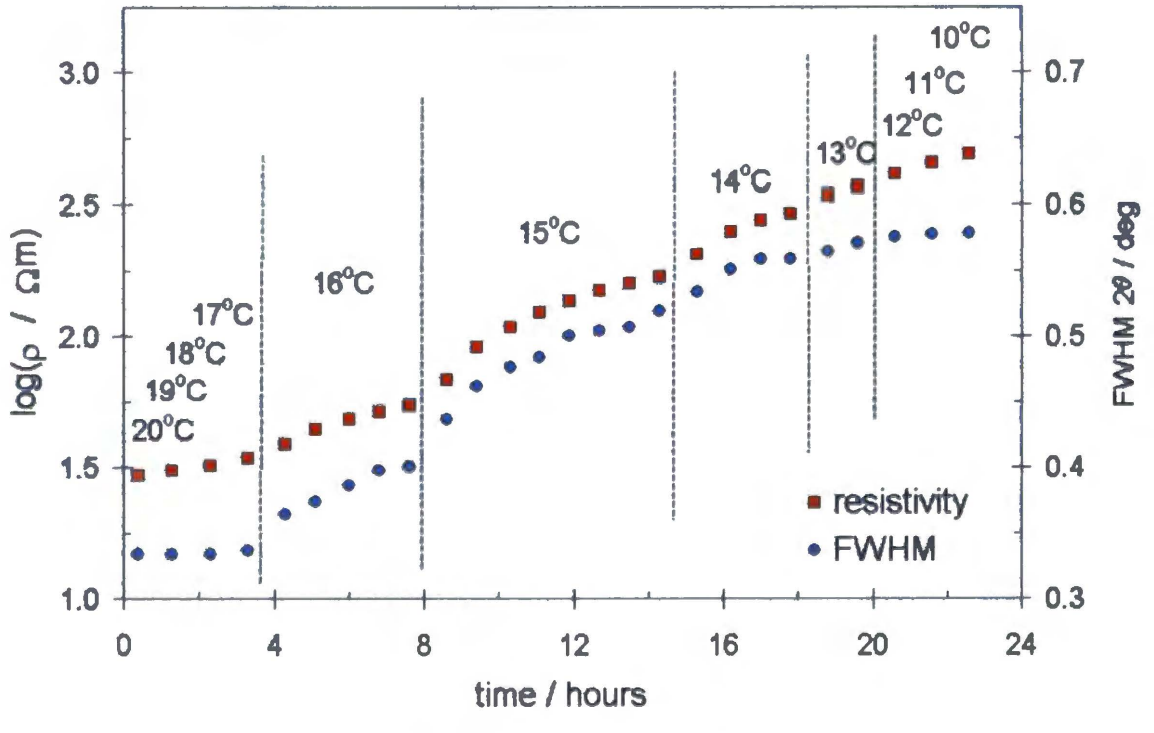

Fig. 7.15. Time dependence of the resistivity (red squares) of $LiMn_2O_4$ (high temperature sol-gel synthesis) and the FWHM (full width at half maximum) of the 400 X-ray reflection (blue circles) during cooling through the temperature region of phase transition.

'.3. $Li_{1.005}Mn_{1.995}O_4$ synthesized by high temperature sol-gel method

a) XRD measurements

Results of Rietveld analysis shown in Fig. 7.16., Fig. 7.17. and Table 7.7. At 25°C sample consists of only one phase.

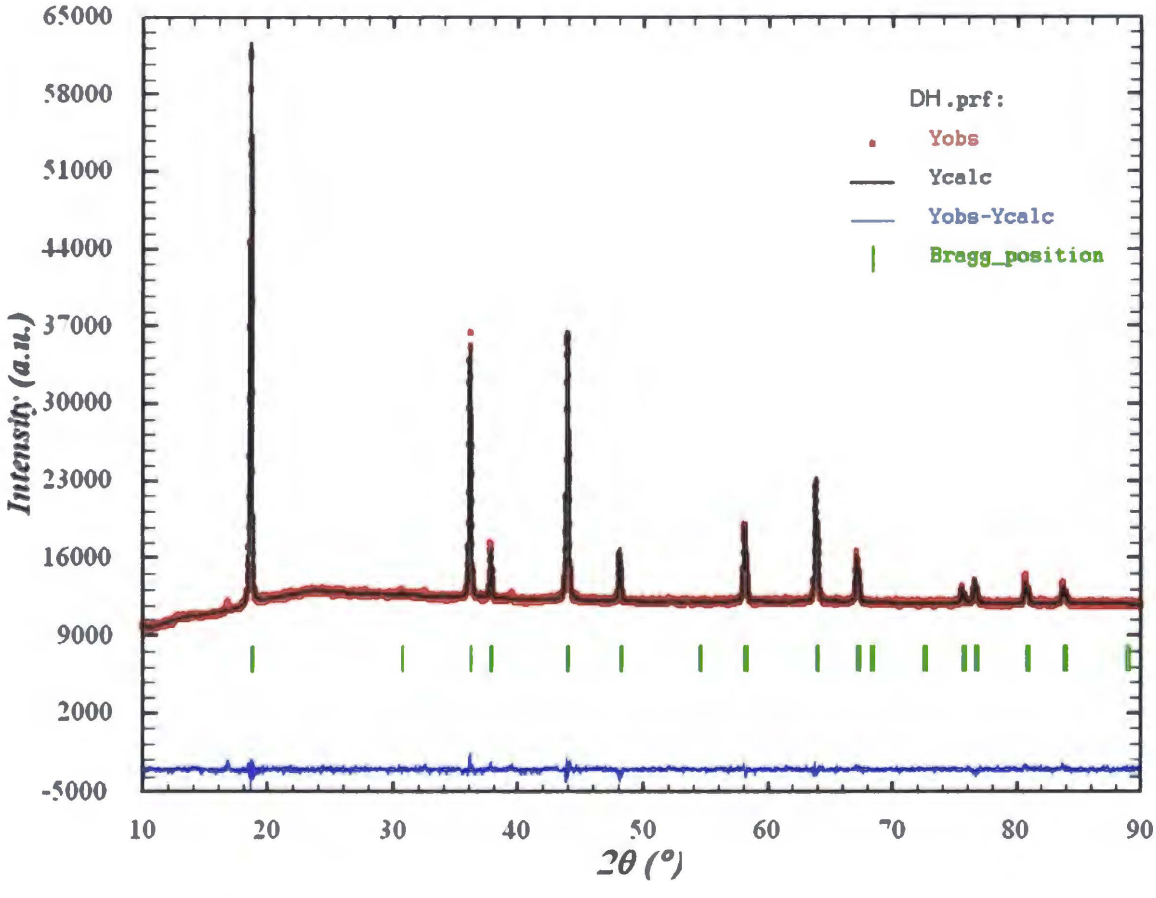

Fig.7.16. Graphical results of Rietveld refinement for $Li_{1.005}Mn_{1.995}O_4$ samples (high temperature sol-gel synthesis), sample measured at 25°C.

It is: Lithium Manganese Oxide , cubic spinel $Li_{1.005}Mn_{1.995}O_4$, close to ICSD card 40485 and JCPDS card 35-0782, Number of Space group: 227, Hermann-Mauguin Symbol: Fd-3m, Crystal System: Cubic, Laue Class: m-3m, Point Group: m-3m, Bravais Lattice: F, Lattice Symbol: cF.

As can see from offset in Fig. 7.17. and Fig. 7.18. the phase transition is complete already at -4°C.

Sample	t_{meas} [°C]	Cell parameters [Å] of the individual phases	Fract. (%)	Volume [Å^3]	Bragg R-factor	RF factor
$Li_{1.005}Mn_{1.995}O_4$ Sol-gel heated up to 800°C during synthesis	25	δ-spinel α=β=γ=90° a=b=c=8.2448(5)	100	560.45	3.75	2.81
$Li_{1.005}Mn_{1.995}O_4$ Sol-gel heated up to 800°C during synthesis	-4	δ-spinel α=β=γ=90° a=8.2084(3) b=8.2505(3) c=8.2849(3).	100	561.08	5.31	4.34

Table 7.7. Results of Rietveld refinement for $Li_{1.005}Mn_{1.995}O_4$ samples (high temperature sol-gel synthesis).

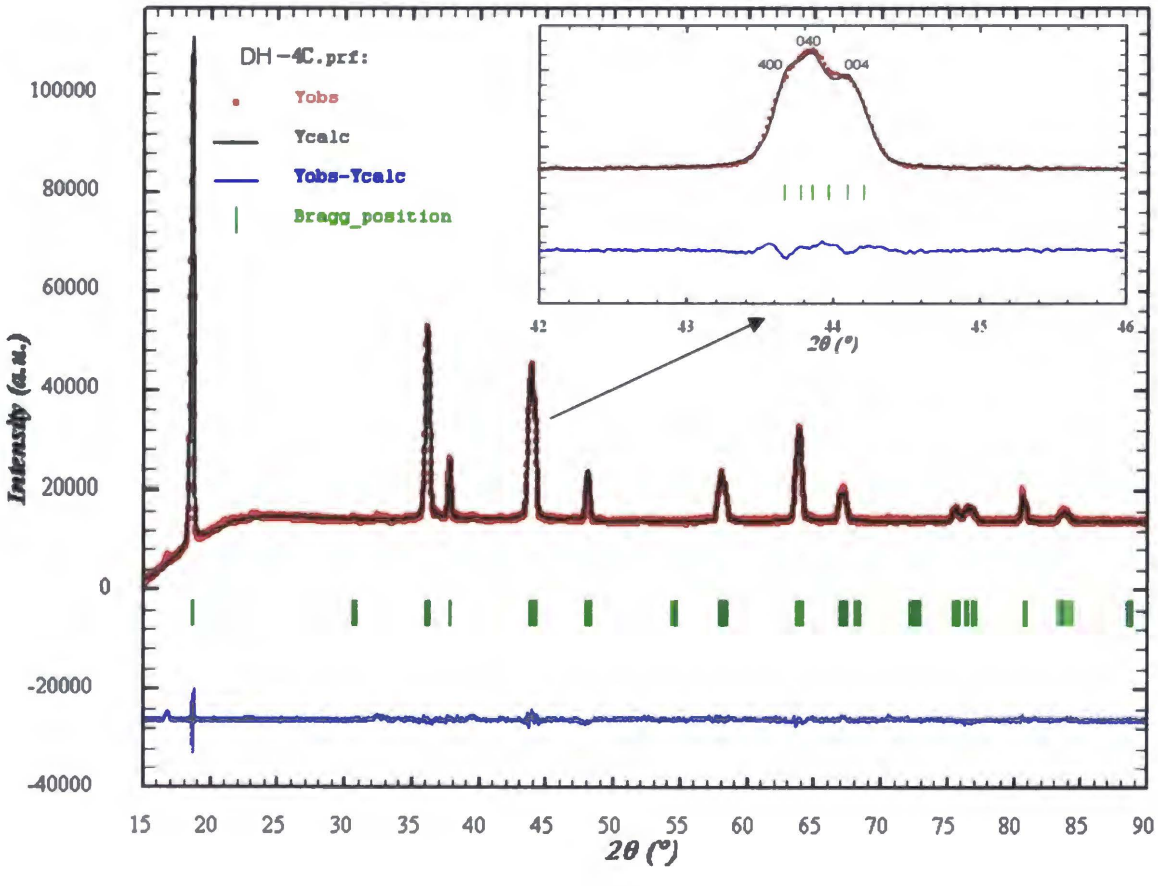

Fig. 7.17. Graphical results of Rietveld refinement for $Li_{1.005}Mn_{1.995}O_4$ samples (high temperature sol-gel synthesis), sample measured at -4°C.

At -4°C (after phase transition) the sample consist of following spinel phase:

Lithium Manganese Oxide, orthorhombic spinel, $Li_{1.005}Mn_{1.995}O_4$, close to card ICSD #84842, Number of Space group: 70, Hermann-Mauguin Symbol: Fddd, Crystal System: Orthorhombic, Laue Class: mmm, Point Group: mmm, Bravais Lattice: F Lattice Symbol: oF.

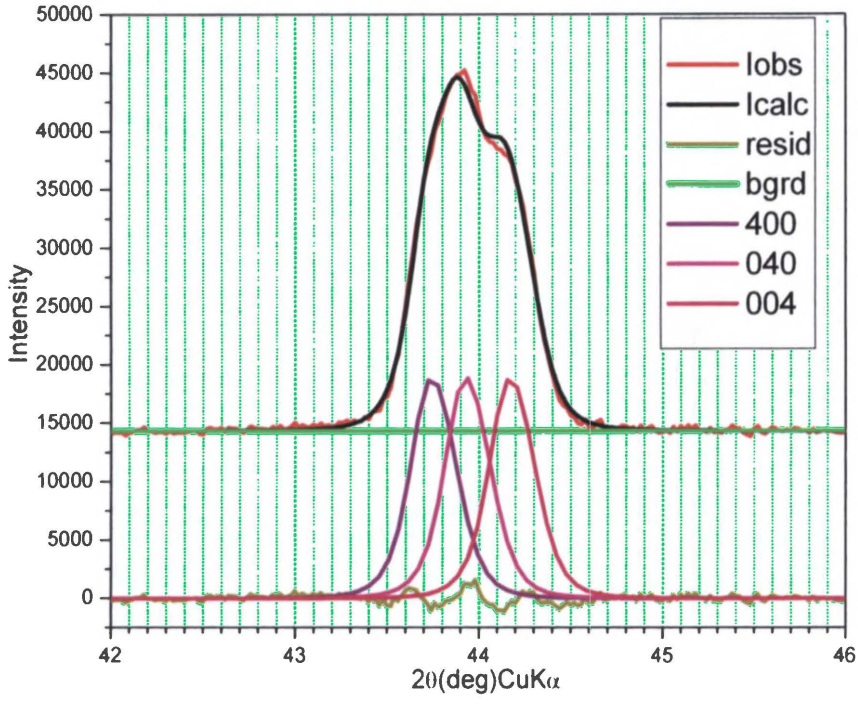

Fig. 7.18. Single peak refinement for $Li_{1.005}Mn_{1.995}O_4$ samples (high temperature sol-gel synthesis), sample measured at -4°C.

b) Simultaneous XRD and impedance spectroscopy measurements

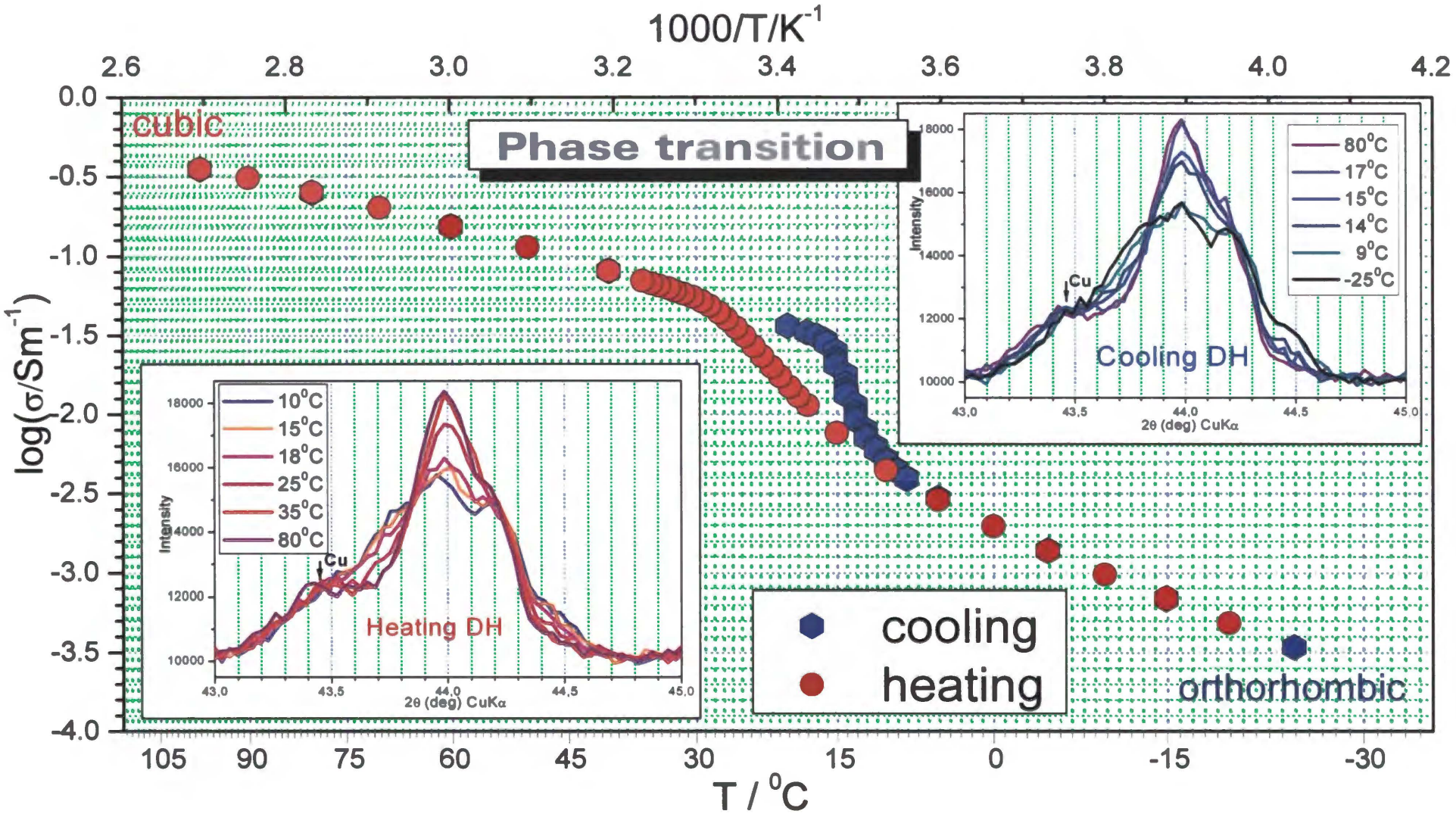

Fig.7.19.Temperature dependency of conductivity correlated with 400 peak shape for $Li_{1.005}Mn_{1.995}O_4$ sample (high temperature sol-gel synthesis)

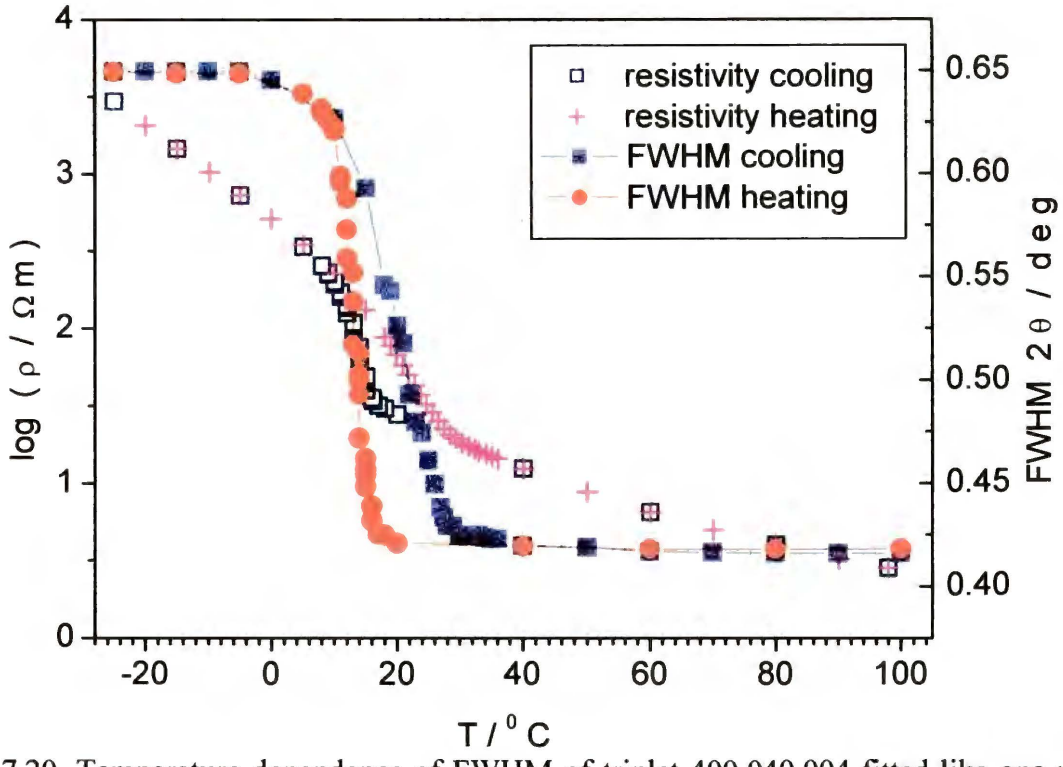

Fig. 7.20. Temperature dependence of FWHM of triplet 400,040,004 fitted like one peak correlated with resistivity for $Li_{1.005}Mn_{1.995}O_4$ sample (high temperature sol-gel synthesis).

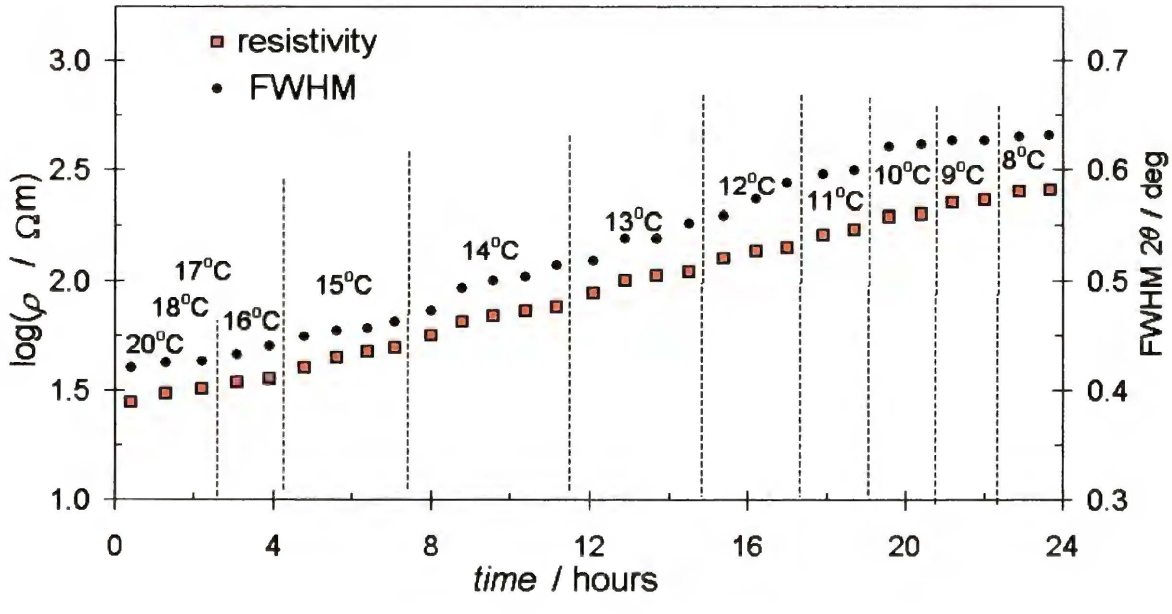

Fig. 7.21. Time dependence of the resistivity (red squares) of $Li_{1.005}Mn_{1.995}O_4$ (high temperature sol-gel synthesis) and the FWHM (full width at half maximum) of the 400 X-ray reflection (blue circles) during cooling through the temperature region of phase transition.

7.4. $LiMn_2O_4$ supplied by Alfa Aesar Company

7.4.1. As supplied.

Specified by manufacturer purity of $LiMn_2O_4$ sample (supplied by Alfa Aesar Co.) is 99.5%. Results of preliminary phase analysis shown presence of manganese oxide Mn_3O_4 close to JCPDS card 80-0382 and ICSD card 068174 (Fig. 7.22.).

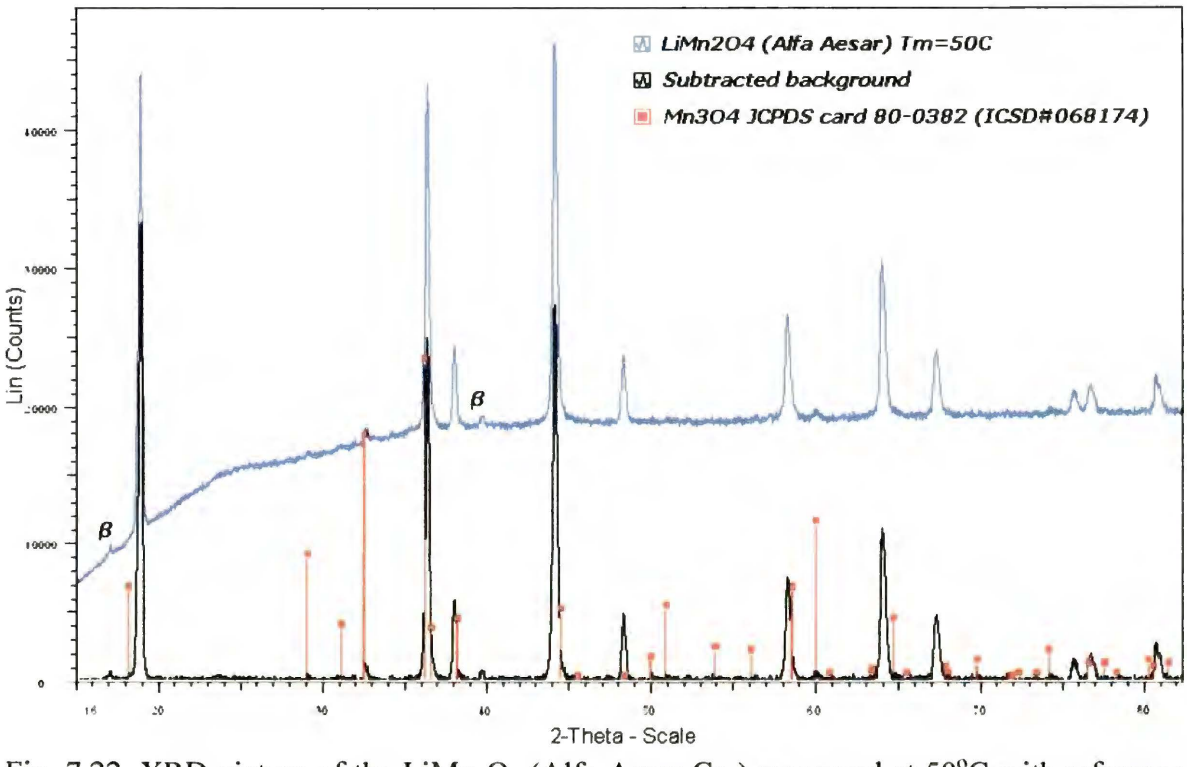

Fig. 7.22. XRD picture of the $LiMn_2O_4$ (Alfa Aesar Co.) measured at 50°C with reference lines of the Mn_3O_4 phase.

The Rietveld analysis has shown presence of Mn_3O_4 impurity of about 3.13 %. The results of Rietveld refinement are presented in Table 7.8., Fig 7.23. and Fig. 7.24.

At 50°C the sample consist of following two phases:

Phase 1: Lithium Manganese Oxide (1/2/4), cubic spinel $LiMn_2O_4$, similar to ICSD card 40485 and JCPDS card 35-0782, Number of Space group: 227, Hermann-Mauguin Symbol: Fd-3m, Crystal System: Cubic, Laue Class: m-3m, Point Group: m-3m, Bravais Lattice: F, Lattice Symbol: cF.

Phase 2: Dimanganese (III) Manganese Oxide, Mn_3O_4, Hausmannite, close to ICSD card 68174 and JCPDS card 80-0382, Number of Space group: 141, Hermann-Mauguin Symbol: I 41/A M D, Crystal System: Tetragonal, Laue Class: 4/mmm, Point Group: 4/mmm Bravais Lattice: I, Lattice Symbol: tI.

At -25°C (after phase transition of the main phase) the sample consists of the following two phases:

Phase 1: Lithium Manganese Oxide (1/2/4), orthorhombic spinel, $LiMn_2O_4$, close to card ICSD #84842, Number of Space group: 70, Hermann-Mauguin Symbol: Fddd, Crystal System: Orthorhombic, Laue Class: mmm, Point Group: mmm, Bravais Lattice: F Lattice Symbol: oF.

Phase 2: Dimanganese (III) Manganese Oxide Mn_3O_4 Hausmannite close to ICSD card 68174 and JCPDS card 80-0382, Number of Space group: 141, Hermann-Mauguin Symbol: I 41/A M D, Crystal System: Tetragonal, Laue Class: 4/mmm, Point Group: 4/mmm Bravais Lattice: I, Lattice Symbol: tI. (Cell parameters were adopted from refinement for +50°C, assuming that this oxide does not change its structure in the temperature range from -25°C to 50°C).

Sample	t_{meas} [°C]	Cell parameters [Å] of the individual phases	Fract. (%)	Volume [Å^3]	Bragg R-factor	RF factor
$LiMn_2O_4$ Alfa Aesar as supplied	50	1) $LiMn_2O_4$: $\alpha=\beta=\gamma=90^o$ a=b=c=8.2408(6).	1) 96.87 ±1.03	559.63	15.4	8.90
		2) Mn_3O_4 : $\alpha=\beta=\gamma=90^o$, a=5.7651(8), b=5.7651(8), c=9.4422 (8)	2) 3.13 ±0.22	313.82	35.2	31.3
$LiMn_2O_4$ Alfa Aesar as supplied	-25	1) $LiMn_2O_4$: $\alpha=\beta=\gamma=90^o$ a=8.2052(9), b=8.2417(9), c=8.2778(9)	1) 96.87 ±1.03	559.78	13.6	10.4
		2) Mn_3O_4 : $\alpha=\beta=\gamma=90^o$, a=5.7651(8), b=5.7651(8), c=9.4422 (8)	2) 3.13 ±0.22	313.82	45.5	35.8

Table 7.8. Numerical results of Rietveld refinement for $LiMn_2O_4$ (Alfa Aesar Co.) samples as supplied.

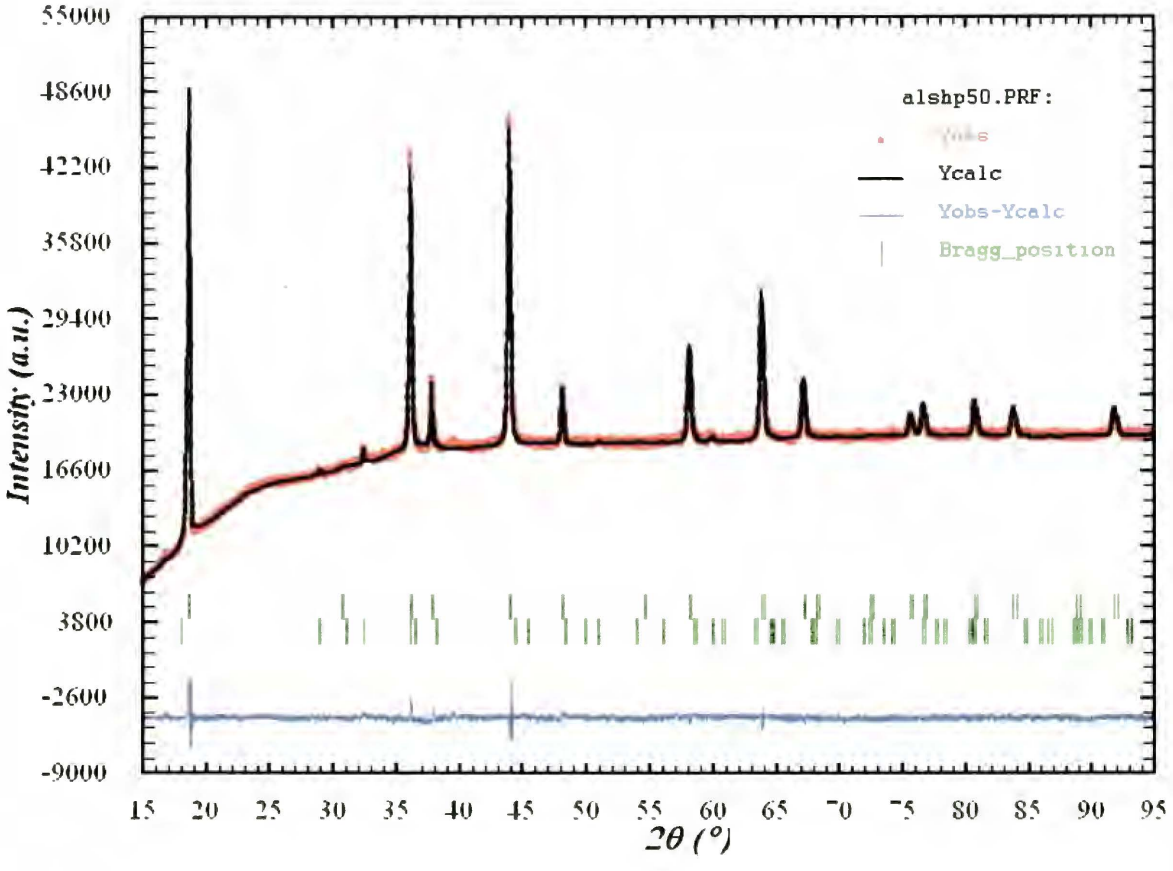

Fig. 7.23. Graphical results of Rietveld refinement for $LiMn_2O_4$ (Alfa Aesar Co.) sample as supplied (measured at 50°C).

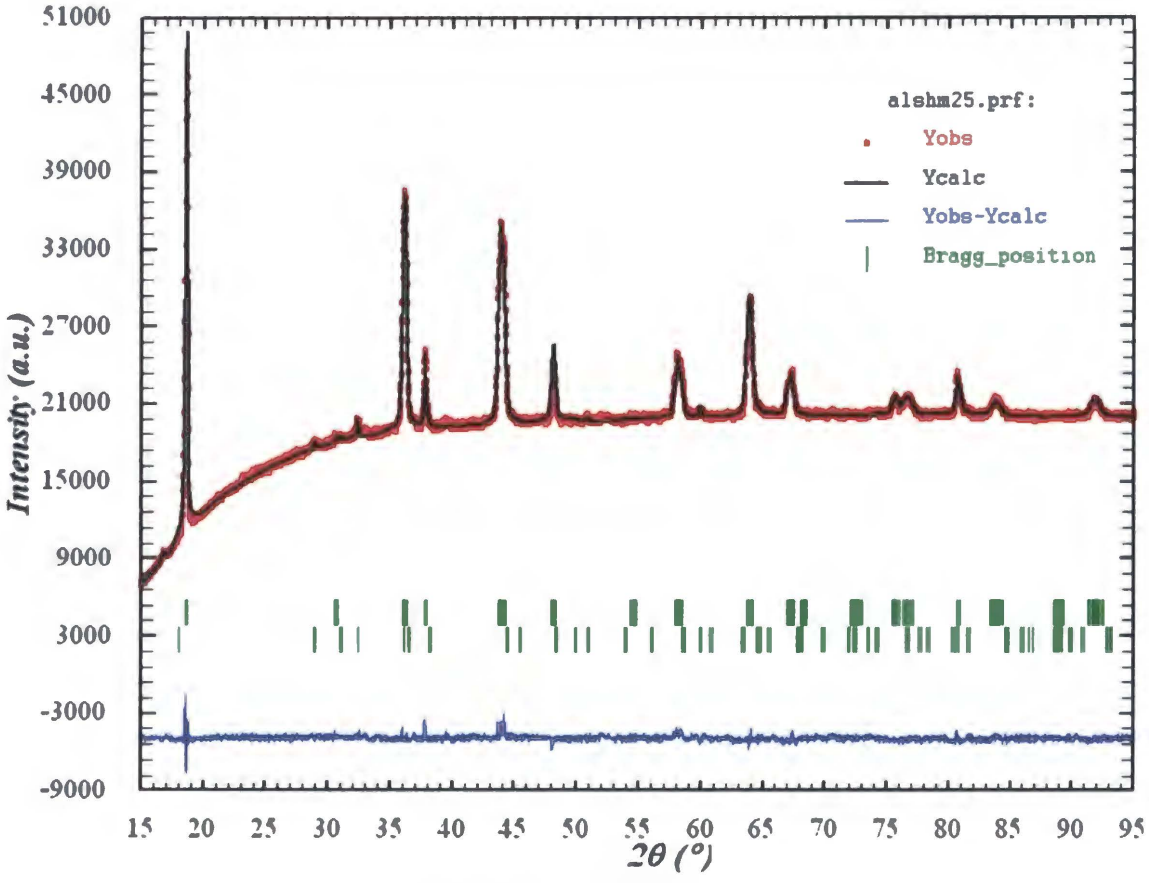

Fig. 7.24. Graphical results of Rietveld refinement for $LiMn_2O_4$ (Alfa Aesar Co.) sample as supplied (measured at -25°C).

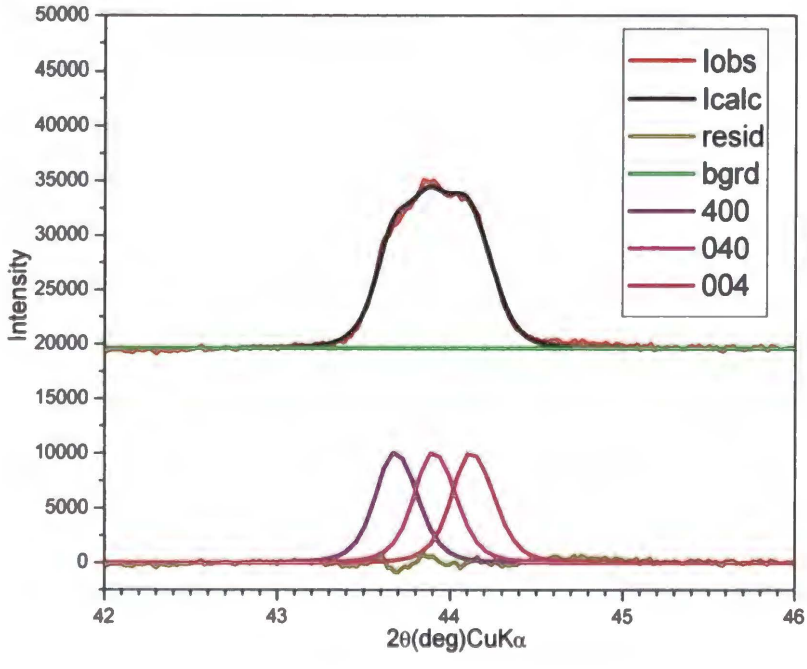

Fig. 7.25. Single peak refinement for $LiMn_2O_4$ (Alfa Aesar Co.) sample us supplied (measured at -25°C).

7.4.2. Heated up to 800°C

a) XRD measurements

After heat treatment at 800°C the quantity of impurity phase was diminished down to 1.1% as follow from Rietveld refinement, results shown in Table 7.9., Fig. 7.26. and Fig.7.27.

Sample	t_{meas} [°C]	Cell parameters [Å] of the individual phases	Fract. (%)	Volume [Å^3]	Bragg R-factor	RF factor
$LiMn_2O_4$ Alfa Aesar heated up to 800°C	50	1) $LiMn_2O_4$: $\alpha=\beta=\gamma=90^o$ $a=b=c=8.2539(6)$.	1) 98.99 ±0.60	562.31	9.05	7.94
		2) Mn_3O_4: $\alpha=\beta=\gamma=90^o$, $a=5.7651(8)$, $b=5.7651(8)$, $c=9.4422(8)$	2) 1.01 ±0.05	313.82	60.6	42.1
$LiMn_2O_4$ Alfa Aesar heated up to 800°C	-25	1) $LiMn_2O_4$: $\alpha=\beta=\gamma=90^o$ $a=8.2052(9)$, $b=8.2554(9)$, $c=8.2906(9)$	1) 98.99 ±0.61	561.58	9.62	8.94
		2) Mn_3O_4: $\alpha=\beta=\gamma=90^o$, $a=5.7651(8)$, $b=5.7651(8)$, $c=9.4422(8)$	2) 1.01 ±0.05	313.82	77.6	51.4

Table 7.9. Numerical results of Rietveld refinement for $LiMn_2O_4$ (Alfa Aesar Co.), samples heated up to 800°C.

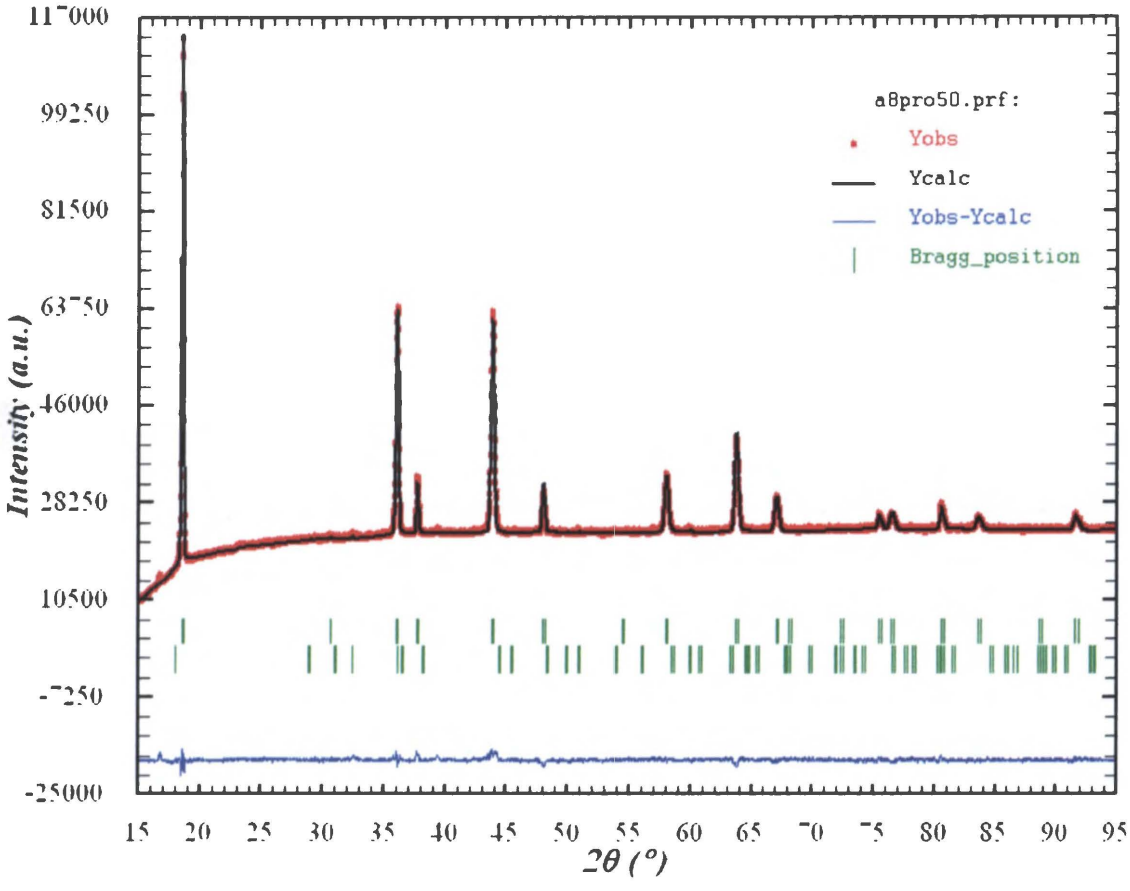

Fig. 7.26. Graphical results of Rietveld refinement for $LiMn_2O_4$ (Alfa Aesar Co.), sample heated up to 800°C (measured at 50°C).

At 50°C the sample consists of the following two phases:

Phase 1: Lithium Manganese Oxide (1/2/4), cubic spinel $LiMn_2O_4$, similar to ICSD card 40485 and JCPDS card 35-0782, Number of Space group: 227, Hermann-Mauguin Symbol: Fd-3m, Crystal System: Cubic, Laue Class: m-3m, Point Group: m-3m, Bravais Lattice: F, Lattice Symbol: cF.

Phase 2: Dimanganese (III) Manganese Oxide, Mn_3O_4, Hausmannite, close to ICSD card 68174 and JCPDS card 80-0382, Number of Space group: 141, Hermann-Mauguin Symbol: I 41/A M D, Crystal System: Tetragonal, Laue Class: 4/mmm, Point Group: 4/mmm Bravais Lattice: I, Lattice Symbol: tI.

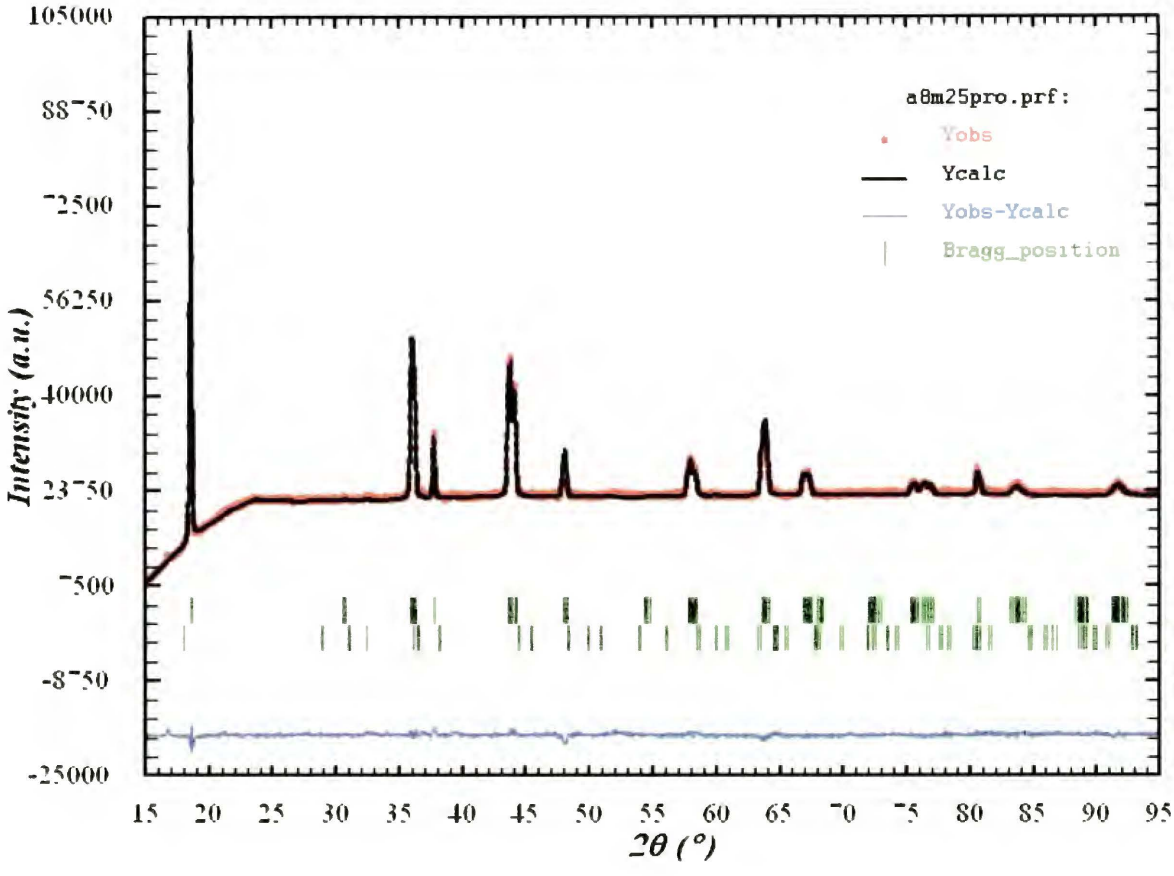

Fig. 7.27. Graphical results of Rietveld refinement for $LiMn_2O_4$ (Alfa Aesar Co.), sample heated up to 800°C (measured at -25°C).

At -25°C (after phase transition of the main phase) the sample consists of the following two phases:

Phase 1: Lithium Manganese Oxide (1/2/4), orthorhombic spinel, $LiMn_2O_4$, close to card ICSD #84842, Number of Space group: 70, Hermann-Mauguin Symbol: Fddd, Crystal System: Orthorhombic, Laue Class: mmm, Point Group: mmm, Bravais Lattice: F Lattice Symbol: oF.

Phase 2: Dimanganese (III) Manganese Oxide Mn_3O_4 Hausmannite close to ICSD card 68174 and JCPDS card 80-0382, Number of Space group: 141, Hermann-Mauguin Symbol: I 41/A M D, Crystal System: Tetragonal, Laue Class: 4/mmm, Point Group: 4/mmm Bravais Lattice: I, Lattice Symbol: tI. (as before the cell parameters were adopted from refinement for +50°C, assuming that this oxide does not change its structure in the temperature range from -25°C to 50°C).

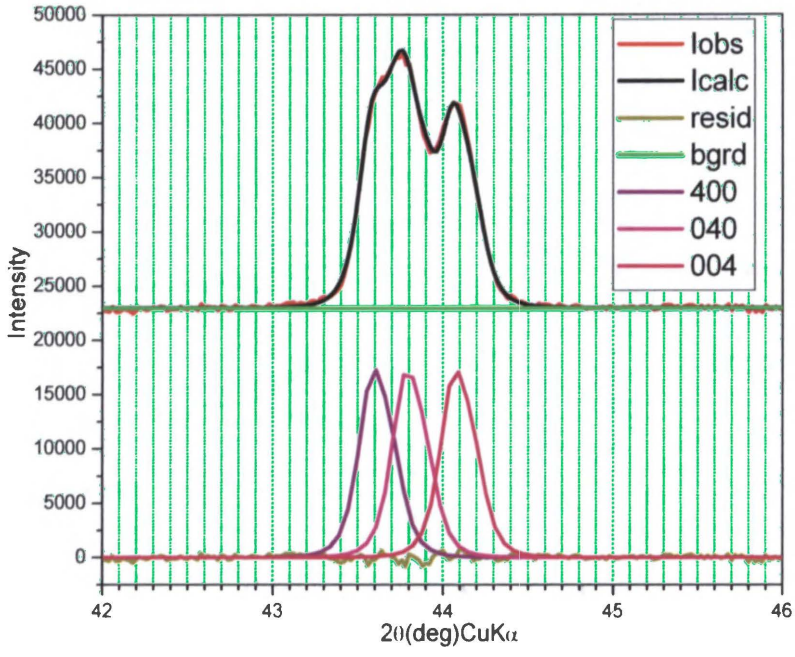

Fig. 7.28. Single peak refinement for $LiMn_2O_4$ (Alfa Aesar Co.), sample heated up to 800°C (measured at -25°C).

b) Simultaneous XRD and impedance spectroscopy measurements

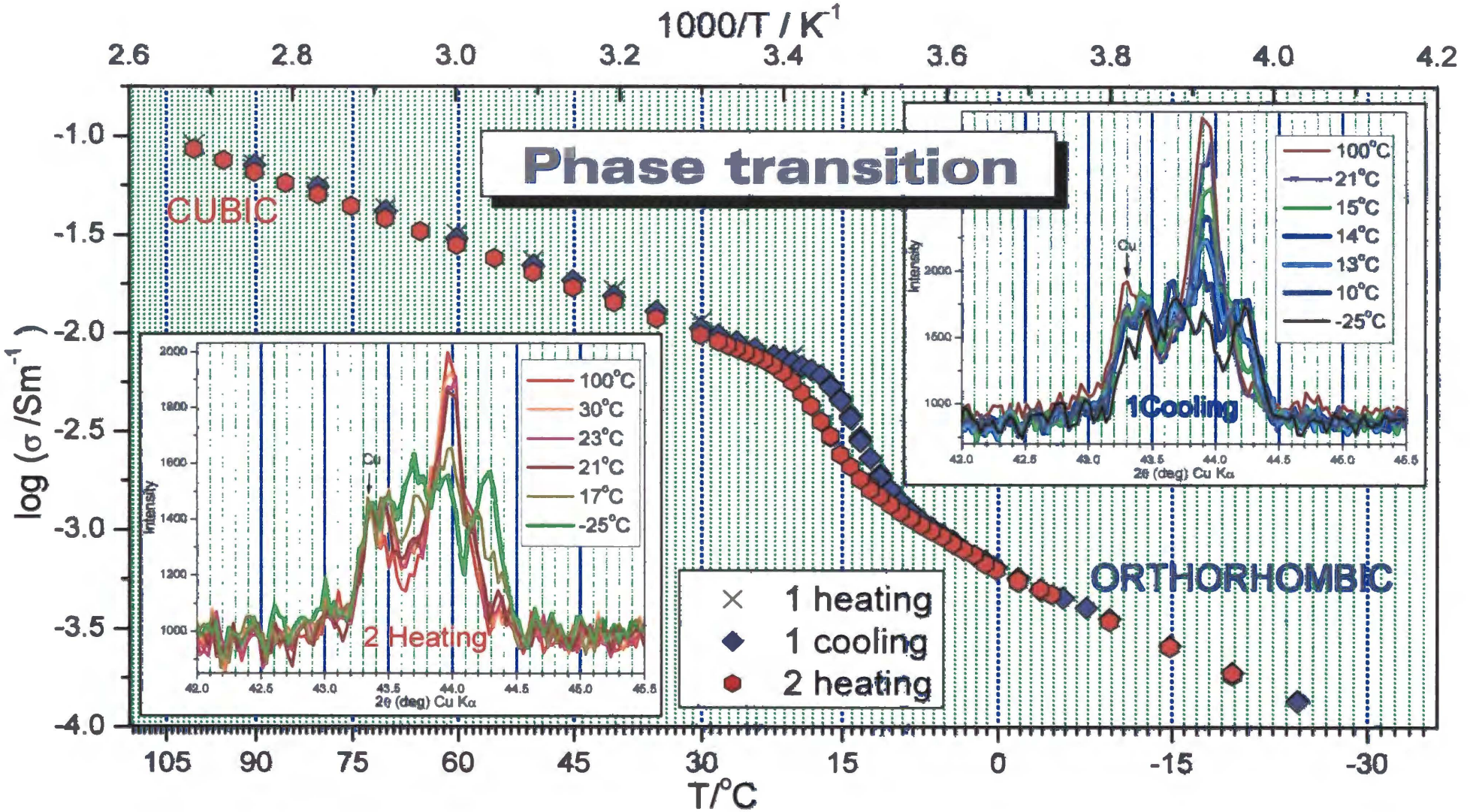

Fig. 7.29. Temperature dependency of conductivity correlated with 400 peak shape for $LiMn_2O_4$ (Alfa Aesar Co.), sample heated up to 800°C.

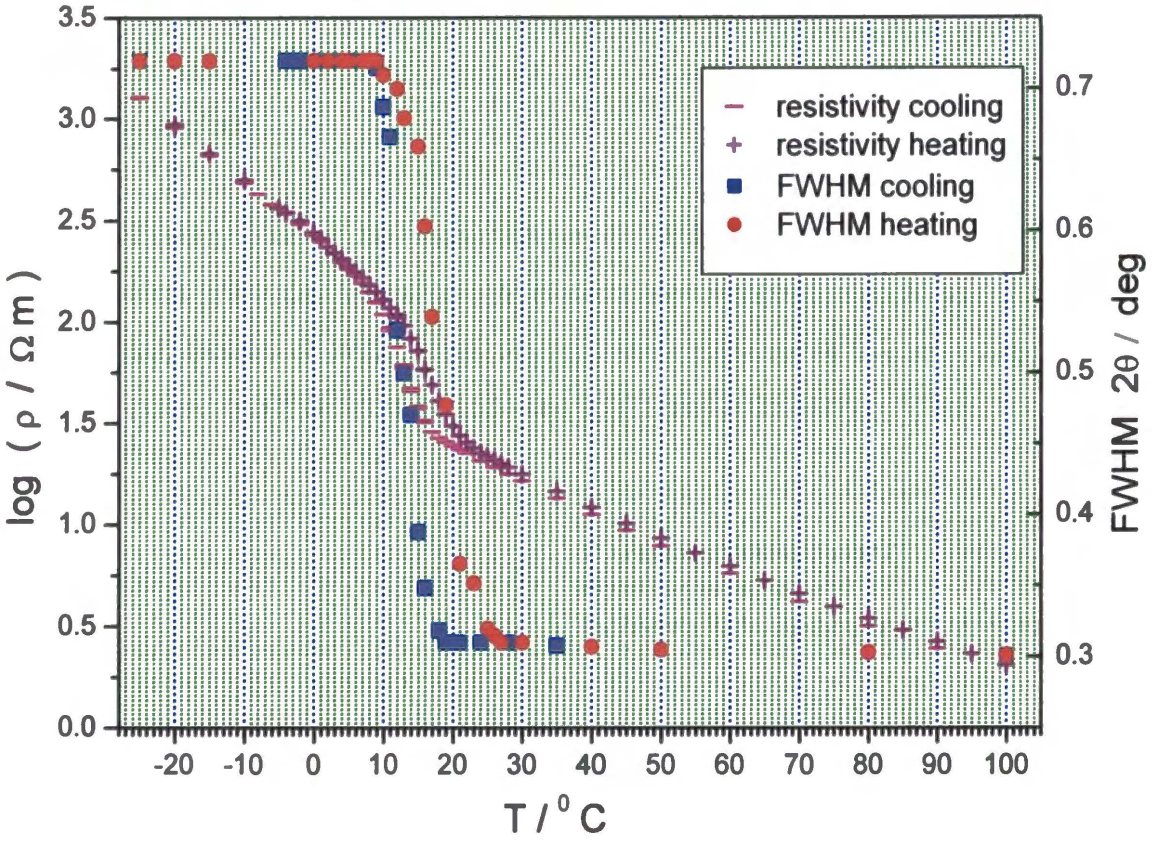

Fig. 7.30. Temperature dependence of FWHM of triplet 400,040,004 fitted like one peak correlated with resistivity for $LiMn_2O_4$ (Alfa Aesar Co.), sample heated up to 800°C.

7.5. $LiMn_2O_4$ supplied by Sigma - Aldrich Company

7.5.1. As supplied.

Specification note of the manufacturer of $LiMn_2O_4$ sample (supplied by Sigma - Aldrich Co.) gives the following information: electrochemical grade and substance not fully tested. Results of initial phase analysis show presence of lithium manganese oxide Li_2MnO_3 close to JCPDS card 84-1634 and ICSD card 202639 (Fig. 7.31.).

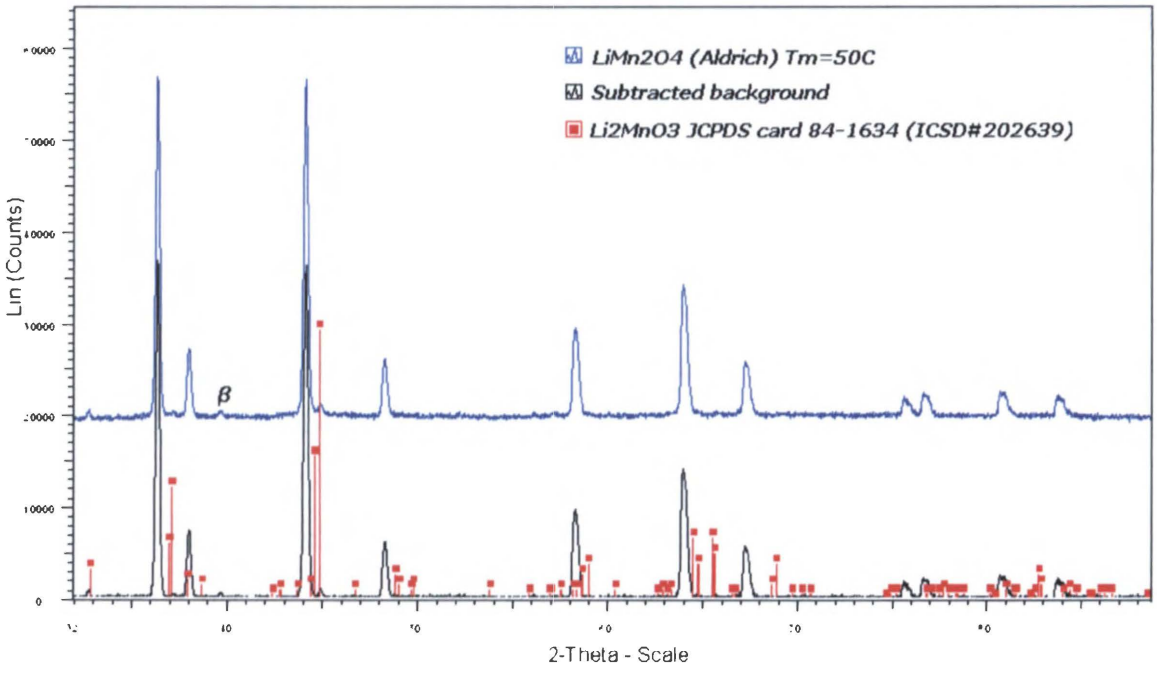

Fig. 7. 31. Enlarged part of XRD pattern of the $LiMn_2O_4$ (Sigma - Aldrich Co.) measured at 50°C with reference lines of the Li_2MnO_3 phase presented as bars.

The Rietveld analysis has shown presence of Li_2MnO_3 impurity of about 4.94 %. The results of Rietveld refinement are given in Table 7.10., Fig. 7.32. and Fig. 7.34.

At 50°C the sample consists of following two phases:

Phase 1: Lithium Manganese Oxide (1/2/4), spinel $LiMn_2O_4$, similar to cards JCPDS 35-0782 and ICSD 40485. Number of Space group: 227, Hermann-Mauguin Symbol: Fd-3m, Crystal System: Cubic, Laue Class: m-3m, Point Group: m-3m, Bravais Lattice: F, Lattice Symbol: cF.

Phase 2: Dilithium Manganese (IV) Trioxide, Li_2MnO_3 close to cards JCPDS 84-1634, ICSD 83848 and ICSD 202639. Number of Space group: 12, Hermann-Mauguin Symbol:

C 1 2/M 1, Crystal System: Monoclinic, Laue Class: 2/m, Point Group: 2/m, Bravais Lattice: C, Lattice Symbol: mC.

At -25°C (after phase transition of main phase) the sample consists of the following three phases:

Phase 1: Lithium Manganese Oxide (1/2/4), *orthorhombic* spinel $LiMn_2O_4$, close to cards JCPDS 88-0544 and ICSD 84842. Number of Space group: 70, Hermann-Mauguin Symbol: Fddd Crystal System: Orthorhombic. Laue Class: mmm, Point Group: mmm, Bravais Lattice: F Lattice Symbol: oF.

Phase 2: Lithium Manganese Oxide (1/2/4), *cubic* spinel $LiMn_2O_4$, similar to ICSD card 40485 and JCPDS card 35-0782. Number of Space group: 227,Hermann-Mauguin Symbol: Fd-3m, Crystal System: Cubic, Laue Class: m-3m, Point Group: m-3m, Bravais Lattice: F, Lattice Symbol: cF.

Phase 3: Dilithium Manganese (IV) Trioxide, Li_2MnO_3 close to cards JCPDS 84-1634, ICSD 83848 and ICSD 202639. Number of Space group: 12, Hermann-Mauguin Symbol: C 1 2/M 1, Crystal System: Monoclinic, Laue Class: 2/m, Point Group: 2/m, Bravais Lattice: C, Lattice Symbol: mC.

Sample	t_{meas} [°C]	Cell parameters [Å] of the individual phases	Fract. (%)	Volume [Å^3]	Bragg R-factor	RF factor
$LiMn_2O_4$ Aldrich as supplied	50	1) $LiMn_2O_4$: $\alpha=\beta=\gamma=90^o$ a=b=c=8.2433(7).	1) 95.06 ±0.28	560.14	7.57	7.52
		2) Li_2MnO_3: $\alpha=\gamma=90^o$, $\beta=109.398(3)^o$, a=4.9246(6), b=8.5216(6), c=5.0245(6)	2) 4.94 ±0.01	198.89	56.9	49.1
$LiMn_2O_4$ Aldrich as supplied	-25	1) $LiMn_2O_4$: $\alpha=\beta=\gamma=90^o$ a=8.2063(5), b=8.2423(5), c=8.2907(5)	1) 62.64 ±0.21	560.77	11.5	8.45
		2) $LiMn_2O_4$: $\alpha=\beta=\gamma=90^o$ a=b=c=8.2379(7)	2) 32.42 ±0.08	559.04	8.09	7.82
		3) Li_2MnO_3: $\alpha=\gamma=90^o$, $\beta=109.398(3)^o$, a=4.9246(6), b=8.5216(6), c=5.0245(6)	3) 4.94 ±0.01	198.89	55.5	38.4

Table 7.10. Numerical results of Rietveld refinement for $LiMn_2O_4$ (Sigma - Aldrich Co.), samples as supplied.

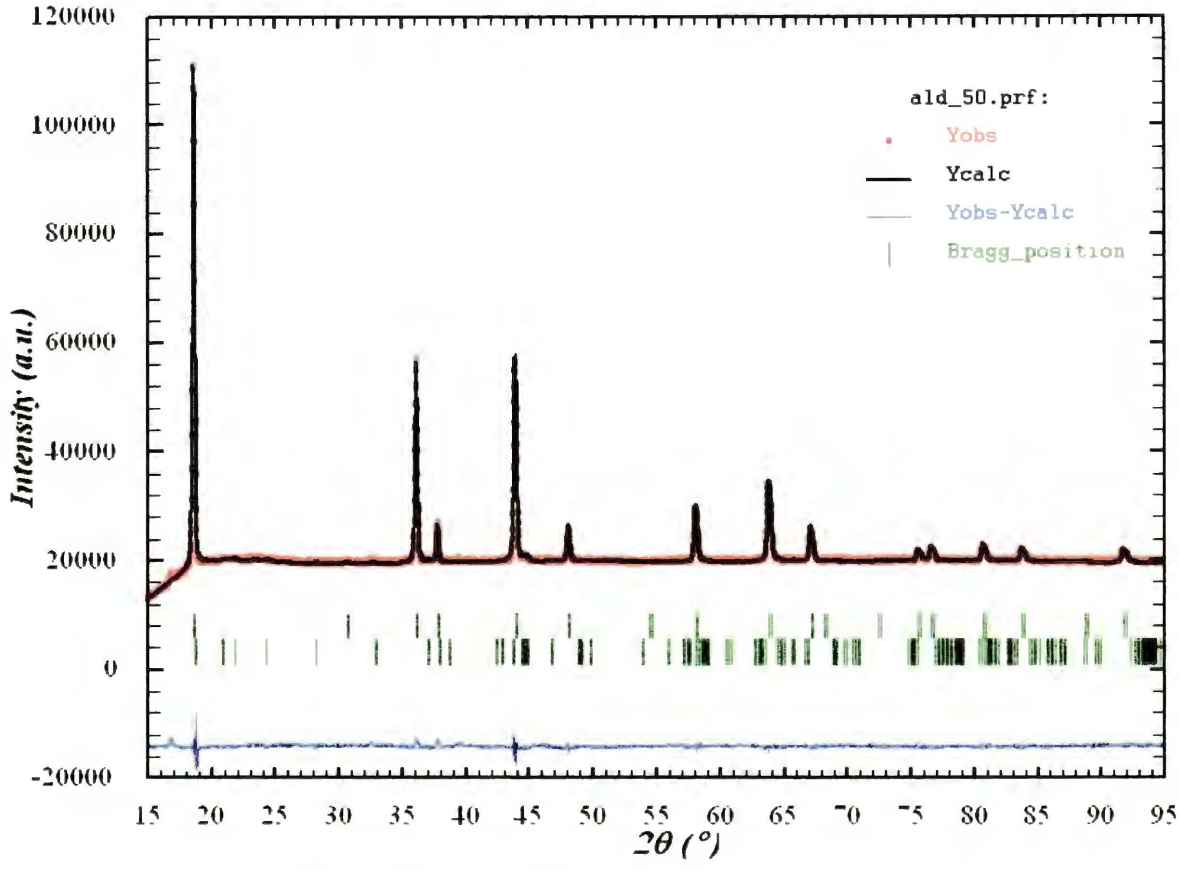

Fig. 7.32. Graphical results of Rietveld refinement for $LiMn_2O_4$ (Sigma - Aldrich Co.), sample as supplied (measured at 50°C).

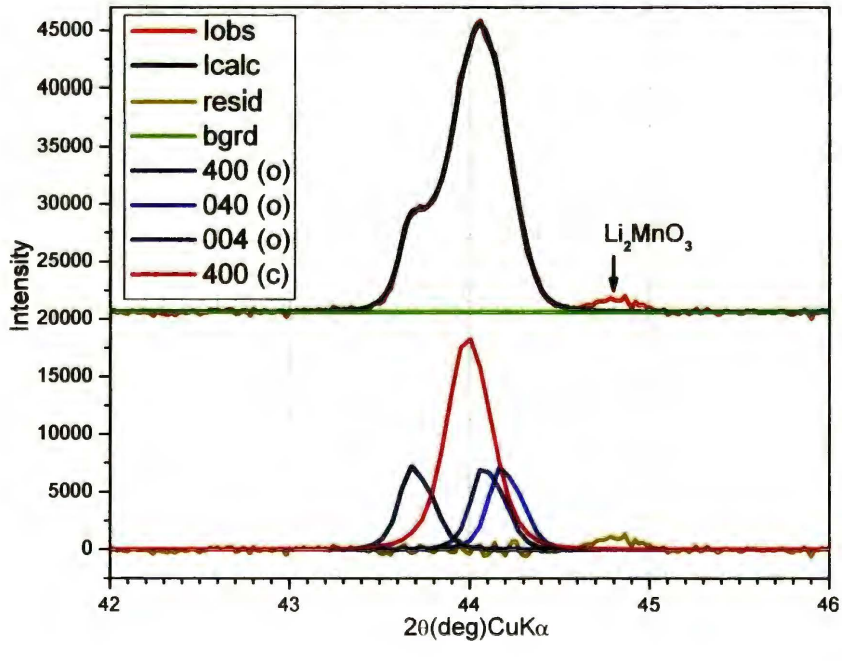

Fig. 7.33. Single peak refinement for $LiMn_2O_4$ (Sigma - Aldrich Co.), sample us supplied (measured at -25°C).

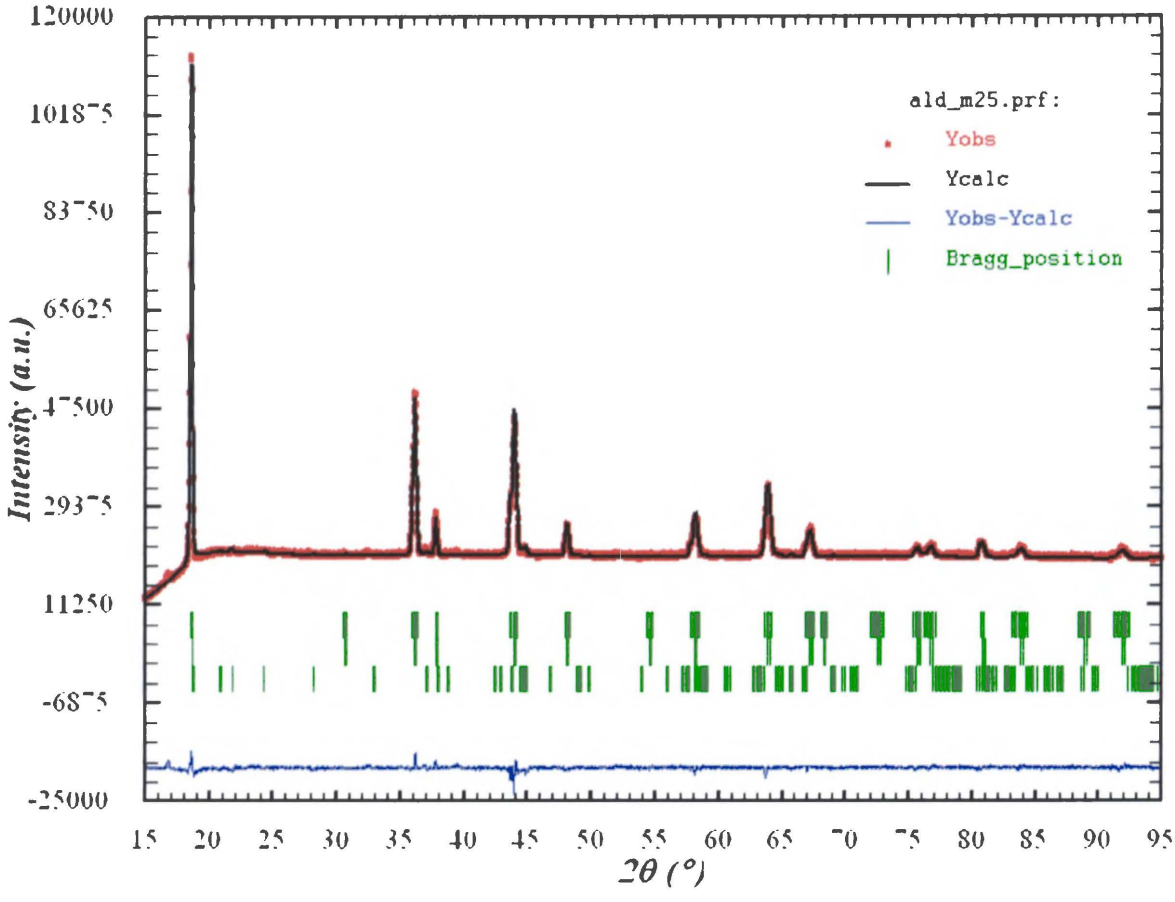

Fig. 7.34. Graphical results of Rietveld refinement for $LiMn_2O_4$ (Sigma - Aldrich Co.), sample as supplied (measured at -25°C).

7.5.2. Heated up to 800°C

a) XRD measurements

After heat treatment at 800°C the quantity of impurity phase was diminished down to 3.45%. as follows from Rietveld refinement; results are shown in Table 7.11., Fig 7.36.and Fig 7.37.

Sample	t_{meas} [°C]	Cell parameters [Å] of the individual phases	Fract. (%)	Volume [Å^3]	Bragg R-factor	RF factor
$LiMn_2O_4$ Aldrich heated up to 800°C	50	1) $LiMn_2O_4$: α=β=γ=90° a=b=c=8.2446(5).	1) 96.55 ±0.60	560.41	8.55	7.07
		2) Li_2MnO_3 : α=γ=90°, β=109.398(3)°, a=4.9246(6), b=8.5216(6), c=5.0245(6)	2) 3.45 ±0.07	198.89	65.7	44.0
$LiMn_2O_4$ Aldrich heated up to 800°C	-25	1) $LiMn_2O_4$: α=β=γ=90° a=8.2065(5), b=8.2409(5), c=8.2902(5)	1) 49.64 ±0.73	560.65	13.1	12.4
		2) $LiMn_2O_4$: α=β=γ=90° a=b=c=8.2451(7)	2) 46.80 ±0.65	560.51	10.21	7.42
		3) Li_2MnO_3 : α=γ=90°, β=109.398(3)°, a=4.9246(6), b=8.5216(6), c=5.0245(6)	3) 3.56 ±0.06	198.89	58.4	47.6

Table 7. 11. Numerical results of Rietveld refinement for $LiMn_2O_4$ (Sigma - Aldrich Co.), samples heated up to 800°C.

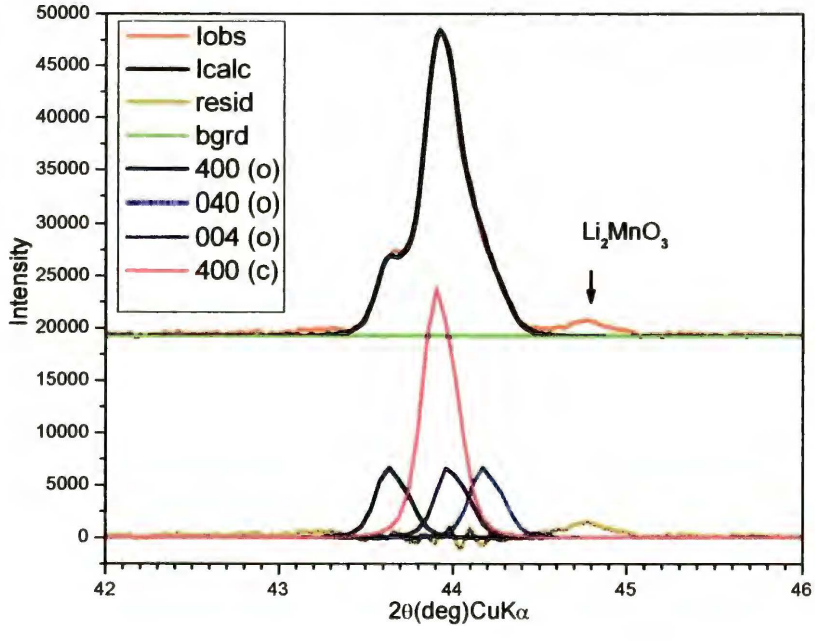

Fig. 7.35. Single peak refinement for $LiMn_2O_4$ (Sigma - Aldrich Co.), sample heated up to 800°C (measured at -25°C).

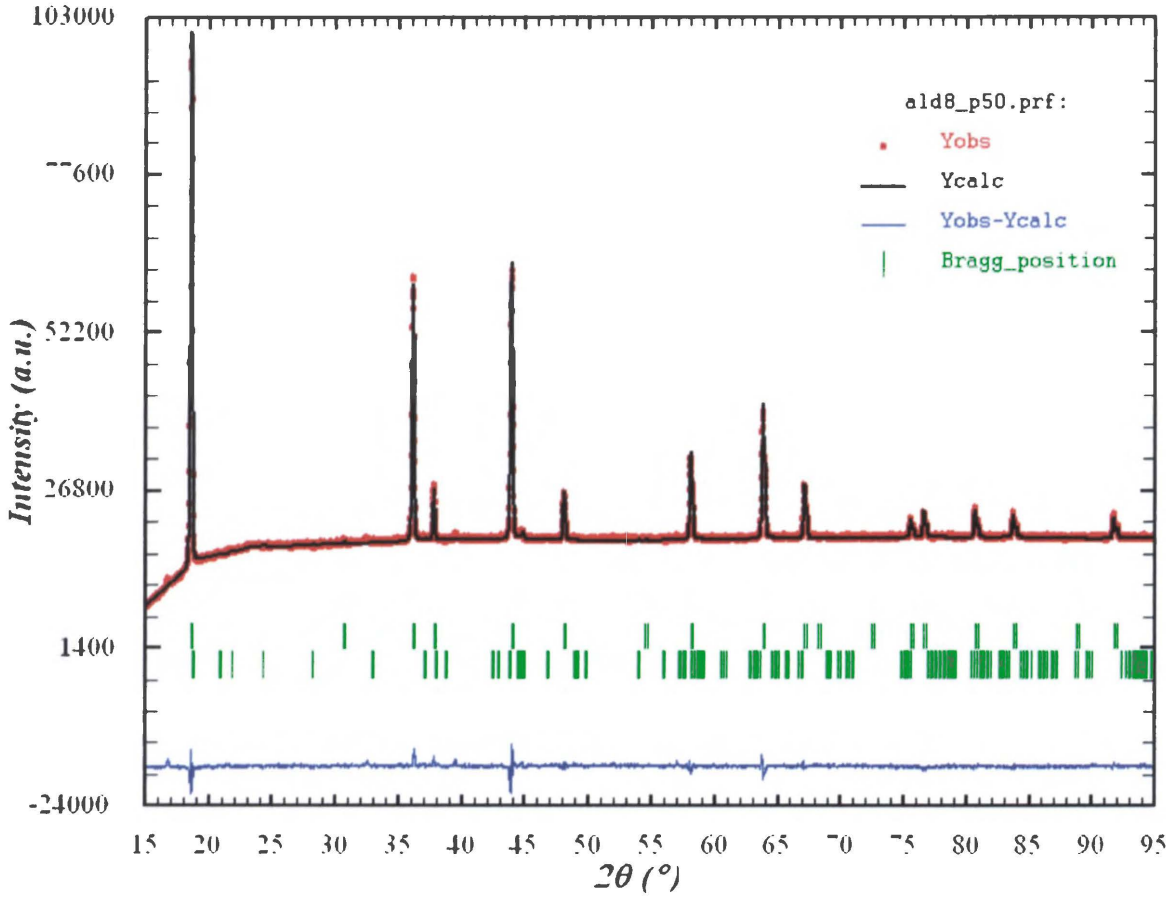

Fig. 7.36. Graphical results of Rietveld refinement for $LiMn_2O_4$ (Sigma - Aldrich Co.), sample heated up to 800°C (measured at 50°C).

At 50°C the sample consists of following two phases:

Phase 1: Lithium Manganese Oxide (1/2/4), spinel $LiMn_2O_4$, similar to cards JCPDS 35-0782 and ICSD 40485. Number of Space group: 227, Hermann-Mauguin Symbol: Fd-3m, Crystal System: Cubic, Laue Class: m-3m, Point Group: m-3m, Bravais Lattice: F, Lattice Symbol: cF.

Phase 2: Dilithium Manganese (IV) Trioxide, Li_2MnO_3 close to cards JCPDS 84-1634, ICSD 83848 and ICSD 202639. Number of Space group: 12, Hermann-Mauguin Symbol: C 1 2/M 1, Crystal System: Monoclinic, Laue Class: 2/m, Point Group: 2/m, Bravais Lattice: C, Lattice Symbol: mC.

At -25°C (after phase transition of the main phase) the sample consists of the following three phases:

Phase 1: Lithium Manganese Oxide (1/2/4), *orthorhombic* spinel $LiMn_2O_4$, close to cards JCPDS 88-0544 and ICSD 84842. Number of Space group: 70, Hermann-Mauguin Symbol:

Fddd Crystal System: Orthorhombic. Laue Class: mmm, Point Group: mmm, Bravais Lattice: F Lattice Symbol: oF.

Phase 2: Lithium Manganese Oxide (1/2/4), *cubic* spinel $LiMn_2O_4$, similar to ICSD card 40485 and JCPDS card 35-0782. Number of Space group: 227,Hermann-Mauguin Symbol: Fd-3m, Crystal System: Cubic, Laue Class: m-3m, Point Group: m-3m, Bravais Lattice: F, Lattice Symbol: cF.

Phase 3: Dilithium Manganese (IV) Trioxide, Li_2MnO_3 close to cards JCPDS 84-1634, ICSD 83848 and ICSD 202639. Number of Space group: 12, Hermann-Mauguin Symbol: C 1 2/M 1, Crystal System: Monoclinic, Laue Class: 2/m, Point Group: 2/m, Bravais Lattice: C, Lattice Symbol: mC.

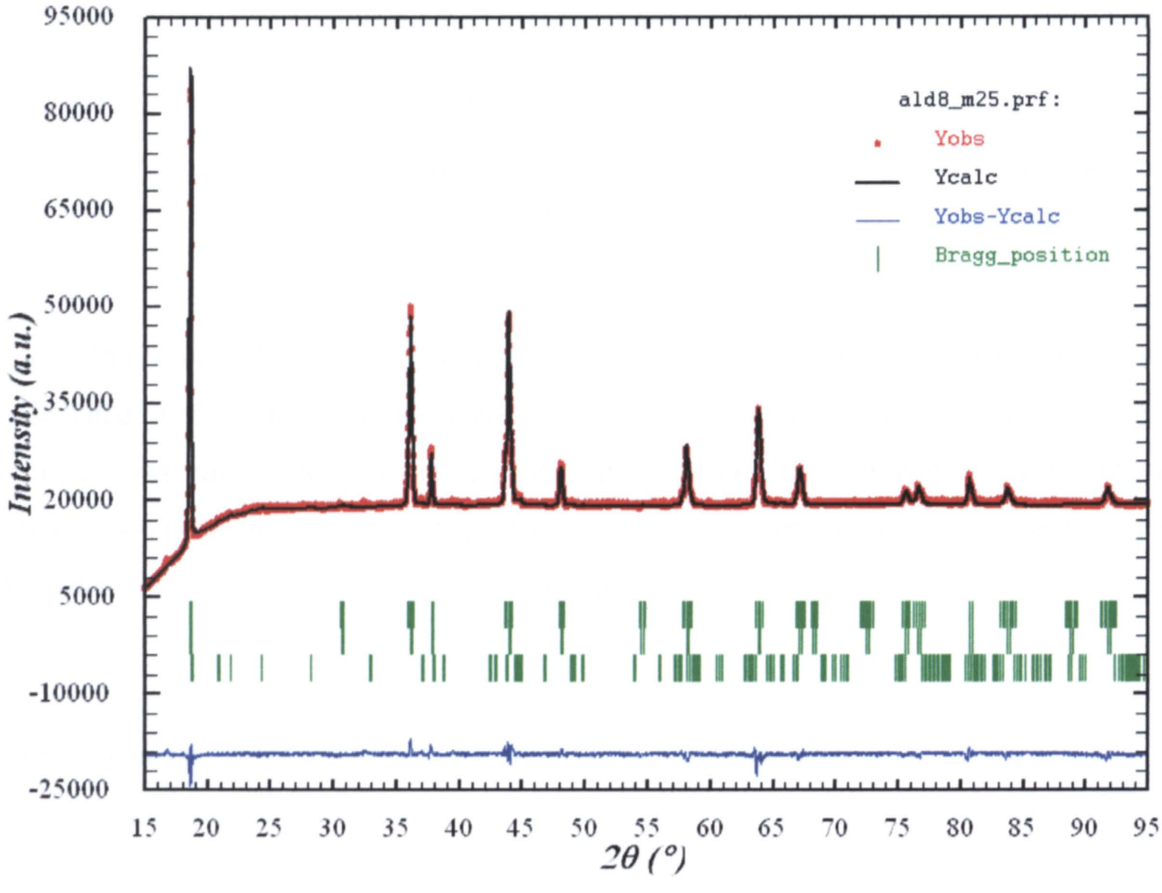

Fig. 7.37. Graphical results of Rietveld refinement for $LiMn_2O_4$ (Sigma - Aldrich Co.), sample heated up to 800°C (measured at -25°C).

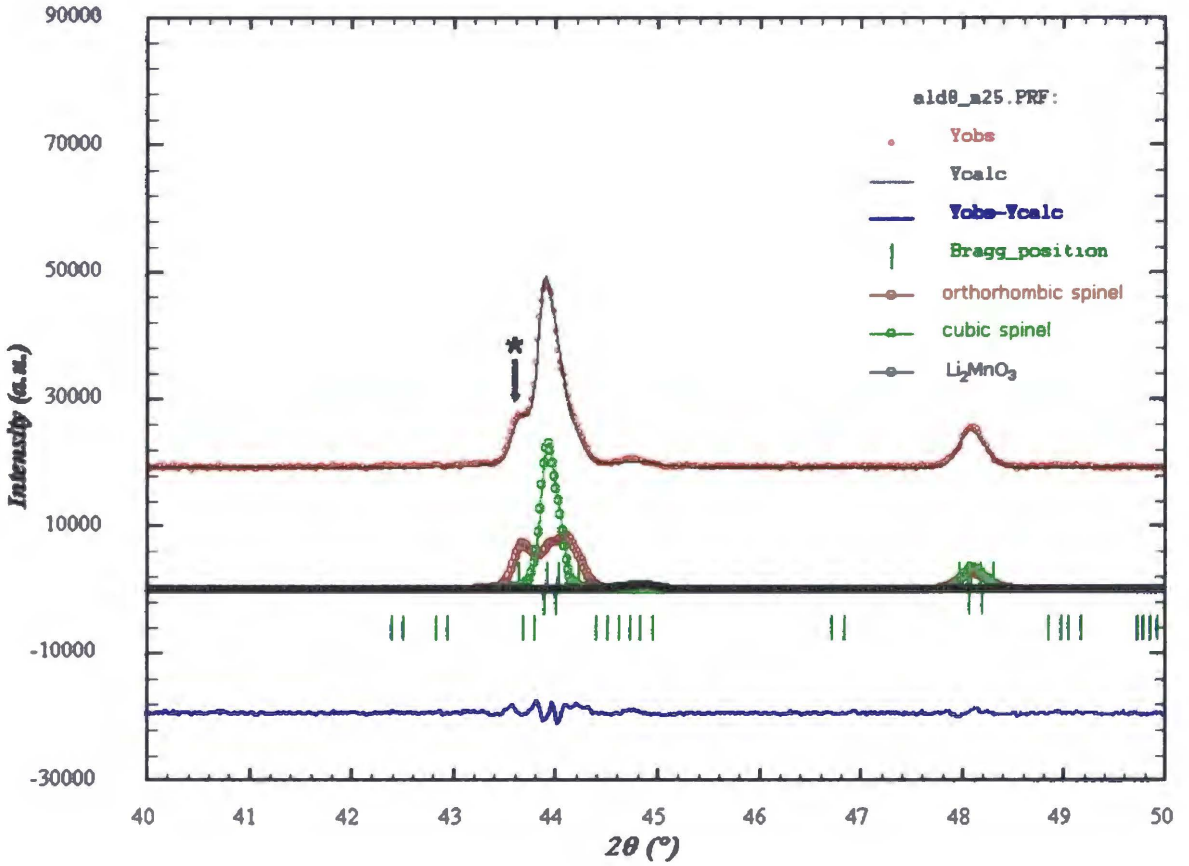

Fig. 7.38. Portion of the pattern around 400 reflection with performed decomposition of the calculated profile onto individual components (phases). Green circles show the cubic spinel, brown circles show the orthorhombic spinel, black circles show the Li_2MnO_3 phase. (*corresponds to the same reflection from the copper electrode as on the pattern from simultaneous XRD and impedance spectroscopy measurements).

b) Simultaneous XRD and impedance spectroscopy measurements

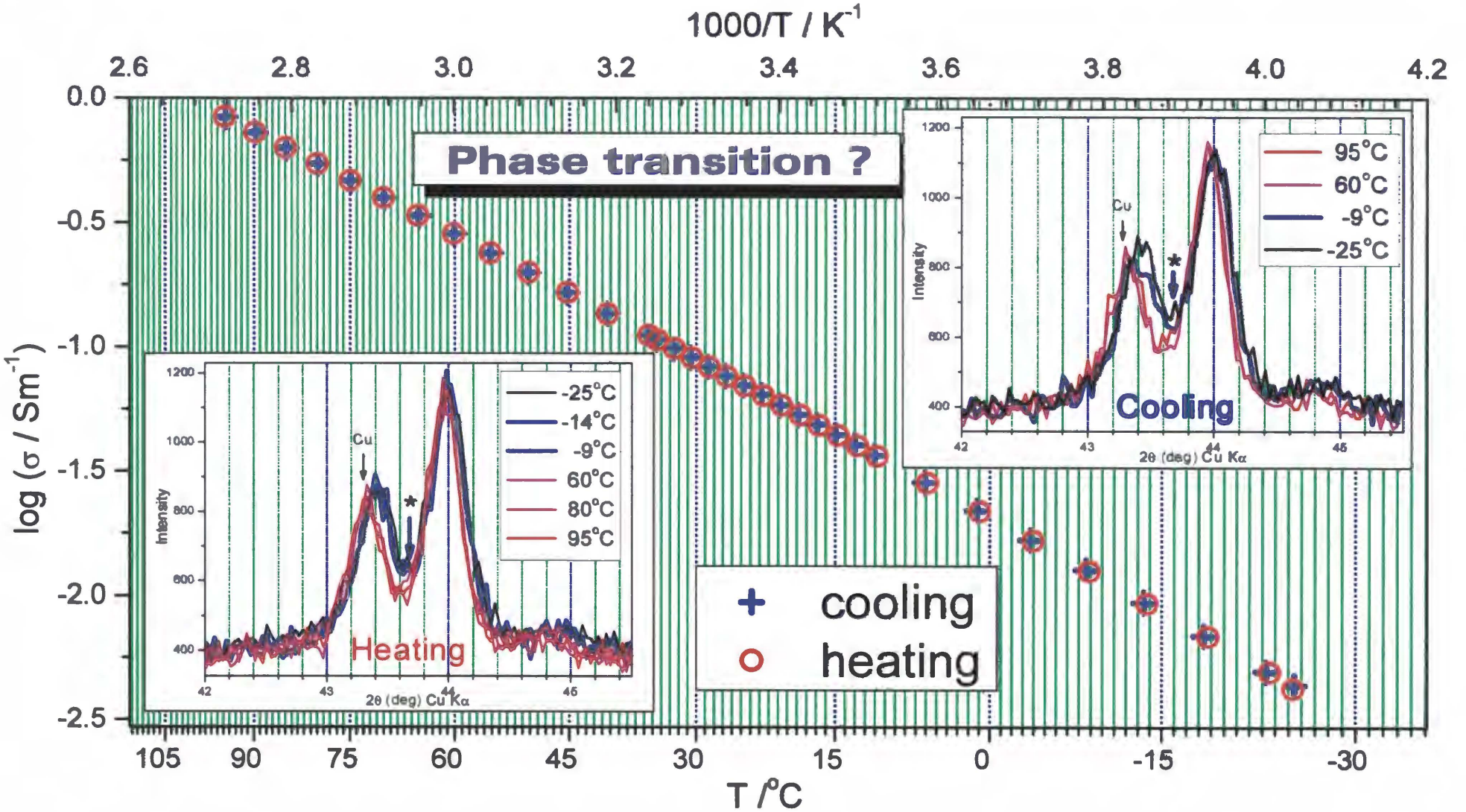

Fig.7.39.Temperature dependency of conductivity correlated with 400 peak shape for $LiMn_2O_4$ (Sigma - Aldrich Co.), sample heated up to 800°C.

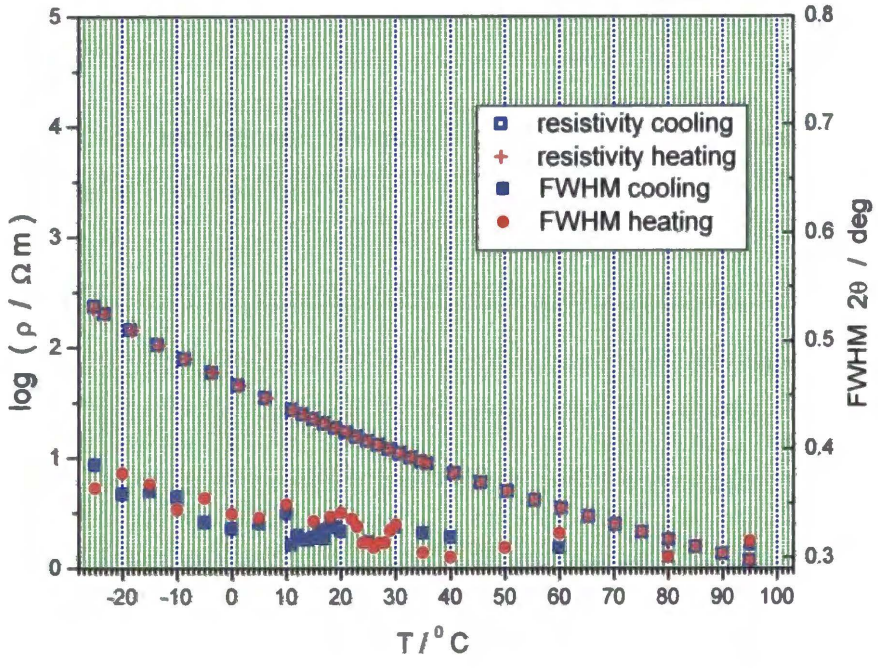

Fig. 7.40. Temperature dependence of FWHM of complex peak around 44° 2θ fitted as one peak correlated with resistivity for $LiMn_2O_4$ (Sigma - Aldrich Co.), sample heated up to 800°C.

7.6. $Li_{1.0237}Mn_{1.9763}O_4$ and $Li_{1.0392}Mn_{1.9608}O_4$ supplied by Honeywell Specialty Chemicals Company

Results of Rietveld analysis are shown in Fig. 7.41, Fig. 7.42 and Table 7.12. At 25°C the samples consist of only one phase.

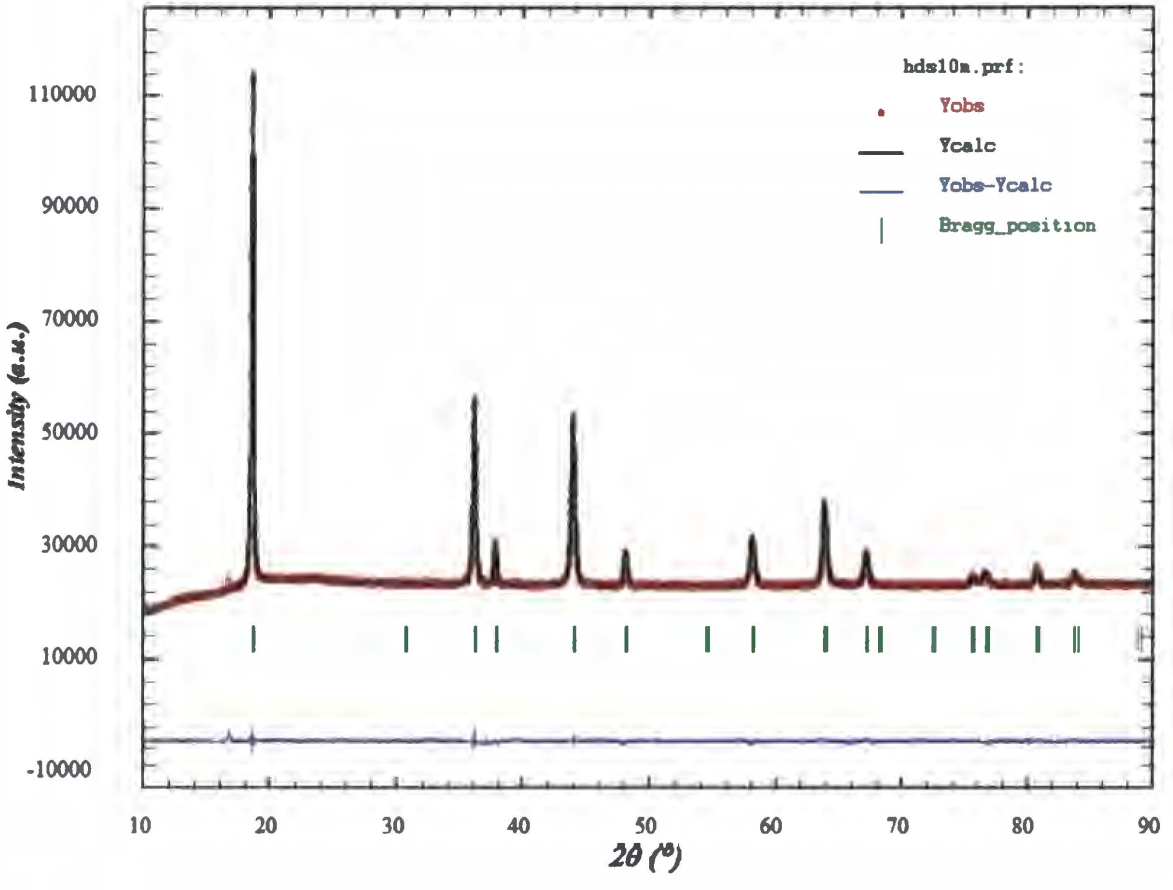

Fig. 7.41. Graphical results of Rietveld refinement for $Li_{1.0237}Mn_{1.9763}O_4$ sample (supplied by Honeywell Specialty Chemicals Co.), sample measured at 25°C.

Sample	t_{meas} [°C]	Cell parameters [Å]	Fract. (%)	Volume [Å^3]	Bragg R-factor	RF factor
$Li_{1.0237}Mn_{1.9763}O_4$ (Honeywell Specialty Chemicals)	25	δ-spinel α=β=γ=90° a=b=c=8.2342(9)	100	558.30	3.25	2.88
$Li_{1.0392}Mn_{1.9608}O_4$ (Honeywell Specialty Chemicals)	25	δ-spinel α=β=γ=90° a=b=c=8.2304(9)	100	557.52	2.50	2.22

Table. 7.12. Numerical results of Rietveld refinement for $Li_{1.0237}Mn_{1.9763}O_4$ and $Li_{1.0392}Mn_{1.9608}O_4$ samples (supplied by Honeywell Specialty Chemicals Co.)

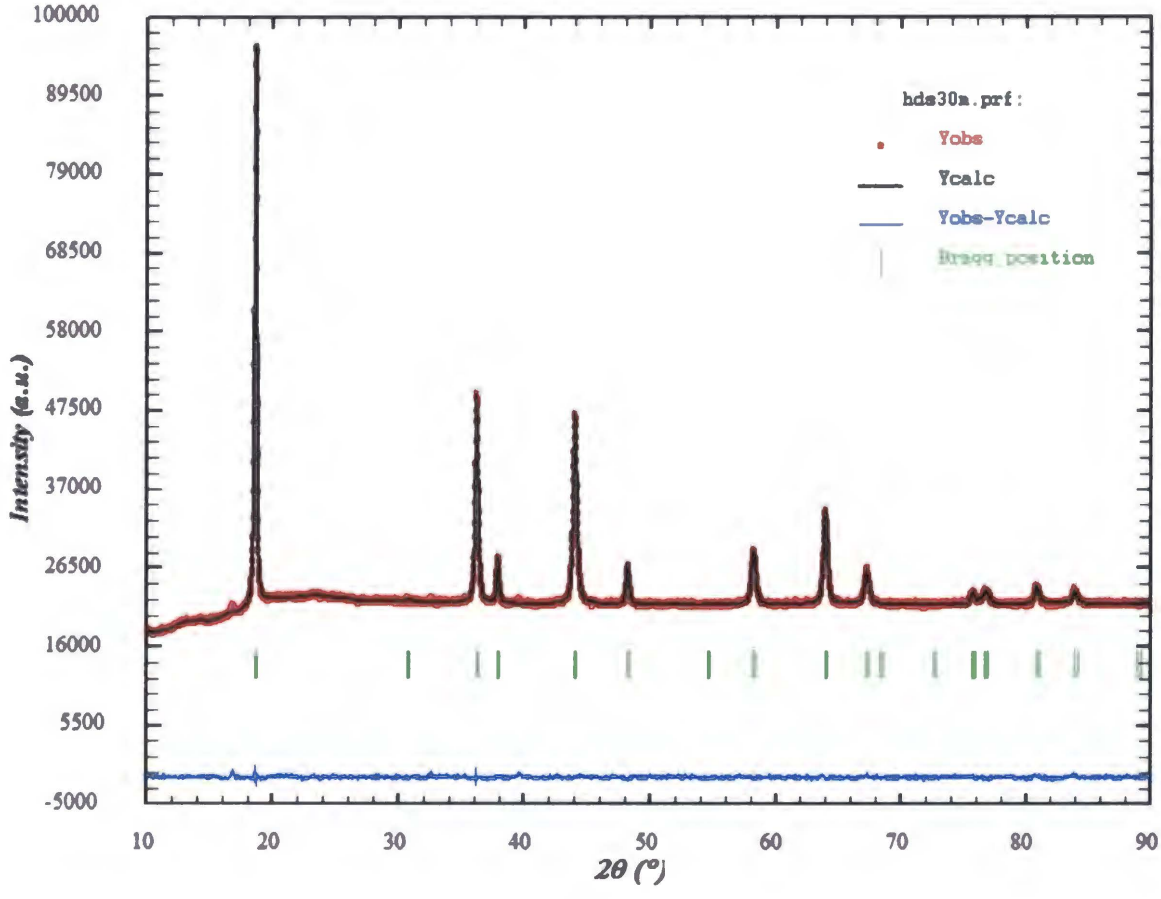

Fig. 7.42. Graphical results of Rietveld refinement for $Li_{1.0392}Mn_{1.9608}O_4$ sample (supplied by Honeywell Specialty Chemicals Co.), sample measured at 25°C.

At 25°C the samples consist of the following spinel phase:

Lithium Manganese Oxide, cubic δ-spinel $Li_{1.0237}Mn_{1.9763}O_4$ and $Li_{1.0392}Mn_{1.9608}O_4$, close to ICSD card 40485 and JCPDS card 35-0782, Number of Space group: 227, Hermann-Mauguin Symbol: Fd-3m, Crystal System: Cubic, Laue Class: m-3m, Point Group: m-3m, Bravais Lattice: F, Lattice Symbol: cF.

7.7. $Li_{1.20}Mn_{1.80}O_4$ synthesized by high and low temperature sol-gel method

7.7.1. $Li_{1.20}Mn_{1.80}O_4$ synthesized by low temperature sol-gel method

At 25°C the sample consists of two phases.

Phase 1: Lithium Manganese Oxide, (4/5/12), spinel $Li_4Mn_5O_{12}$, similar to JCPDS card 46-0810, Number of Space group: 227, Hermann-Mauguin Symbol: Fd-3m, Crystal System: Cubic, Laue Class: m-3m, Point Group: m-3m, Bravais Lattice: F, Lattice Symbol: cF.

Phase 2: Lithium Manganese Oxide, (1/2/4), cubic spinel $LiMn_2O_4$, close to ICSD card 40485 and JCPDS card 35-0782, Number of Space group: 227, Hermann-Mauguin Symbol: Fd-3m, Crystal System: Cubic, Laue Class: m-3m, Point Group: m-3m, Bravais Lattice: F, Lattice Symbol: cF.

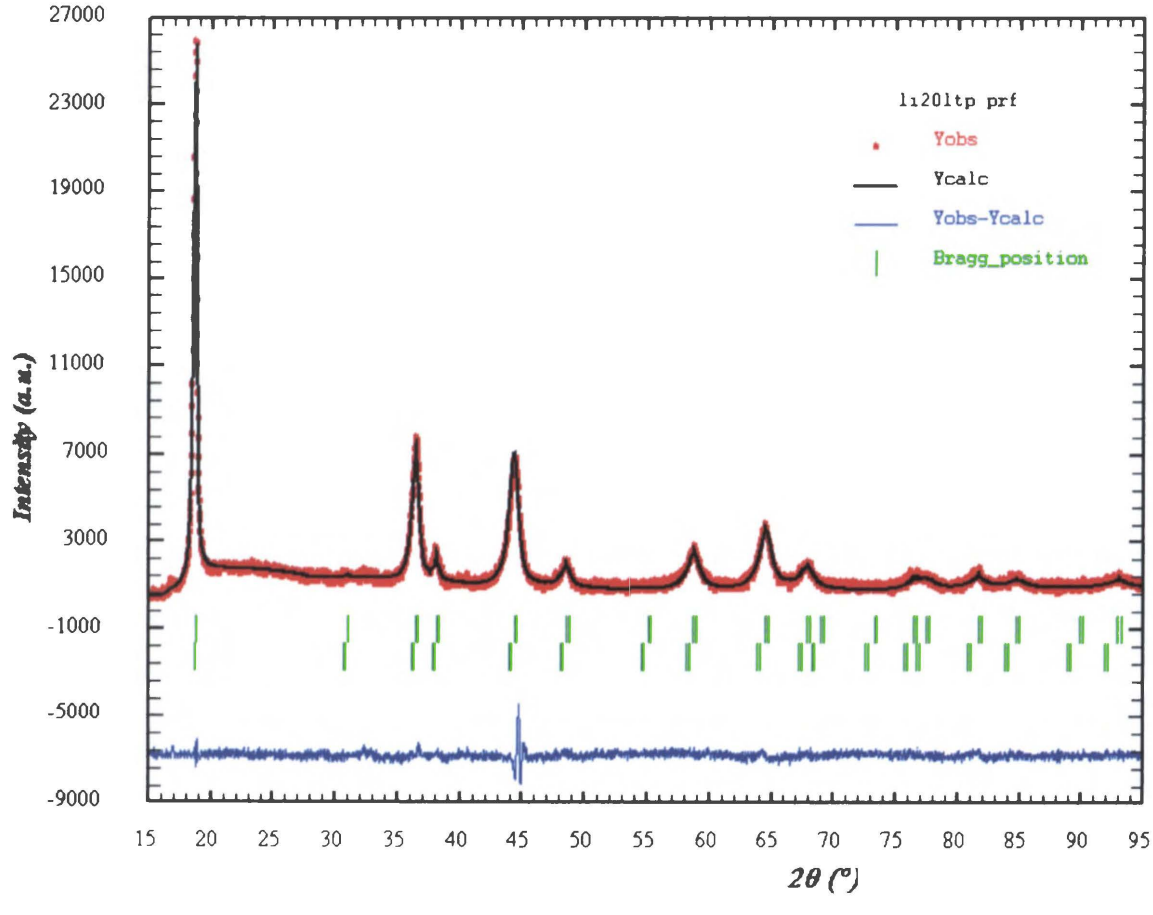

Fig. 7.43. Graphical results of Rietveld refinement for $Li_{1.20}Mn_{1.80}O_4$ (low temperature sol-gel synthesis), sample measured at 25°C.

The numerical results for all group of $Li_{1.20}Mn_{1.80}O_4$ samples (low and high temperature sol-gel synthesis) are presented in Table 7.13.

Sample	t_{treat} [°C]	Cell parameters [Å] of the individual phases	Fract. (%)	Volume [Å^3]	Bragg R-factor	RF factor
$Li_{1.20}Mn_{1.80}O_4$ Sol-gel heated up to 300°C during synthesis	as is	1) $Li_4Mn_5O_{12}$: $\alpha=\beta=\gamma=90^o$ a=b=c=8.1635(1).	1) 88.26 ±0.64	544.04	4.91	4.15
		2) $LiMn_2O_4$: $\alpha=\beta=\gamma=90^o$ a=b=c=8.2372(2).	2) 11.74 ±0.06	558.91	7.24	5.69
$Li_{1.20}Mn_{1.80}O_4$ Sol-gel heated up to 300°C during synthesis	600	1) spinel $\alpha=\beta=\gamma=90^o$ a=b=c=8.1862(1).	100	548.59	3.67	3.07
$Li_{1.20}Mn_{1.80}O_4$ Sol-gel heated up to 300°C during synthesis	800	1) $LiMn_2O_4$: $\alpha=\beta=\gamma=90^o$ a=b=c=8.2319(2).	1) 92.22 ±0.64	557.82	5.61	3.98
		2) Li_2MnO_3 : $\alpha=\gamma=90^o$, $\beta=109.01(9)^o$, a=4.9290(7), b=8.5319(8), c=5.0258(7)	2) 7.78 ±0.17	199.86	30.6	22.2
$Li_{1.20}Mn_{1.80}O_4$ Sol-gel heated up to 800°C during synthesis	as is	1) $LiMn_2O_4$: $\alpha=\beta=\gamma=90^o$ a=b=c=8.2116(2).	1) 91.89 ±1.17	553.71	5.93	5.24
		2) Li_2MnO_3 : $\alpha=\gamma=90^o$, $\beta=109.10(9)^o$, a=4.9297(8), b=8.5348(9), c=5.0240(8)	2) 8.11 ±0.19	199.72	28.2	21.6

Table 7.13. Numerical results of Rietveld refinement for $Li_{1.20}Mn_{1.80}O_4$ samples (low and high temperature sol-gel synthesis), all measurements performed at 25°C. The temperatures of additional heat treatments of the samples are shown in $t_{treat.}$ column.

7.7.2. $Li_{1.20}Mn_{1.80}O_4$ synthesized by low temperature sol-gel method and heat treated up to 600°C

At 25°C the sample consists of following spinel phase:
Lithium Manganese Oxide, (spinel type), close to card JCPDS 35-0782 or ICSD #40485. Number of Space group: 227, Hermann-Mauguin Symbol: Fd-3m, Crystal System: Cubic, Laue Class: m-3m, Point Group: m-3m, Bravais Lattice: F, Lattice Symbol: cF.

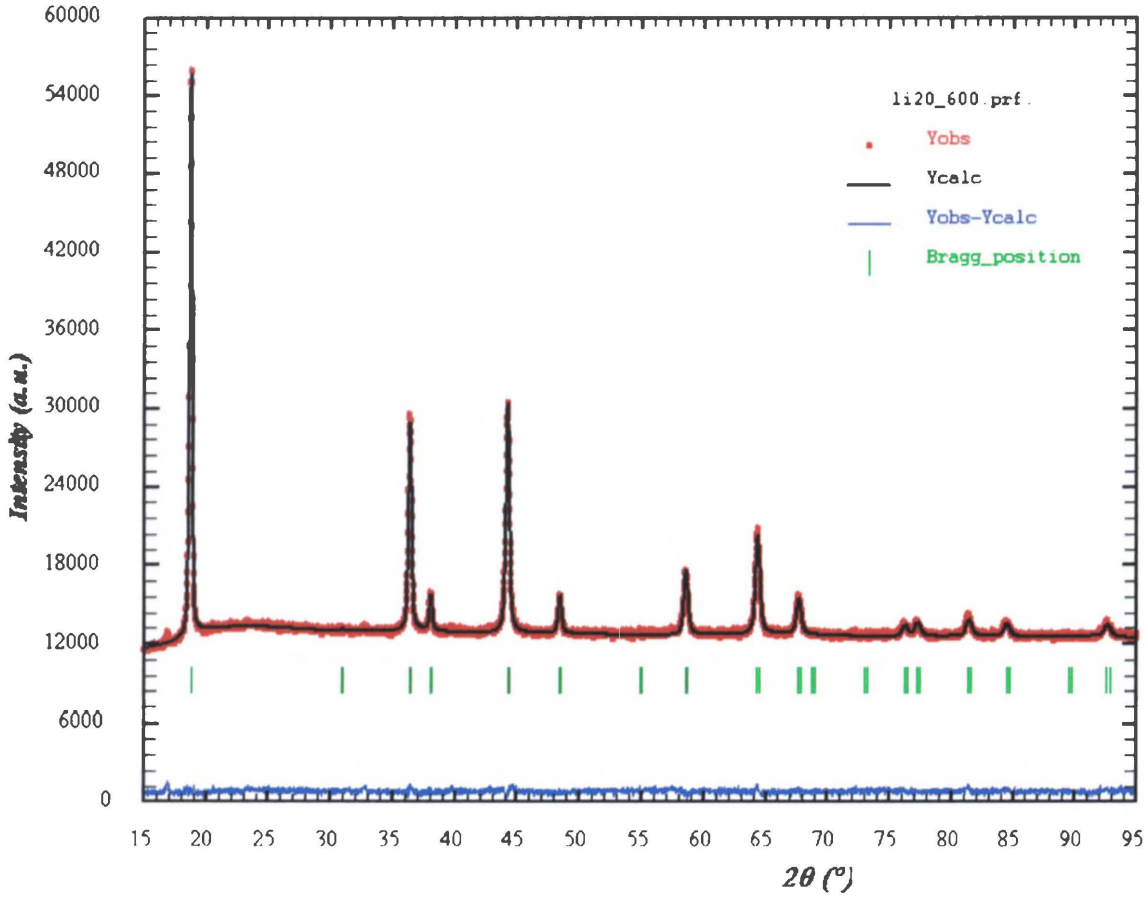

Fig. 7.44. Graphical results of Rietveld refinement for $Li_{1.20}Mn_{1.80}O_4$ (low temperature sol-gel synthesis) additionally heated up to 600°C, sample measured at 25°C.

7.7.3. $Li_{1.20}Mn_{1.80}O_4$ synthesized by low temperature sol-gel method and heat treated up to 800°C

At 25°C the sample consists of the two phases.

Phase1: Lithium Manganese Oxide (1/2/4), spinel $LiMn_2O_4$, similar to card JCPDS 35-0782 or ICSD #40485. Number of Space group: 227,Hermann-Mauguin Symbol: Fd-3m, Crystal System: Cubic, Laue Class: m-3m, Point Group: m-3m, Bravais Lattice: F, Lattice Symbol: cF.

Phase2: Dilithium Manganese (IV) Trioxide, Li_2MnO_3 close to card JCPDS 84-1634 or ICSD #202639 and ICSD#83848. Number of Space group: 12, Hermann-Mauguin Symbol: C 1 2/M 1, Crystal System: Monoclinic, Laue Class: 2/m, Point Group: 2/m, Bravais Lattice: C, Lattice Symbol: mC.

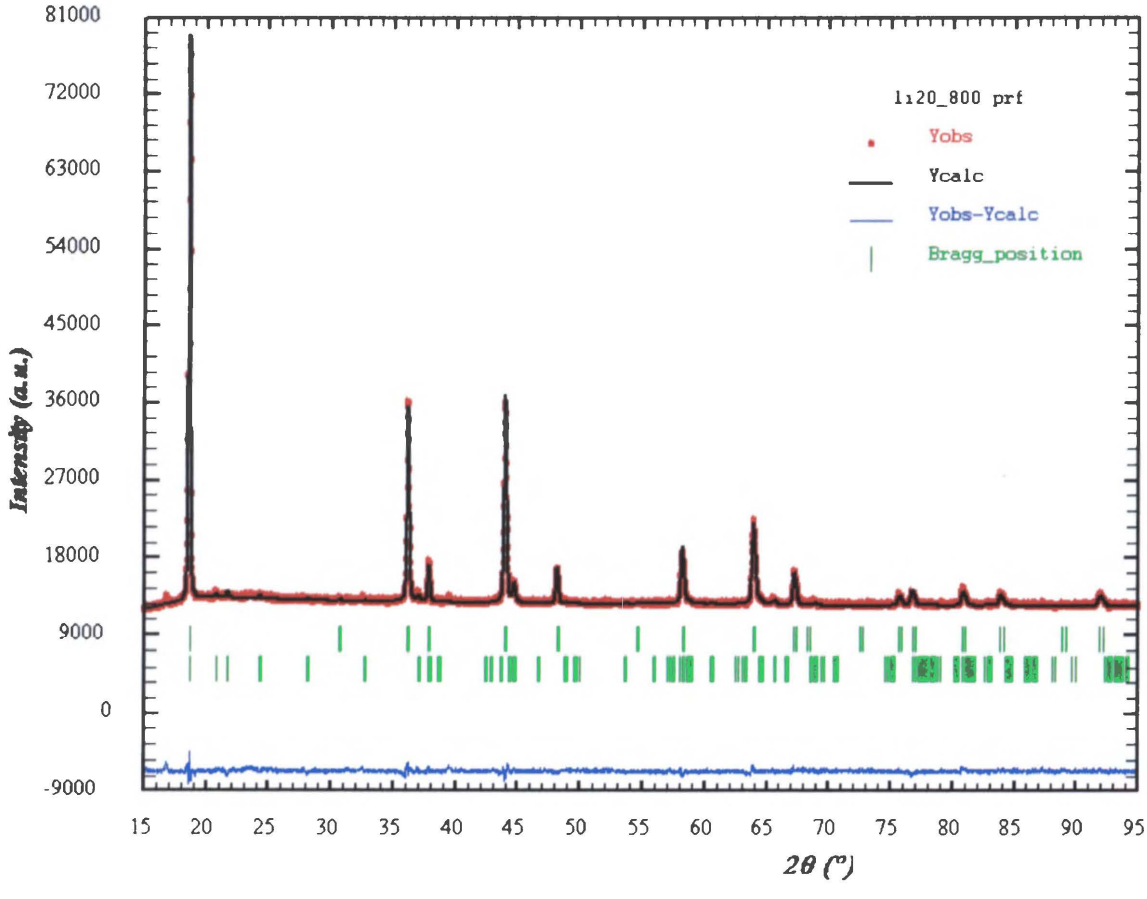

Fig. 7.45. Graphical results of Rietveld refinement for $Li_{1.20}Mn_{1.80}O_4$ samples (low temperature sol-gel synthesis) additionally heated up to 800°C, sample measured at 25°C.

7.7.4. $Li_{1.20}Mn_{1.80}O_4$ synthesized by high temperature sol-gel method

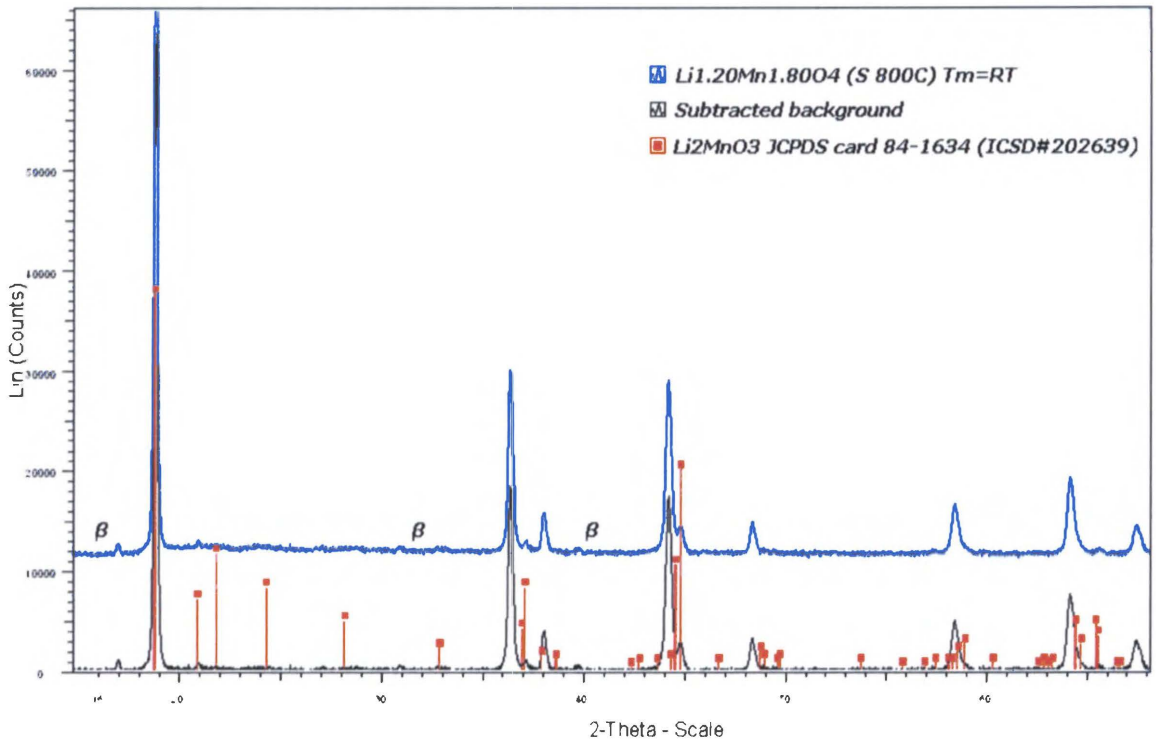

Fig. 7.46. Part of XRD pattern of the $Li_{1.20}Mn_{1.80}O_4$ sample (high temperature sol-gel synthesis) with reference lines of the Li_2MnO_3 phase.

At 25°C the sample consists of the two phases:

Phase1: Lithium Manganese Oxide (1/2/4), spinel $LiMn_2O_4$, similar to card JCPDS 35-0782 or ICSD #40485. Number of Space group: 227,Hermann-Mauguin Symbol: Fd-3m, Crystal System: Cubic, Laue Class: m-3m, Point Group: m-3m, Bravais Lattice: F, Lattice Symbol: cF,

Phase2: Dilithium Manganese (IV) Trioxide, Li_2MnO_3 close to card JCPDS 84-1634 or ICSD #202639 and ICSD#83848. Number of Space group: 12, Hermann-Mauguin Symbol: C 1 2/M 1, Crystal System: Monoclinic, Laue Class: 2/m, Point Group: 2/m, Bravais Lattice: C, Lattice Symbol: mC.

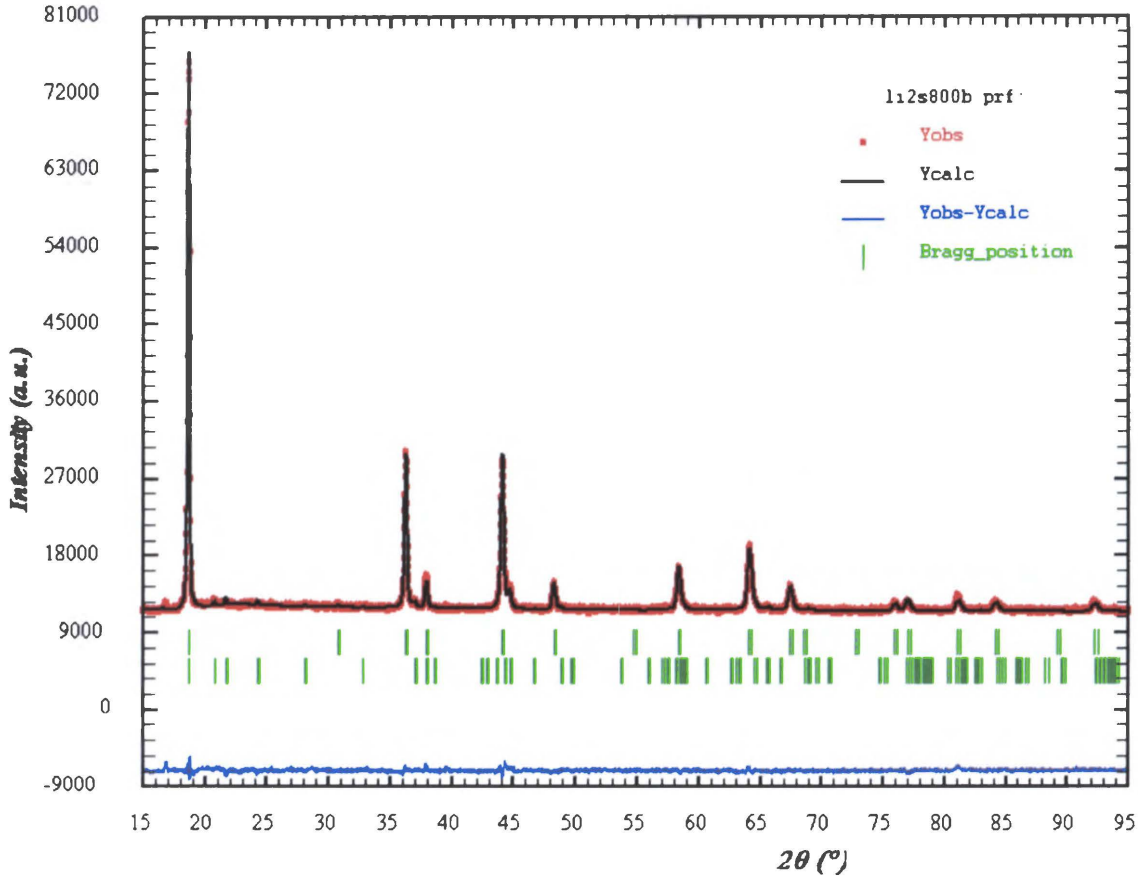

Fig. 7.47. Graphical results of Rietveld refinement for $Li_{1.20}Mn_{1.80}O_4$ (high temperature sol-gel synthesis), sample measured at 25°C.

8. SUMMARY OF THE RESULTS

The results of structural and electric measurements can be summarized for particular type of samples as follows:

8.1. $LiMn_2O_4$ and $Li_{1.005}Mn_{1.995}O_4$ synthesized by low temperature sol-gel method

XRD measurements at 25°C show that both of the samples exhibit diffraction lines corresponding to typical cubic spinel structure. The XRD patterns show strong broadening of diffraction lines related to small average crystallite size and probably to the structural defects. In these samples, seemingly consisting of only one phase, additional phases were found using Rietveld analysis. The cell parameters of the dominating phases are quite low for stoichiometric $LiMn_2O_4$ spinel. Such low cell parameters could be attributed to defected spinel structure with a general formula $Li_4Mn_5O_{12}$ [48]. The second phase has for both type of samples cell parameter very close to $LiMn_2O_4$ stoichiometric spinel. The last minor impurity phase for these samples is manganese oxide Mn_3O_4. Such type of oxides is quite typical impurity phase [49] for samples received by sol-gel synthesis. It should be noted, however, that due to the possible presence of small amounts of amorphous, non-detectable by XRD phase, the concentrations calculated from Rietveld refinement are mostly indicative of the XRD-detectable nanocrystalline phases. Additionally, calculated structural parameters can be burdened by some uncertainty because of very close kinship of the spinel phases and very low content of the minor impurity phases. Presence of additional phases is confirmed by visible left side asymmetry of main spinel peaks and by presence of additional weak peaks unusual for spinel structures. The received results are at the limit of application of Rietveld refinement method, especially when, as in the case under study, there are so little differences in phase composition between stoichiometric and delta spinels. Nevertheless this method is practically the only one which allows finding multiphase nature of such samples. In these samples any anomalous electrical properties at temperatures close to room temperature was observed. It means that both lithium manganese spinels (stoichiometric and delta) obtained by low temperature sol-gel method do not undergo the phase transition.

8.1.1. $LiMn_2O_4$ and $Li_{1.005}Mn_{1.995}O_4$ synthesized by low temperature sol-gel method and additionally heat treated up to 580°C

After heat treatment up to 580°C the spinel peaks become narrower, shifting towards low diffraction angles and become more symmetrical. It reflects an increase of cell parameter and increase of average crystallite size as wall as an increase of homogeneity of both samples. The heat treated samples consist of only one spinel phase and the minor manganese oxide impurities concentration is about three times lower. The quantities of the impurities can not be estimated more precisely by this method because of their very low content in the samples.

8.1.2. $LiMn_2O_4$ and $Li_{1.005}Mn_{1.995}O_4$ synthesized by low temperature sol-gel method and additionally heat treated up to 800°C

During heat treating of the SL580 and DL580 samples up to 800°C, the processes of peaks shift, their sharpening and narrowing are continued due to the same reasons, i.e. cell constants increase and crystallites size growth. Peaks from impurity phase become less pronounced as a result of decrease of the content of the Mn oxide phase which can be estimated as less than 1%. Such small concentrations of additional phase are practically out of the reach of the qualitative analysis by XRD methods [50].

8.2. $LiMn_2O_4$ and $Li_{1.005}Mn_{1.995}O_4$ synthesized by high temperature sol-gel method

XRD patterns of samples obtained by high temperature sol-gel synthesis display only diffraction lines of cubic (Fd-3m) lithium manganese spinel phase. It means that formation of pure spinel phase is completed at temperatures close to 800°C. The average crystallite size of the samples is 2.5-3 times higher than in the case of samples obtained by low temperature sol-gel synthesis but it is still in nano range (35-44 nm).
Little difference between cell parameters of stoichiometric and delta spinel could probably be explained by presence in delta spinel sample bigger quantities of Mn 4+ ions (with lower ionic radius then Mn 3+ ions). In the case of stoichiometric Li-Mn spinel there is equal quantity of Mn 3+ and Mn 4+ ions occupying octahedral positions (Ionic radius of Mn in 3+ oxidation state in octahedral surrounding is 78.5 pm and Mn 4+ is 67 pm).

Samples synthesized by high temperature method undergo at lower (close to room) temperature, structural phase transition. XRD patterns recorded at -4°C indicate that at this temperature there is complete transformation to orthorhombic (Fddd) structure. The most visible effect of this phase transition is splitting of 400 reflection into 400, 040 and 004 reflections. The change corresponding to three different cell parameters is typical for orthorhombic phase as compared with one cell constant for cubic phase. It was thus possible to fit calculated profile to the observed one using orthorhombic structure model containing three peaks with exactly equal intensities and widths.

It should be also noted that these materials do not exhibit significant change in cell volume caused by the phase transition. Volume changes are 0.06% and 0.11% for SH and DH respectively. Such a small change of volume is one of characteristic features of the first order phase transition.

Combining impedance measurements and X-ray diffraction, measured either independently or in in-situ arrangement, electrical quantities like conductivity can be directly related to the structural information obtained from X-Ray diffraction. The samples were investigated over heating and cooling ramps, in the range from 100°C to -25°C, with narrow temperature steps of 1°C in the phase transition region, near room temperature. The impedance drift at a given temperature caused the measurement to be repeated until the change of impedance was below the predetermined value (0.6%) during spectral acquisition time, selected as 7 minutes.

Resistance of sample increased with time. Change of resistance was accompanied by change in the 400 peak shape.

Due to the fact that the orthorhombic distortion is minor, i.e. the change in lattice parameters is small, the cubic to orthorhombic transition can be manifested clearly only with the reflections of the h00 type, which undergo splitting during transition from cubic to orthorhombic structure. For the stoichiometric spinel virtually no changes of the X-ray diffraction pattern were recorded during cooling from 100° C down to 17°C. Also below 12°C down to -25°C there is no further broadening of the diffraction maximum. The evolution of shape and width of the X-ray diffraction pattern near the 400 reflection during the phase transformation is visible only in between these temperatures.

Detailed analysis of the X-ray diffraction pattern by fitting a combination of diffraction peaks, under assumption of presence of both cubic and orthorhombic phases of the spinel

during transformation, proved to be difficult, due to the limited resolution of the position sensitive detector and non-ideal geometry of diffraction. Therefore, the full width at the half maximum (FWHM) of the 400 reflection was chosen as a measure of progress of the phase transition. At temperatures from +20°C to +17°C the FWHM is almost constant and equal to 0.33 deg of 2θ (Fig.7.15.) The increase in resistance for this range is a consequence of decreasing temperature, following Arrhenius type of temperature dependence. When the resistivity starts to increase at a constant temperature of 16°C, the FWHM of the 400 reflection also increases, indicating change of the crystal structure and is following the increase of resistance throughout the temperature range in which phase transformation takes place. From 12°C the FWHM remains nearly constant at lower temperatures. The increase of resistance below that temperature follows Arrhenius dependence. Considering the time dependence at constant temperature, it is seen that the largest changes of resistivity and FWHM took place at 15°C. Decrease of conductivity with time at constant temperature can be fitted by an exponential decay. In this way a time constant describing the kinetics of phase transition was estimated to be equal to about 2 hours.

During heating, the phase transition from orthorhombic to cubic structure progressed over a range of temperature from 20°C to 40°C, but drift of impedance at constant temperature did not exceed the pre-set limit of 0.6%. Thus the isothermal time dependence of electric and structure parameters was not recorded.

In the case of delta spinel $Li_{1.005}Mn_{1.995}O_4$, the conductivity decreased by a factor about 5 during phase transformation upon cooling. Drift of impedance was detected at temperatures between 16°C and 9°C. Thus the temperature range of the phase transformation was broadened with respect to the stoichiometric spinel, while the cumulative decrease of conductivity was almost twice smaller.

By combining impedance measurements and X-ray diffraction, electrical quantities like conductivity can be directly related to the structural information obtained from X-ray diffraction patterns. Detection of drift of impedance allows automatic switching from temperature ramp to isothermal recording of time dependence of electric and structural parameters. In this way it was possible to follow the kinetics of a phase transition of the lithium manganese spinel. It was found that the phase change of the stoichiometric spinel occurred progressively during cooling from 16°C to 13°C, with the largest change of crystal structure and electrical conductivity at 15°C. In the course of phase transformation

the increase of resistance was well correlated with the extent of the orthorhombic distortion of the structure.

8.3. $LiMn_2O_4$ supplied by Alfa Aesar Company

8.3.1. As supplied

The XRD patterns of this material exhibit well defined, narrow reflections, which can be identified as belonging to $LiMn_2O_4$ cubic (Fd-3m) phase. Additional weak peaks of the minor phase were also observed. Subsequently these peaks have been attributed to dimanganese (III) manganese oxide Mn_3O_4. Generally the minor amount of manganese oxide (impurity phase) are quite often recognizable in the samples obtained by sol-gel method [49]. Therefore it can be assumed that this sample also has been synthesized by a method close to the sol-gel technique. But it should be emphasized that there is practically no structural data on commercial spinels. Like in the case of laboratory synthesized by high temperature sol-gel method samples (SH, DH), this material undergoes at low temperature structural phase transition from cubic (Fd-3m) to orthorhombic (Fddd) phase. XRD pattern of this type of sample measured at -25°C exhibit diffraction lines belonging both to manganese oxide and to orthorhombic spinel phase. The quantity of impurity (close to 3%) exceeds those given by manufacturer (0.5%) more than six times. It can be than speculated that sol-gel reaction is not completed in industrial conditions (in large scale production). The elementary cell volume change does not exceed 0.03%, and volume of orthorhombic phase is a little bigger than volume of the cubic phase.

8.3.2. Heated up to 800°C

After heat treatment up to 800°C the spinel peaks become narrower, and shifted towards low angles as a result of increase of cell constant and growth of crystallites. The average crystallite size increase is about 17%. The diffraction peaks from Mn_3O_4 impurity phase became weaker and Rietveld refinement indicates that the quantity of impurity is lowered about three times. The elementary cell volume change does not exceed 0.13% and, probably because of the lowering of impurity quantity, the cell volume of cubic phase is slightly bigger than of the orthorhombic one. This is opposite to the situation in the case of the spinel sample without heat treatment, where volume of orthorhombic phase was a little

bigger. This fact is probably related with the presence of different quantities of impurities in both samples.

Simultaneous XRD and impedance spectroscopy measurements confirmed that lithium manganese spinel obtained from Alfa Aesar Co. and heat treated at 800°C exhibits upon cooling below room temperature phase transition from cubic to orthorhombic structure. Thermal hysteresis of conductivity was considerably narrower than in the case of SH and DH samples. The conductivity of the studied sample decreases by a factor of about 10 on cooling from 22^0C to 10^0C. The temperature dependence of resistance is well correlated with change of shape of the X-ray pattern near 400 reflection; a narrow peak characteristic for cubic phase was recorded during cooling from 100^0C down to 22^0C. and a broad maximum, consisting of three peaks characteristic for orthorhombic phase, reaches constant width at low temperatures. During heating, the phase transition from orthorhombic to cubic structure progressed over a range of temperatures from 10°C to 30°C.

8.4. $LiMn_2O_4$ supplied by Sigma - Aldrich Company

8.4.1. As supplied

XRD patterns of this material exhibit well defined, narrow reflections, which were identified as belonging to $LiMn_2O_4$ cubic (Fd-3m) phase. Additional weak peaks of minor phase were also observed. Subsequently these peaks have been attributed to dilithium manganese (IV) trioxide Li_2MnO_3. Such impurity phases are quite often detectable in samples obtained by a solid state route of synthesis [51]. Therefore it can be assumed that this sample also has been received through the solid state reaction. It should be noted that from a battery-production point of view the presence of Li_2MnO_3 in cathode material is a direct source of capacity loss and increase of battery weight. Lithium extraction (during working cycle of a battery) from Li_2MnO_3 is precluded because the manganese ions are already in 4+ oxidation state and therefore cannot be further oxidized. Therefore this impurity phase is more harmful than manganese oxide in the case of previously described samples because in Mn_3O_4 most of Mn ions are in 3+ oxidation state.

The quantity of impurity calculated by Rietveld refinement analysis was close to 5% and it was not specified by manufacturer. It probably means that solid state reaction can not be

completed fully in industrial conditions (large scale production). Additionally in the supplied spinel in the form of black powder red inclusions of an impurity were visible. In comparison with the previously described samples, in this sample only part of the dominating spinel cubic phase undergoes a phase transition and there is no change in XRD pattern of the impurity phase.

8.4.2. Heated up to 800°C

Like in the previous case the XRD patterns of this material exhibit well defined reflections, which belong to $LiMn_2O_4$ cubic (Fd-3m) phase. The reflections become narrower because of the increase of crystallite size (about 15-19%), caused by heat treatment. Additional weak peaks of minor phase are still observed, belonging to Li_2MnO_3 phase (about 3.5%). It means that decrease of the impurity content does not exceed 1.5%. This can be related e.g. with higher temperature of the synthesis procedure (typical temperature for solid state reactions is 800-1000°C). The cell parameter change does not exceed 0.016%, which can also confirm hypotheses about previous high temperature treatment of the sample.
Like in the case of the Aldrich sample without heat treatment, in this sample only part of the dominating spinel cubic phase undergoes a phase transition, but only 49.64% of cubic phase was transformed as compared to 62.64% for unheated sample. There is no change in quantity of the impurity phase. The impedance measurements confirm that in the sample the phase transition is not complete even at -25°C and no stepwise change of conductivity is observed for this sample.
Although in the conductivity measurements there was no indication of the phase transition, the X-ray patterns indicated nevertheless pure cubic spinel phase at +50°C and a mixture of two coexistent spinel phases (cubic and orthorhombic) at -25°C. The impurity phase was not involved in phase transition. The temperature dependence of FWHM was well correlated with thermal changes in resistivity (Fig 7.40.) but there is no hysteresis in that case.

8.5. $Li_{1.0237}Mn_{1.9763}O_4$ and $Li_{1.0392}Mn_{1.9608}O_4$ supplied by Honeywell Specialty Chemicals Company

Little difference between cell parameters of samples probably could be explained by presence in (HDS30) spinel sample bigger quantities of Mn 4+ ions occupying octahedral

positions (with lower ionic radius then Mn 3+ ions) than in case of (HDS10) sample. (Ionic radius of Mn in 3+ oxidation state in octahedral surrounding is 78.5 pm and Mn 4+ is 67 pm. [52])

Because these samples do not undergo phase transition they were not further investigated.

8.6. $Li_{1.20}Mn_{1.80}O_4$ synthesized by high and low temperature sol-gel method

8.6.1. $Li_{1.20}Mn_{1.80}O_4$ synthesized by low temperature sol-gel method

XRD patterns recorded at 25°C show reflections corresponding to typical cubic spinel structure. Strong broadening of diffraction lines is related with small average crystallite size and, probably, internal defects of the structure. In this sample, seemingly consisting of only one phase, two coexisting phases are found when Rietveld analysis is applied. The cell parameters of the dominating phases are quite low for stoichiometric $LiMn_2O_4$ spinel. Such a low cell parameters could be attributed to defected spinel structure with a general formula $Li_4Mn_5O_{12}$. The second phase has cell parameter close to $LiMn_2O_4$ stoichiometric spinel.

8.6.2. $Li_{1.20}Mn_{1.80}O_4$ synthesized by low temperature sol-gel method and heat treated up to 600°C

After heat treatment up to 600°C the spinel peaks on the XRD patterns become narrower, shifting towards low angles and are more symmetrical. It is caused by average crystallite size and cell constant growing respectively and increasing of homogeneity of the sample. In heat treated samples only one spinel phase with cell parameter quite low for stoichiometric spinel (probably caused by defected structure of the sample) is detectable on XRD patterns. About twofold increase of crystallite size is observed.

8.6.3. $Li_{1.20}Mn_{1.80}O_4$ synthesized by low temperature sol-gel method and heat treated up to 800°C

During next heat treatment up to 800°C, the processes of peak shift sharpening and narrowing are continued due to the same reasons: cell constants and crystallites are growing. Small peaks from impurity phase became visible as a result of formation of Li_2MnO_3 phase. Average crystallite size is increasing by about 43% in comparison with the previous sample.

8.6.4. $Li_{1.20}Mn_{1.80}O_4$ synthesized by high temperature sol-gel method

XRD patterns of samples obtained by high temperature sol-gel synthesis display diffraction lines of cubic (Fd-3m) lithium manganese spinel phase and additional weak peaks of Li_2MnO_3.phase (dilithium manganese (IV) trioxide). Average crystallite size is more than three times highest than for sample obtained by low temperature sol-gel synthesis.

From the above presented summary of the results it is evident that the Rietveld method was successful in determination of crystal structure and phase composition in the samples before and after phase transformation (where it occurs). And this is especially important considering the nanocrystalline nature of the spinels and the fact that the different spinel oxide phases coexisting in some samples have very close structural parameters and the minor impurity phases detected in some samples were even in quantity of only about one percent

The separate problem is the course of the phase transition. Due to the problem of the kinetics of the transformation and problem of statistics of measurements for the Rietveld method (use of PSD counter) the "classical" XRD approach (i.e. analysis of width of individual reflections) had to be used. Nevertheless it was possible to show the direct relationship between the change in FWHM and electrical parameters.

9. MAIN CONCLUSIONS

1. All the studied materials were in the nano range of crystallite sizes.

2. It was shown that the Rietveld method was successfully used for investigation of these materials. The phase composition and estimation of their contents was possible. This is especially noticeable considering the size of crystallites and fact that the identified spinel phases are structurally very close and the the minor impurity phases are of the order of few percent (and in some cases even less).

3. The novel equipment for simultaneous measurements of XRD patterns and electric parameters was designed, constructed and applied for in situ measurements.

4. By making use of this equipment, the direct correlation of electric and structural parameters was evidenced.

ANNEX I

AI. Rietveld refinement strategy in practice.

The basic requirements for any Rietveld refinement are: (a) accurate powder diffraction intensity data measured in intervals of 2θ (i.e. step-scan). (b) a starting structural model that is reasonably close to the actual crystal structure of the material of interest, and (c) a mathematical model that accurately describes shapes, widths and any systematic errors in the positions of the Bragg peaks in the powder pattern.

AI-1. Data collection

In the great majority of studies reporting Rietveld refinements using powder XRD data, the data were collected using automated powder diffractometers, primarily because accurate digitized step-scan intensity information can be collected quickly and easily. For Rietveld refinement, it is essential that the powder diffraction data are collected appropriately. Factors to consider prior to data collection are: the geometry of the diffractometer, the precision of the instrument alignment and calibration, the most suitable source of radiation (e.g. conventional X-ray sealed-off tubes, synchrotron X-ray or neutrons), the wavelength, appropriate sample preparation and thickness, slit sizes, and necessary counting time. If the relative intensities and/or the 2θ values (d spacings) are not correct, any amount of time spent further on the structure refinement calculation will bring about no sensible results.

To ensure a constant volume condition, it is important for Bragg-Brentano geometry that the incident beam illuminates only the sample independently on the diffraction angle. Quite often the divergence slits which are used are too wide and the beam hits also the sample holder at the low angles, so the intensities measured at these angles are too low. Some programs can correct for this, but most do not. If a correction is used, the shape of the sample holder *(i.e.* circular or rectangular) must also be taken into account. It should not be assumed that using a rotating circular sample will eliminate the problem. Therefore an appropriate data-collection strategy will depend also on the nature of the sample *(e.g.* how well it scatters, how quickly the pattern degrades, peak-broadening effects and the degree of peak overlap). The practice indicates that there should be at least five steps (but generally not more than ten) across the top of each peak *(i.e.* step size = FWHM/5, where FWHM is the full width at half-maximum), the time per step should approximately compensate for the gradual decline in

intensity with 2θ and the maximum 2θ value should be chosen to give the maximum useful information. Finally, data should be collected to the highest 2θ angle possible. High-angle data are especially important for successful refinement of temperature factors. Diffraction patterns with severely broadened reflections at intermediate angles (80^0 to 100^o) probably will not contain much useful information at high angles, but even severely overlapped reflections at high angles are still useful and should be included.

Another problem is that of sample transparency. The assumption for reflection geometry is that the sample is "infinitely thick" *(i.e.* the X-ray beam is totally absorbed by the sample). If the sample contains only light elements, this condition might not be fulfilled. Then the constant-volume assumption is not valid and the intensities measured at high angles will be too low unless an appropriate correction is introduced at the refinement stage. For such materials, transmission geometry usually is preferred.

On the other band, heavily absorbing samples can be a problem in a transmission set-up, because the incident beam cannot penetrate the whole sample. In this case, the sample may have to be diluted with a light-element material *(e.g.* diamond powder or glass beads). For such samples, reflection geometry is usually to be preferred. However, for highly absorbing materials, a potential source of error in reflection geometry is that of surface roughness. This can reduce the intensity of low-angle reflections and lead in refinement to anomalously low thermal parameters.

Preferred-orientation effects often met in practice can be difficult to eliminate, especially for flat-plate specimens, and these can also lead to incorrect intensity measurements. If the intensities show a strong *hkl* dependence *(e.g.* all *00l* reflections are strong and all *hk0* weak), preferred orientation of the crystallites should be suspected. Although many Rietveld refinement programs allow refinement of a preferred-orientation parameter, this is usually only a crude approximation to reality, so elimination (or minimization) of the problem experimentally is to be preferred. Rotation of a horizontally mounted capillary (usual set-up at a synchrotron) can virtually eliminate preferred-orientation effects, although long needles may still tend to remain aligned along the capillary axis. If other considerations dictate that a flat-plate sample should be used, spray drying the sample to minimize preferred orientation should be considered. Rotation of a flat-plate sample in its own plane will not correct preferred-orientation effects. For classical XRD measurements an ideal particle size within a powder sample is circa 1-5 μm. If large crystallites are used, there are fewer crystallites in the sample and nonrandomness *(i.e.* not all crystallite orientations are equally represented) may become a

problem. This can cause nonsystematic inaccuracies in the relative intensities that, unlike preferred- orientation effects, cannot be corrected at the refinement stage. Sample rotation will improve the particle statistics and is strongly recommended. If smaller particles are used, line-broadening effects due to crystallite size begin to become apparent. If there are one or more large crystallites within a sample of smaller ones ("rocks in the dust"), the relative intensities of the reflections originating from the larger crystallites will be too high in comparison with the other reflections and as with non-randomness, no correction can be applied at the refinement stage.

AI-2. Sample preparation

Considering the above (and also for other reasons) sample preparation is one of the most critical stages of any structure study based on powder XRD data. Many materials exhibit some cleavage and therefore are prone to yield powder samples having non-randomly oriented crystallites. Consequently, observed peak intensities will be inaccurate to some unknown degree, resulting in an incorrect refined structure. In many cases, grinding samples to very small particle sizes and using proper sample mounting techniques can greatly reduce preferred orientation problems. Even for samples that do not show a pronounced cleavage, it is essential that they be ground to particle sizes generally less than about 10 μm, depending on their absorption characteristics.

Several methods are described in the literature for preparing random XRD powder mounts, for example side- or back-loading, dilution with a second phase, spray drying and dusting the sample onto glass fiber-filters. Unfortunately, none of these preparation techniques will guarantee a random sample and it is therefore important to compare data from several sample mounts to assess the magnitude of any preferred orientation effects. Some publications has shown that sieving powder onto a glass microfibre filter is an effective method for preparing a random sample. One drawback, however, is that for weakly absorbing materials it might not be possible to prepare a sample layer on the filter substrate that is infinitely thick to X-rays, thereby contributing background (from the filter) and transparency effects to the resulting powder pattern that must be accounted for during the Rietveld refinement. These effects, if not properly modeled in the refinement can result in significant errors, particularly in temperature factors. Whatever is the sample preparation technique, the mounted sample should be effectively "infinitely thick" (this depends on radiation used and absorption

properties of the sample) and be large enough to contain fully the X-ray beam at the lowest diffraction angle of interest.

The 2θ values should be carefully calibrated using several peaks from a standard material (e.g. NIST Si standard SRM 640b). Almost any diffractometer can be adjusted so that the deviations of the measured peak positions from the correct ones are less than 0.01^{o} *(2θ).* Although longer data-acquisition times are required with monochromatic radiation, its use is particularly advantageous: the number of lines in the pattern is halved (so the severe overlap of reflections begins at higher angles) and the background is lower. If both α_1 and α_2 components are used in the data collection, the spectral distribution (intensity ratios) and dispersion (profile changes as a function of 2θ) must also be calibrated.

Any temptation to smooth the diffraction data before doing a Rietveld refinement must be resisted. Smoothing introduces point-to-point correlations (off-diagonal weight matrix elements) which will give falsely lowered e.s.d.'s in the refinement.

AI-3. Background contribution

There are basically two approaches to dealing with the background in a powder diffraction pattern. It can either be estimated by linear interpolation between selected points between peaks and then subtracted, or it can be modeled by an empirical or semi-empirical function containing several refinable parameters. Both have their advantages and disadvantages. For a simple pattern where most peaks ale resolved to the baseline, both methods tend to work well and the fit is easily verified with a plot.

For complex patterns with a high degree of reflection overlap, however, the majority of the peaks are not resolved to the baseline, so the estimation of the background is difficult. This means that if a background subtraction approach is used, the background usually has to be re-estimated and re-subtracted several times during a refinement. The background variance is also difficult to estimate and is often assumed to be zero. However, it should be taken into account if the weighting scheme used in the refinement [usually $1/\sigma^2(I)$] is to be correct. While background subtraction can be a somewhat cumbersome approach to background correction and may seem to be rather unsophisticated, it has the advantage of being flexible.

It might appear that refining the background would be the preferred method, because this would eliminate same of the problems inherent to background subtraction *(i.e.* the background and structural parameters can be refined simultaneously and the standard deviations estimated in the usual way). However, the polynomial functions usually used for this purpose are largely

or entirely empirical. If the polynomial happens to describe the background well, then, as might be expected, this procedure also works well; but it if does not, no amount of refining the coefficients of the polynomial (or increasing the order of the polynomial) can correct the problem and the refinement will not proceed satisfactorily. In such a case, background subtraction is the better approach. Of course, it is also possible to use the two techniques in combination. A simple empirical function can be used to fit the background and then the deviations described by a sequence of fixed points. The advantage is that the magnitude of the fixed part is minimized and thus the impact of its inherent arbitrariness on the refinement is reduced.

AI-4. Starting model

Because the Rietveld method is primarily a refinement technique, it is necessary to start with a model that is a reasonable approximation of the actual crystal structure. Commonly, a starting model, or at least partial model, is conceived by analogy to similar structures, for example other members of a solid solution series or isostructural materials whose crystal structures are known. Alternately, a model might be developed using distance-least-squares electrostatic energy minimization or other computer modeling procedures. In some cases, high-resolution transmission electron microscope images can provide sufficient information from which to assemble a structure model.

AI-5. Peak-shape function

Accurate description of the shapes of the peaks in a powder pattern is critical to the success of a Rietveld refinement. If the peaks are poorly described, the refinement will not be satisfactory. The peak shapes observed are a function of both the sample *(e.g.* domain size, stress/strain, defects) and the instrument *(e.g.* radiation source, geometry, slit sizes), and they vary as a function of 2θ. In certain cases, they can also vary as a function of *hkl* indices. Accommodating all of these aspects in a single peak-shape description is nontrivial and compromises are often necessary.

Of the analytical peak-shape functions investigated, the pseudo-Voigt approximation of the Voigt function is probably the most widely used for X-ray and constant wavelength neutron data. The pseudo-Voigt function (I-4) is simply a linear combination of Lorentzian and Gaussian components in the ratio $\eta/(1-\eta)$, where η is the pseudo-Voigt mixing parameter (I-4).

This appears to describe the symmetrical part of an X-ray diffraction peak quite well. However, an additional function to allow a more precise description of asymmetry due to axial divergence of the diffracted beam at low angles is essential (Thompson-Cox-Hastings pseudo-Voigt [A1] for example). For X-ray diffraction lines dominated by instrumental broadening, η usually varies in a linear manner, from a dominant Gaussian component at low angles to a Lorentzian trend at high angles. If a Pearson VII peak-shape function (I-3) is used, the exponent *m* varies differently, but the same trends in line shape are observed. An advantage of the pseudo-Voigt or Voigt functions is that they allow the Gaussian and Lorentzian components of the peak shape to be introduced in a physically intuitive way to model the overall line broadening, which furnishes useful information about the microstructure with respect to size and strain effects. The Pearson VII function does not have this physical basis. However, both can be used to describe the peak shape for Rietveld refinement.

Regardless of the type of peak-shape function selected, the range of the peak *(i.e.* when it no longer contributes significant intensity to the diffraction pattern) must be established. As a rule of thumb, a peak can be considered to be down to background level when the intensity is less than 0.1-1.0% of the peak maximum. The appropriate percentage depends upon the peak shape. If the 'tails' of the peaks are long *(i.e.* high Lorentzian character), a wider range will be required than for peaks with more Gaussian character. The range needed depends upon the FWHM of the peak; thus it is usually expressed as an integral number of FWHM values, though some programs use a fraction of the peak height. Typically, the value will range from 10 to 20 × FWHM depending upon the Lorentzian character of the peak. Thus, a reflection with an FWHM of $0.10^{o}(2\theta)$ contributes to the diffracted intensity over a range of at least 1.0-$2.0^{o}(2\theta)$ (and sometimes much more). This parameter is often set at much too low a value, resulting in a severe underestimation of the reflection intensity. If the 'tails' of high-intensity reflections are cut off prematurely in the profile plot this is a good indication that the range has been set at too small a value.

Most of the commonly used profile shape functions, including the Pearson VII and pseudo-Voigt, are symmetrical about the nominal Bragg peak positions. A variety of instrumental and sample effects, for example axial divergence of the X-ray beam and structure disorder in the sample, however, give rise to pronounced asymmetry in the observed peak shape, especially at low diffraction angles. Consequently, most Rietveld refinement computer programs include as a variable a semi-empirical asymmetry correction term. This factor corrects primarily asymmetry at low angles caused by axial divergence of the X-ray beam and does not affect

the integrated intensity but will shift the apparent peak position. The use of both incident- and diffracted-beam Soller slits during data collection significantly reduces asymmetry on the low-angle side of peaks (and improves resolution). Also, because asymmetry is largely associated with low-angle peaks, in some cases results might be improved if only the higher-angle data are used in the refinement.

All the profile functions Ω used in FullProf are normalized to 1 (i.e. $\int_{-\infty}^{+\infty} \Omega(x)\,dx = 1$).

The variable is $x=T-T_h$, (definitions of T and h are given in chapter 3.1.1.) the FWHM will be called H. The definition of $\Omega(x)$, is the following:

• *GAUSSIAN*: $\Omega_G(x)=G(x)=a_G\exp(-b_G x^2)$ (I-1)

where: $a_G = \frac{2}{H}\sqrt{\frac{\ln 2}{\pi}}$ $b_G = \frac{4\ln 2}{H^2}$

The integral breadth of the Gaussian function is: $\beta_G = \frac{1}{a_G} = \frac{H}{2}\sqrt{\frac{\pi}{\ln 2}}$

• *LORENTZIAN*: $\Omega_L(x) = L(x) = \frac{a_{ML}}{1 + b_L x^2}$ (I-2)

where: $a_L = \frac{2}{\pi H}$ $b_L = \frac{4}{H^2}$

The integral breadth of the Lorentzian function is: $\beta_L = \frac{1}{a_L} = \frac{\pi H}{2}$

• *PEARSON VII*: $\Omega_{VII}(x) = PVII(x) = \frac{a_{VII}}{(1 + b_{VII} x^2)^m}$ (I-3)

where: $a_{VII} = \frac{\Gamma(m)}{\Gamma(m) - 1/2}\frac{2\sqrt{2^{1/m} - 1}}{\sqrt{\pi}H}$ $b_{VII} = \frac{4(2^{1/m} - 1)}{H^2}$

• *PSEUDO-VOIGHT*: $\Omega_{pV}(x)=pV(x)=\eta L'(x)+(1-\eta)G'(x)$ $0\le\eta\le1$ (I-4)

• *Thompson-Cox-Hastings pseudo-Voigt* convoluted with axial divergence asymmetry function [A1].

The $pV(x)$ function is a linear combination of a Lorentzian (L') and a Gaussian (G') of the same FWHM $(H)^2$, so there are two parameters characterizing the peak shape: $pV(x) = pV(x,\eta,H)$. If $L'(x)$ and $G'(x)$ are normalized, $pV(x)$ is also normalized. The integral breadth of a normalized pseudo-Voigt function is just the inverse of the maximum value. The FWHM is

the same for $L(x)$, $G(x)$ and $pV(x)$. If the function is multiplied by a constant (integrated intensity) the integral breadth doesn't change:

$$\beta_{pV} = \frac{\int \Omega(x)dx}{\Omega(0)} = \frac{\int I_i pV(x)dx}{I_i pV(0)} = \frac{1}{pV(0)} \qquad \beta_{pV} = \frac{\pi H/2}{\eta + (1-\eta)\sqrt{\pi \ln 2}} \tag{I-5}$$

The difference between pseudo-Voigt (pV) and Thompson-Cox-Hastings pseudo-Voigt (TCHpV) is that in the later the parameter η is not directly refinable but calculated from H_L and H_G. The pseudo-Voigt function is an approximation to the Voigt function defined as the convolution of a Lorentzian and a Gaussian:

$$VOIGT: \quad V(x) = L(x) \otimes G(x) = \int_{-\infty}^{+\infty} L(x-u)G(u)du \tag{I-6}$$

where $L(x)$ and $G(x)$ have different FWHM (H_L and H_G, respectively). The $pV(x)$ function is an approximation that substitutes the two shape parameters H_L and H_G by the pair (η,H).

AI-6. Systematic line-shifts (for Bragg-Brentano arrangement)

Powder diffraction data are sometimes affected by systematic aberrations resulting from the sample itself or from an improper setting of the sample or diffractometer. One of the most popular program used for Rietveld refinement FullProf gives the possibility to correct for two of the most commonly occurring errors by refining the parameters called *Sycos* and *Sysin*. These parameters relate to errors having a cosθ and sinθ dependency, respectively. The corresponding errors originate from a different physical or/and geometrical problem depending on the diffraction geometry.

The two largest systematic aberrations of $\theta-2\theta$ powder diffractometers operating in this geometry arise from specimen displacement and transparency. The sample displacement error is one of the largest systematic errors affecting line positions in this geometry. It is given by:

$$\Delta 2\theta = \frac{-2s}{R}\cos\theta \ \ [in\ radians], \tag{I-7}$$

where s is the displacement of the sample surface with respect to the axis of the goniometer and R the radius of the goniometer circle. The negative sign means that a displacement away from the centre of the focusing circle moves the diffraction lines to lower 2θ angle. The refinable parameter is $SYCOS$=-2s/R. This is by far the largest systematic aberration in this geometry. As the angles are expressed in degrees in FullProf, the sample offset can be calculated as: s=π/180·R·$SYCOS$. The transparency correction is given by the relation:

$$\Delta 2\theta = \frac{1}{2\mu R} \sin\theta \ [in\ radians], \qquad \text{(I-8)}$$

where μ is the linear absorption coefficient of the sample. This relation holds in the case of thick absorbing samples and the refinable parameter is *SYSIN*=1/(2μ*R*). For thin transparent amples, the correction would write:

$$\Delta 2\theta = \frac{t}{R} \cos\theta \ [in\ radians] \qquad \text{(I-9)}$$

where *t* is the sample thickness; this (less usual) correction is not explicitly included in the program code but can be accounted for by the displacement correction which turns out to show the same 2θ dependency. It should be noted however that samples requiring that kind of correction would also give biased integrated intensities; correction for this effect is not implemented in FullProf.

The presented above recommendation follow those given by well recognized authors and advanced users of method: H.M. Rietveld, R.A. Young, R.B. Von Dreele, L.B. McCusker, D. Louer, J.E. Post D.L. Bish and others [A1,A2,A3,A4,A5,A6].

References:

A1. L. W. Finger, D. E. Cox and A. P. Jephcoat, "A correction for powder diffraction peak asymmetry due to axial divergence". J. Appl. Cryst. 27, 892, 1994

A2. H.M. Rietveld "A Profile Refinement Method for Nuclear and Magnetic Structures" J. Appl. Cryst. ,2 (1969) 65-71

A3. L.B. McCusker, R.B. Von Dreele, D.E. Cox, D. Louer, P. Scardi "Rietveld refinement guidelines" Reprinted from J. Appl. Cryst., 32, (1999), 36-50

A4. R.A. Young "The Rietveld Method". Oxford, University Press, 1993

A5. R.J. Hill, I.C. Madsen "Data Collection Strategies for Constant Wavelength Rietveld Analysis" Powder Diffraction, Vol.2 № 3 September 1987

A6. D.L. Bish, J.E. Post "Rietveld Refinement of Crystal Structures Using Powder X-ray Diffraction Data" in Reviews in Mineralogy Vol.20, Series Editor P.H. Ribbe, Mineralogical Society of America 1989

10. REFERENCES

1. http://www.batteryuniversity.com/parttwo 34.htm, Copyright 2003-2005 I. Buchmann

2. http://www.webopedia.com, Copyright 2005 Jupitermedia Corporation

3. M.M. Thackeray "Spinel Electrodes for Lithium Batteriers" J. Am. Ceram. Soc., 82 (12) (1999) 3347-3354

4. M.M. Thackeray "Manganese Oxides for Lithium Batteries" Prog. Solid St. Chem., 25 (1997) 1-71 Published by Elsevier Science Ltd Printed in Great Britain

5. "International Tables For Crystallography" Volume A, Theo Hahn editor (published for IUCr) Kluwer Academic Publishers 1993

6. Z. Bojarski, M. Gigla, K. Stróż, M. Surowiec „Krystalografia, podręcznik wspomagany komputerowo". Wydawnictwo Naukowe PWN, Warszawa 1996

7. Jaephil Cho, M.M. Thackeray "Structural changes of $LiMn_2O_4$ spinel electrodes during electrochemical cycling" Journal of The Electrochemical Society, 146 (10) (1999) 3577-3581

8. P.W. Atkins "Physical chemistry" fourth edition. Oxford university press 1992. (Polish edition P.W. Atkins „Chemia fizyczna". Wydawnictwo Naukowe PWN, Warszawa 2001).

9. http://www.answers.com Copyright 1999-2005 by GuruNet: Online Encyclopedia, Thesaurus, Dictionary definitions and more (Wikipedia).

10. J. Klamut, K. Durczewski, J. Sznajd „Wstęp do fizyki przejść fazowych". Zakład Narodowy Imenia Ossolińskich, Wydawnictwo PAN, 1979

11. A.B. Pippard "The Elements of Classical Thermodynamics". Cambridge University Press, 1957

12. A. Münster "Statistical Thermodynamics" vol. 1. Springer-Verlag-Berlin-Hiedelberg-New York, Academic Press, 1969.

13. L. Tisza "On the general theory of phase transitions". In: Phase transformations in solids. R.J. Smoluchowski, I.E. Mayer, W.A. Weyl, editors; John Wiley and Sons Inc., New York 1951

14. N.V.C. Shekar, K.G. Rajan "Kinetics of pressure induced structural phase transitions-A review" Bull. Mater. Sci., 24 (1) (2001) 1–21

15. S.C. Gupta, R. Chidambaram "Symmetry Systematics of Pressure-Induced Phase Transitions" High-Pressure Res., 12 (1994) 51-70

16. C.N.R. Rao, K.J. Rao "Phase transitions in solids". NewYork, McGraw Hill, 1978

17. M.T. Dove "Structure and Dynamics". In: An Atomic View of materials, Oxford University Press, 2003

18. http://www.rphf.h1.ru. В.Б.Бондаренко, Конспект лекций по физике твердого тела

19. L.D. Landau, E.M. Lifshitz "Fizyka Statystyczna (Statistical Physics)". PWN 1959

20. Г.С. Жданов, А.Г. Хунджуа „Лекции по физике твердого тела". Москва, МГУ, 1988

21. L.C. Klein "Sol gel formation and deposition". In: Handbook of nanophase materials. A. Goldstein editor; Marcel Dekker Inc., 1997

22. M. Jurczyk, J. Jakubowicz „Metoda zol-żel". In: Nanomaterialy ceramiczne. Wydawnictwo Politechniki Poznańskiej, 2004

23. D. Hreniak, W. Stręk „Materiały nanokrystaliszne i nanokompozytowe otrzymywane technikami zol-zelowymi (Nanocomposites and nanokrystalline materials prepared by sol-gel techniques)". In: Nanomateriały (Nanomaterials). Polskie Towarzystwo Chemiczne, Wrocław, 2004

24. C.A. Huber "X-ray diffraction characterization of nanophase materials". In: Handbook of nanophase materials. A. Goldstein editor, Marcel Dekker Inc., 1997

25. D. Zanchert, B.D. Hall and D. Ugarte "X-ray Characterization of Nanoparticles". In: Characterization of Nanophase Materials. Zhong Lin Wang editor, WILLEY-VCH, 2000

26. D. Lisovytskiy, Z. Kaszkur, V.N. Baumer, J. Pielaszek, M. Molenda, R. Dziembaj, J. Marzec, J. Molenda, J. Dygas, M. Kopec, F. Krok "Phase transformation of nanocrystalline lithium manganese spinels produced by low and high temperature methods" Molecular Physics Reports, 35 (2002) 26-30

27. R. Dziembaj, M. Molenda, D. Majda, S. Walas „Synthesis, thermal and electrical properties of $Li_{1+\delta}Mn_{2-\delta}O_4$ prepared by sol-gel method" Solid State Ionics, 157 (2003) 81-87

28. H.M. Rietveld "Line Profiles of Neutron Powder-diffraction Peaks for Structure Refinement" Acta Cryst., 22 (1967) 151-152

29. H.M. Rietveld "A Profile Refinement Method for Nuclear and Magnetic Structures" J. Appl. Cryst. ,2 (1969) 65-71

30. R.A. Yong, P.E. Mackie, and R.B. Von Dreele "Application of the pattern-fitting structure-refinement method of X-ray powder diffractometer patterns" J. Appl. Cryst., 10 (1977) 262-269

31. A. Antoniadis, J. Berruyer and A. Filhol "Maximum-likelihood methods in powder diffraction refinements" Acta Cryst., A46 (1990) 692

32. R.J. Hill, H.D. Flack "The use of the Durbin-Watson *d* statistic in Rietveld analysis" J. Applied Cryst., 20 (1987) 356

33. Handbook of nanophase materials. A. Goldstein, editor, Marcel Dekker Inc., 1997

34. H. P. Klug and L. E. Alexander "X-Ray Diffraction Procedures for Polycrystalline and Amorphous Materials" 2nd ed. Wiley, New York, 1974

35. H. Lipson and H. Steeple "Interpretation of X-Ray Powder Diffraction Patterns". St. Martin's Press, New York, 1970

36. T.O. Mason, J.-H. Hwang, N. Mansourian-Hadavi, G.B. Gonzalez, B.J. Ingram and Z.J. Homrighaus "Impedance/Dielectric Spectroscopy of Nanoceramics". In: Nanocrystalline metals and oxides-selected properties and applications edited by P. Knauth and J. Schoonman, series editor H.L. Tuller, Kluwer, 2002

37. J. E. Garbarczyk, M. Wasiucionek, P. Józwiak, L. Tykarski, J. Nowinski „Studies of Li_2O - V_2O_5 - P_2O_5 glasses by DSC, EPR and impedance spectroscopy" Solid State Ionics, 154-155 (2002) 367–373

38. W. Bogusz, F. Krok „Elektrolity Stałe - właściwości elektryczne i sposoby ich pomiaru". Wydawnictwo Naukowo-Techniczne, Warszawa, 1995

39. W. Jakubowski „Przewodniki Superjonowe". Wydawnictwo Naukowo-Techniczne, Warszawa, 1988

40. A. Authier "Dynamical Theory of X-ray Diffraction", International Union of Crystallography Series, Oxford University Press, 2001

41. O. Masson, R. Guinebretiere, M. Dauger "Reflection Asymmetric Powder Diffraction with Flat-Plate Sample using a Curved Position-Sensitive Detector (INEL CPS 120) J. Appl. Cryst., 29 (1996) 540-546

42. Z. Kaszkur "Powder diffraction beyond the Bragg law: study of Palladium nanocrystals" J. Appl. Cryst., 33 (2000) 1262-1270

43. J. Rodríguez-Carvajal and T. Roisnel "FullProf.98 and WinPLOTR: New Windows 95/NT Applications for Diffraction, Commission For Powder Diffraction" International Union for Crystallography, Newletter N°20 (May-August) Summer 1998

44. T. Roisnel and J. Rodríguez-Carvajal "WinPLOTR: a Windows tool for powder diffraction patterns analysis". In: Materials Science Forum, Proceedings of the Seventh European Powder Diffraction Conference (EPDIC 7), 2000, p.118-123, Ed. R. Delhez and E.J. Mittenmeijer

45. R.A. Young "The Rietveld Method". Oxford, University Press, 1993

46. D. Lisovytskiy, Z. Kaszkur, J. Pielaszek, M. Marzantowicz, J.R. Dygas "In situ impedance and X-ray diffraction study of phase transformation in lithium manganese spinel" Solid State Ionics 176 (2005) 2059 – 2064

47. J.R. Dygas, M. Kopec, F. Krok, D. Lisovytskiy, J. Pielaszek "Conductivity and dielectric relaxation phenomena in lithium manganese spinel" Solid State Ionics, 176 (2005) 2153 – 2161

48. T. Takada, H. Hayakawa, E. Akiba "Preparation and crystal structure refinement of $Li_4Mn_5O_{12}$ by the Rietveld method" J. Solid State Chem., 115 (1995) 420-426

49. V. Masarotti, D. Capsoni, M. Bini, G. Chiodelli "Characterization of sol-gel $LiMn_2O_4$ spinel phase" J. Solid State Chem., 147 (1999) 509-515

50. Z. Bojarski, E. Langewka „Rentgenowska analiza structuralna". Wydawnictwo Uniwersytetu Śląskiego, Katowice, 1995

51. H. Berg, E.M. Kelder, J.O. Thomas "Neutron diffraction study of Stoichiometric spinel $Li_{1+x}Mn_{2-x}O$ showing octachedral 16c-site Li occupation" J. Mater. Chem., 9 (1999) 427-429

52. www.webelements.com Copyright 1993-2005 Mark Winter, The University of Sheffield and WebElements Ltd, UK.